Time-Resolved Spectroscopic Studies of Chlorine and Bromine Atom Reactions in Solution

by

Jae Yoon Shin

A dissertation submitted in partial fulfillment of

the requirements for the degree of

Doctor of Philosophy

(Chemistry)

at the

UNIVERSITY OF WISCONSIN – MADISON

2015

Date of final oral examination: 8/21/2015

The dissertation is approved by the following members of the Final Oral Committee:

F. Fleming Crim, Professor, Physical Chemistry
Martin Zanni, Professor, Physical Chemistry
John Wright, Professor, Analytical Chemistry
Etienne Garand, Assistant Professor, Physical Chemistry
Amanda Case, Scientist, Physical Chemistry

Time-Resolved Spectroscopic Studies of

Chlorine and Bromine Atom Reactions in Solution

Jae Yoon Shin

Under the supervision of Professor F. Fleming Crim

at the University of Wisconsin-Madison

Ultrafast time-resolved pump-probe spectroscopy monitors the dynamics of bimolecular reactions of Cl and Br atoms in solution with sub-picosecond time resolution. A photolysis pulse dissociates a given precursor to generate either Cl or Br atoms, and a UV/VIS or mid-IR probe pulse monitors the evolution of the atom or a reaction product. The hydrogen abstraction reactions of Cl and Br atoms with organic molecules are exoergic and endoergic, respectively. In the case of Br atom reaction, we introduce an additional near-IR pump pulse to promote this endoergic reaction using vibrational excitation.

The reactions of Cl atoms with alkanes and alkenes exhibit rate constants that are diffusion-limited (or faster) and are ranked by the number of C=C bonds in the reactants. This suggests that an attractive intermolecular force between the Cl atom and the C=C bond influences the reaction rates. The reactions of Cl atoms with alkenes produce vibrationally excited HCl (v=1). The branching into HCl (v=1) shows a solvent viscosity dependence, owing to a dampening of the vibrational excitation. In contrast, the reaction rates are faster in a more-viscous solvent, implying a failure of simple diffusion theory in describing the reactions of Cl atoms with alkenes.

In the reactions of Br atoms, we seek to realize the first vibrationally driven bimolecular reaction. Our most promising prospects are the reactions of Br atoms with CH_3OH and DMSO.

We observe a difference signal in the decay of the Br–solvent complex when the near-IR pump is resonant with the C–H or O–H overtone stretches of CH_3OH and DMSO. This difference signal contains a negative offset at long times, which signifies a loss of the Br–solvent following vibrational excitation. This could be due to vibrational predisocciation of the complex, followed by either geminate recombination to re-form the solvent and the Br precursor or reaction of the Br atoms with vibrationally excited solvent molecules.

Table of Contents

List of Figures

Chapter 2

Chapter 3

Chapter 4

List of Tables

Chapter 3

Acknowledgement

About five years ago from now, my wife and I were taking a big transition, the transition from living in South Korea to living in the U. S. for my Ph.D. study in Madison. That was a little scary because both of us have never experienced with that big change in our life. However, we met a lot of nice people who helped us to settle down in Madison and feel like being at home. I thank all those people and I think I would not be able to finish my degree without their support.

First, I should give a great thank to Fleming. He has been my role model since I have met him in Madison, not only as a scientist but also as a mentor in the future. He always gave me more than I asked, even when I didn't know what I want from him. Also, he always welcomed me in his office or in the kitchen or in the hallway, wherever I find him, and listened to me. I remember the moment that I was sitting in his office and told him that I am not going to leave the group when he accepted an offer from NSF. I am proud of myself that I made that decision and never regret.

I also thank my friends in the Crim group. Adam Dunkelburger was my lab partner and taught me many things about the experiments, optics, laser, and almost everything in the lab. I really appreciated his supports especially when I was struggling in the first two years after my daughter was born. Ryan Kieda shared the lab before I moved to bimolecular lab and shared office in his last year at Madison. The discussions with him for troubleshooting the lasers were very helpful. I inherited everything in the current lab from T. J. Preston and Michael Shaloski. All the experiments in this thesis were built on their efforts. I also learned tips and tricks for coding from his elaborated LabView codes. Michael and I both join the Crim group in 2010. He has been nice and friendly to me and I really enjoyed conversations with him about Korean and

Korean culture. I hope someday we can speak each other in Korean. Tracey Oudenhoven and Brett Marsh are now in other groups, but they were in our group. Even though we are in different group, they are still encouraging me and supportive. I really appreciate it. Cornelia Heid shared an office with me for years before she left. We had lots of conversations about science, coffee, tea, Switzerland, and South Korea. The thesis fuel (Columbia coffee) she sent me from Columbia kept me writing my thesis and finally finished it. Wyatt Merrill will be the last graduate student of our group, backing me up. I am sure he will also done by soon and proceed to the next. Amanda Case is a second advisor to me. She filled in perfectly Fleming's role and I think she will become a good mentor like Fleming in the near future. Lastly, I thank Andrew Orr-Ewing for the invaluable discussions about Cl atom reaction and sharing their unpublished work.

I know that I owe so many things to my family, their supports, patience, and loves. Now, I may take these back to them and I want them to be proud of me. Finally, to Hyunmi and Olivia, this thesis is really for you.

Chapter 1

Introduction

A chemical reaction happens when two species (molecules or atoms) encounter each other and produce new species or when one species transforms its bonding configuration or geometry. Reaction dynamics describe the reaction mechanisms that explain and predict both bimolecular and unimolecular processes at a molecular level.[1,2] Both experimental and theoretical chemistry make a concerted effort toward the understanding of reaction dynamics for many molecular processes.

In 1972, Polanyi proposed a series of rules for qualitatively understanding and predicting the dynamics of atom + diatom reactions based on numerous infrared (IR) chemiluminescence studies and quasi-classical trajectory (QCT) calculations.[3,4] The Polanyi rules state that the location of a reaction barrier influences the energy disposal into products of and dictates the form of energy that best promotes a bimolecular reaction. For an exoergic reaction, the reaction barrier is usually located 'early' along the reaction coordinate, meaning that the transition state (TS)

structure looks more like the reactants (reactant-like TS) as dictated by Hammond's postulate.[5] In this case, reactant translational energy has the advantage (over vibrational energy) to overcome the reaction barrier and any excess energy is likely to appear as products vibration. On the other hand, in an endoergic reaction, the reaction barrier is located 'late' along the reaction coordinate and the TS structure now looks more like the products (product-like TS). In this case, vibrational energy is more efficient at overcoming the reaction barrier and, thus, to promoting the reaction. After the reaction passes the TS, the excess energy will appear mainly as translational energy of the products.

Experimentalists have extensively examined this tenet of reaction dynamics, in the gas phase. The most prototypical reactions are the hydrogen (or deuterium) abstraction reactions of halogen atoms with methane and its isotopologues. Depending on the identity of the halogen atom, the energetics of these reactions change remarkably, mainly due to the variations in the bond strength of the hydrogen halide products. The hydrogen abstraction reaction of F atoms with CH_4 is highly exoergic (133 kJ mol^{-1}). In IR chemiluminescence studies and crossed-beam experiments that use IR absorption spectroscopy, this reaction exhibits vibrational excitations of the HF products up to the v=3 level, in good agreement with the Polanyi's rules. Also, the co-product, CH_3, has much less vibrational excitations, revealing that the CH_3 moiety of CH_4 acts as a spectator in the reaction dynamics.[6-9] By contrast, the hydrogen abstraction reaction of Cl atoms with CH_4 is modestly endoergic (6 kJ mol^{-1}). Therefore, the influence of vibrational excitation on the reaction dynamics have been thoroughly examined in the reactions of Cl atoms with CH_4 and its isotopologues, establishing mode- and bond-selected chemistry. In the reaction of Cl atoms with CH_3D, exciting the C–H or C–D stretch results in preferential cleavage of the excited bond.[10] Also, exciting different modes, the symmetric or antisymmetric C–H stretch,

yields different reactivity in this reaction, revealing enhanced reactivity upon symmetric C–H stretch excitation.[11] In addition, the hydrogen abstraction reaction of Br atoms with CH_4, is even more endoergic (50 kJ mol^{-1}), but to the best of our knowledge, no studies have been published on this system.

While the gas phase studies have established many aspects of reaction dynamics, condensed phase dynamics have not been widely explored, especially, for bimolecular reactions. Investigating bimolecular reactions in the condensed phase can address many fundamental issues, such as static and dynamic effects of the solvent molecules on the reaction dynamics,[12] but there are experimental difficulties that have slowed progresses. A collision occurs roughly every 100 fs in a liquid, thus requiring 100 fs-time resolution to follow a reaction in the condensed phase. Hochstrasser and colleagues pioneered the use of time-resolved IR spectroscopy to monitor the formation of products in the condensed phase reaction of Cl atoms with cyclohexane[13] and of CN radicals with chloroform.[14] In the reaction of CN and deuterochloroform, they witnessed the first evidence of vibrationally excited products in the condensed phase.[14] Since then, our group has revisited reactions of Cl and CN in the condensed phase.[15-18] We use both time-resolved electronic and vibrational spectroscopies to monitor the dynamics of both reactants and products, obtaining a more complete picture of condensed phase bimolecular reactions. In the reaction of Cl atoms with *n*-pentane,[16] Sheps *et*. *al*. observed the reactive decay of the Cl–solvent complex at 330 nm; its rate of decay matched the growth of the fundamental H–Cl stretch in IR transient absorption measurements. Based on the Smoluchowski model, they determined reaction rates, which are diffusion-limited and depend on the solvent viscosity. In the reaction of CN radicals with chlorinated solvents,[17] Crowther *et*. *al*. found that the reactive decays of the CN–solvent complexes at 400 nm is slower than the growth of the

HCN product by a factor of 2.5 to 12, when monitoring the fundamental of the H–CN stretch at 3.07 μm. They attributed the discrepancy between detecting the loss of a reactant and the formation of a product to differences in the reactivity of two different CN–solvent complexes. Quantum calculations showed the formation of a linear and bridging complex after the photolysis of ICN, and they concluded that the relatively weakly bound linear complex is likely to react up to 12 times faster than the more strongly bound bridging complex.

More recently, Orr-Ewing and co-workers have been studying the reaction dynamics of bimolecular reactions in the condensed phase and collaborating with theoretical expertise.[19-22] In their broadband IR transient absorption study of CN radicals reacting with cyclohexane,[19] they demonstrated the state- and mode-resolved dynamics of a bimolecular reaction, for the first time, in the condensed phase. The high exoergicity of this reaction results in vibrational excitation of the products, both the HCN bend and the C–H stretch at early stages of the reaction; they also follow the relaxation of the vibrationally excited products to the ground state product. The vibrational relaxation of the excited products is now credited as the reason for the discrepancy between the reactant decay and the product growth in the study of Crowther *et. al*. The Orr-Ewing group has also investigated the reactions of Cl and F atoms with hydrocarbons in the condensed phase,[21,22] monitoring the products of the hydrogen abstraction reactions. They observed vibrationally excited products and report on the vibrational relaxation dynamics. In addition, molecular dynamics (MD) simulations with elaborately calculated potential energy surface strongly support the reaction dynamics revealed by their experiments.[20,22]

As the number of case studies increases, the links between the gas and condensed phases becomes clearer, allowing us to deduce invaluable insights into condensed phase reaction dynamics. Recent review papers summarize the work on bimolecular reactions in the condensed

phase and make important comparisons of the reaction dynamics between the gas and condensed phases.[12,23,24] A general trend emerges – the overall reaction dynamics is not fundamentally different from those of the gas phase reaction; exoergicity of the reaction transfers to vibrational excitation of products but with less vibrational excitations. Orr-Ewing proposed that these exoergic reactions are within the non-adiabatic regime of Grotes-Hynes theory;[12,24] hence, the solvent is frozen while the reaction proceeds. Yet, the solvents still play an important role in dampening the vibrational excitations of the nascent products (post-TS friction).

In this thesis, Chapter 2 describes the experimental design and techniques used for our ultraviolet (UV) / visible (VIS) and IR transient absorption measurements. In Chapter 3, we expand upon the current base of Cl atom reactions in the condensed phase by studying the reactions of Cl atoms with alkane and alkenes. In Chapter 4, we attempt to move beyond studying exoergic reactions and look at the endothermic reactions of Br atoms with organic reaction partners, CH_3OH and dimethylsulfoxide (DMSO).

References

(1) Levine, R. D. *Molecular reaction dynamics*; Cambridge University Press, 2005.

(2) Brouard, M.; Vallance, C. *Tutorials in molecular reaction dynamics*; Royal Society of Chemistry, 2010.

(3) Polanyi, J. C. *Acc. Chem. Res.* **1972**, *5*, 161.

(4) Polanyi, J. C.; Wong, W. H. *J. Chem. Phys.* **1969**, *51*, 1439.

(5) Hammond, G. S. *J. Am. Chem. Soc.* **1955**, *77*, 334.

(6) Sugawara, K. i.; Ito, F.; Nakanaga, T.; Takeo, H.; Matsumura, C. *J. Chem. Phys.* **1990**, *92*, 5328.

(7) Nazar, M. A.; Polanyi, J. C. *Chem. Phys.* **1981**, *55*, 299.

(8) Wickramaaratchi, M. A.; Setser, D. W.; Hildebrandt, H.; Kōrbitzer, B.; Heydtmann, H. *Chem. Phys.* **1985**, *94*, 109.

(9) Harper, W. W.; Nizkorodov, S. A.; Nesbitt, D. J. *J. Chem. Phys.* **2000**, *113*, 3670.

(10) Yoon, S.; Holiday, R. J.; Crim, F. F. *J. Chem. Phys.* **2003**, *119*, 4755.

(11) Yoon, S.; Holiday, R. J.; Sibert, E. L.; Crim, F. F. *J. Chem. Phys.* **2003**, *119*, 9568.

(12) Orr-Ewing, A. *J. Chem. Phys* **2014**, *140*, 090901.

(13) Raftery, D.; Iannone, M.; Phillips, C. M.; Hochstrasser, R. M. *Chem. Phys. Lett.* **1993**, *201*, 513.

(14) Raftery, D.; Gooding, E.; Romanovsky, A.; Hochstrasser, R. M. *J. Chem. Phys.* **1994**, *101*, 8572.

(15) Sheps, L.; Crowther, A. C.; Elles, C. G.; Crim, F. F. *J. Phys. Chem. A* **2005**, *109*, 4296.

(16) Sheps, L.; Crowther, A. C.; Carrier, S. L.; Crim, F. F. *J. Phys. Chem. A* **2006**, *110*, 3087.

(17) Crowther, A. C.; Carrier, S. L.; Preston, T. J.; Crim, F. F. *J. Phys. Chem. A* **2008**, *112*, 12081.

(18) Crowther, A. C.; Carrier, S. L.; Preston, T. J.; Crim, F. F. *J. Phys. Chem. A* **2009**, *113*, 3758.

(19) Greaves, S. J.; Rose, R. A.; Oliver, T. A. A.; Glowacki, D. R.; Ashfold, M. N. R.; Harvey, J. N.; Clark, I. P.; Greetham, G. M.; Parker, A. W.; Towrie, M.; Orr-Ewing, A. J. *Science* **2011**, *331*, 1423.

(20) Glowacki, D. R.; Rose, R. A.; Greaves, S. J.; Orr-Ewing, A. J.; Harvey, J. N. *Nat. Chem.* **2011**, *3*.

(21) Abou-Chahine, F.; Greaves, S. J.; Dunning, G. T.; Orr-Ewing, A. J.; Greetham, G. M.; Clark, I. P.; Towrie, M. *Chem. Sci.* **2013**, *4*, 226.

(22) Dunning, G. T.; Glowacki, D. R.; Preston, T. J.; Greaves, S. J.; Greetham, G. M.; Clark, I. P.; Towrie, M.; Harvey, J. N.; Orr-Ewing, A. J. *Science* **2015**, *347*, 530.

(23) Crim, F. F. *Faraday Discuss.* **2012**, *157*, 9.

(24) Orr-Ewing, A. J. *Annu. Rev. Phys. Chem.* **2015**, *66*, 119.

Chapter 2

Experimental Apparatus and Data Acquisition

2.1 Laser system

All the experiments described in this thesis utilized a Coherent Legend ultrafast laser system. The laser specifications state that it produces 2.5 mJ pulses of 800 nm light with a 150 cm^{-1} bandwidth and a 100 fs duration. However as it ages (originally purchased in 2004, it is more than 10 years old and has had more than 11000 hours of running time), the output energy drops from the value specified. When I started to use this laser system, in September 2012, the output energy was 1.9 mJ. The output energy stayed near 1.9 mJ for about a year, after which it started to drop slowly (for the first several months) and then the decrease in output energy became more significant. The main cause of this decrease is the decreasing output power of the pump laser, a Coherent Evolution. Increasing the current supplied to the Evolution and lowering the temperature of its chiller increase the output energy of the Legend, but the standard tune-up procedure described in the theses of Sheps,[1] Crowther,[2] Carrier,[3] and Preston[4] do not help much

to recover the output energy. To study vibrationally driven reactions, we need three or more laser pulses; these pulses are in different wavelength regions and are generated *via* non-linear processes, requiring a high output energy from the Legend. Therefore, we have been trying to maintain an output energy of roughly 1.9 mJ by turning up the Evolution's current source. Initially we were able to get a 1.9 mJ output from the Legend by pumping it with the Evolution output obtained after supplying 21.2 A of current, but now we get 1.6 mJ after supplying 24.6 A to the Evolution, also, we have lowered the chiller temperature from 17 to 11 °C. The detail of this laser system are discussed elsewhere.[1-4] We will discuss its current condition and performance, along with some issues and repairs.

2.1.1 Oscillator (Vitesse)

The Vitesse is the oscillator laser that generates the pulsed light centered at 800 nm. It has its own pump laser, the Verdi, and is responsible for seeding our regenerative amplifier, the Legend. Thanks to its closed box design, the Vitesse is incredibly stable from day-to-day. Further, its turn-on procedure is very easy and robust. For daily operation, we turn the key to 'on', open the shutter, enter the 'Verdi Light Loop' mode, increase the Verdi power to 1.95 W, and immediately return to the 'Vitesse Light Loop' mode. Increasing the pumping power in the 'Verdi Light Loop' mode boosts mode-locking and returning to the 'Vitesse Light Loop' mode adjusts the output power to a set 290 mW, after it is mode-locked. We chose the 290 mW set-point because we found that higher output powers lead to a significant increase in the noise in our measurements. If the Verdi stays at high power, the Vitesse shuts itself down, giving an error message.

In November 2013, we had trouble with mode-locking the Vitesse. Our normal turn-on procedure failed to achieve mode-locking. Adam Huss, a service technician from Coherent, pointed to the laser's age as a cause of this issue and suggested a few things to try. The only thing that seemed to work was to just repeatedly turn the key on and off until we got mode-locking. Since laser failed to mode-lock more often than it successfully mode-locked, we decided to leave it on after we got mode-locking rather than sending the whole unit to the company for the repair. The strategy of leaving the oscillator on is also employed for the oscillator in 4317.

In April 2015, the Vitesse started to malfunction. To start, the actual output power does not match the power set in the 'Vitesse Light Loop' mode. As mentioned above, we set its power to 290 mW, but the actual power is below this by about 87 mW. However, under the 'Verdi Light Loop' mode, the actual power matches the power set. The reason that we do not use the 'Verdi Light Loop' mode is that this mode monitors only the Verdi power, and keeping the Verdi power at the set point does not necessarily result in a stable output of the Vitesse. As a temporary solution, we increase the set point such that the Vitesse output reaches the desired 290 mW in the 'Vitesse Light Loop' mode. Another problem we encountered was that the power supply unit kept turning on and off by itself and, thus, never warmed up. Adam Huss visited us and diagnosed that the trouble was a malfunction of the 48 V power supply module inside of the power supply unit. He replaced it with a new module and this resolved the problem. The power mismatch between the set point and the actual reading while in the 'Vitesse Light Loop' mode is still present and Adam suggested that we just keep using the high set point, which gives a 290 mW output power we desire. We also found that increasing the Verdi power to the maximum during startup of the Vitesse can result in more successful mode-locking. Coherent limits the maximum power of the Verdi in the Vitesse at 2.2 W; we now use 2.09 W of Verdi power to

produce 290 mW of Vitesse power, which puts us close to the maximum power that we can use for the Verdi. Once we hit this maximum power and cannot obtain 290 mW of Vitesse power, or once it becomes impossible to get mode-locking, the next course of action is to clean and realign the optics in the cavity. To do this, we could send things back to Coherent; however, considering the laser's age and outdated warranty, we would probably attempt the service by ourselves.

2.1.2 Pump laser (Evolution)

The pump laser, the Evolution, is the main culprit of instability and power loss in our laser system, as stated in Preston's thesis.[4] The Evolution is very sensitive to the humidity of the lab, and we can observe fluctuations of about 0.5 W when the lab humidity is high (more than 40% relative humidity). Also, it usually needs to be tuned up every couple of months to maintain its normal working power. However, this tune-up is becoming increasingly less effective as it ages. In Preston's thesis,[4] he mentioned that the Evolution has produced 16 W of green light at 20 A of diode current, but now its output power is less than 12.5 W at 24.6 A of diode current.

We have explored every parameter that can affect the output power of the Evolution and found that the combination of lowering its chiller temperature and increasing the diode current is the most effective way to increase the power. Adam Huss said that as the diode ages, the light tends to red-shift and lowering the temperature of the chiller will blue-shift the diode light back towards its original frequency, leading to a higher output power from the Evolution. While we need to be careful about water condensation inside the Evolution if the chiller temperature drops below the dew point in the lab, according to Adam this will just result in flickering or blinking of the laser beam and not severe damage. Therefore, we are running the chiller at a rather low

temperature (11 °C), which is 6 degrees lower than the temperature we started at, but we have not seen any condensation inside the Evolution, yet.

The maximum current of the Evolution is set to 25 A, and we cannot exceed this value without modifying its factory settings. Presently, we use 24.6 A of diode current, which is quite close to the maximum. I would think that within a year or so, the current will hit the limit and we will have to either use it at a lower-power setting or replace the diode. In addition, there is an issue with ramping up the current. Sometimes, the current does not reach its set point; the gap can be as bad as 8 A. Adam thinks a bad current driver is causing this issue. We used to just let it run for a while when this happened, and it often fixed by itself. Recently, I found that this issue might be from a bad connection inside the Evolution's power supply. There are four thick wires (2-black and 2-red) that deliver the current from the driver to the Evolution. These wires are located inside the supply near the back and are connected to the power socket, and I noticed that wiggling the red wires using a pen brings the currents back to the set point. Wiggling wires when dealing with such high currents is very scary, consequently we need the help of an expert to investigate this issue in more detail.

2.1.3 Amplifier (Legend)

Our regenerative amplifier, the Legend, seems in good shape even though the performance of its oscillator and pump laser are in a decline. We normally tune up this cavity by cleaning its optics whenever we tune up the Evolution. The detailed procedure for this cavity tune-up is well described in Preston's thesis.[4] Yet, tuning up the Legend cavity has also become less effective, mostly because of the significant drop in the output power from the Evolution. Because the low output power of the Evolution makes light amplification inefficient, it takes

more round-trips inside the cavity for the laser pulse to build up enough energy. Hence, the time for dumping the cavity, the Pockels Cell#2 time, increases from 293 ns and is now at 312 ns.

We have modified the air circulating system of the Environmental Control Unit (ECU), because the circulating pump inside the ECU stopped working in 2015. Instead of replacing the broken pump with new one, we decided to use the house N_2 gas that is available in our department. We connected a long tube from the N_2 outlet of the fume hood directly to the circulating loop of the ECU. We regulate the flow speed using a flow meter that is in the circulating loop and set it at ~ 0.5 SCF/min.

2.2 Non-linear light conversion

For the experiments in this thesis, we have used laser light over a broad range of wavelengths; near-IR, mid-IR, the second and third laser harmonics, and broadband UV/VIS. We have used two or three of these types of light in various combinations to serve as photolysis, pump, or probe light in our experiments.

2.2.1 Second and third harmonics

Second and third harmonic generation are simple techniques of light conversion that provide very stable light sources at 400 and 267 nm, respectively. We generate 400 nm light by pumping a β-$BaBO_3$ (BBO) crystal with fundamental light centered at 800 nm and then adjusting the crystal angle to maximize the mixing and give the most energy of 400 nm light. To generate 267 nm light, we use two mixing stages in two separate BBO crystals. The current design of THG is similar to the one described in the Sheps' thesis.[1] The beam size of our fundamental is a bit larger than the area of the face of the crystal, so we use a 3:1 telescope to shrink the beam size.

We typically use the second harmonic, 400 nm, as our single-point probe light, and we also use it for photolysis of Br_2 in the experiments studying Br atom reactions. In the three beam Br atom reaction experiments we want to resolve a small difference in the signals (500 μOD ~ 1 mOD), thus only this stable 400 nm light source with a noise level that can be as small as 10 - 20 μOD works. The third harmonic, 267 nm, is convenient for photolysis of either chlorinated solvents or bromoform.

2.2.2 Broadband UV/VIS continuum

The broadband UV/VIS continuum is very useful for obtaining transient absorption spectra for species during the course of a reaction. We could get the same information using a monochromatic light source, but it would take much more time and effort, as we would have to change the wavelength of the probe multiple times. The tradeoff is that generating stable continuum can be a bit tricky, and using a continuum probe increases the noise level in the transient absorption measurements. Preston described tips in his thesis that help make a nicer, more stable continuum.[4]

We usually focus 800 nm light into a CaF_2 or sapphire substrate to generate VIS continuum that spans from 330 to 700 nm. Since the CaF_2 substrate has a lower damage threshold, we use a small stepper motor to move the CaF_2 substrate between every time delay. If we need probe light that stretches a little further into the UV, we pump the CaF_2 substrate with 400 nm, which gives continuum in the range of ~ 300 - 600 nm.

2.2.3 Near-IR light

We generate near-IR light, spanning from 1.1 to 2.5 μm, using a double-pass β-$BaBO_3$ optical parametric amplifier (BBO OPA). The details of the BBO OPA design are described by Andrew King.[5] The direct output from the BBO OPA is useful for exciting O–H and C–H stretching overtones near 1.5 and 1.7 μm. We produce up to 50 μJ per near-IR pulse at these wavelengths.

2.2.4 Mid-IR light

We generate mid-IR light of ~ 3 - 5 μm to look for product formation in the bimolecular reactions. This wavelength region covers not only the C–H stretch fundamental, but also the H–Cl and H–Br vibrations. We can generate the mid-IR light by either using a $KNbO_3$ OPA or by doing difference frequency generation (DFG) in AgGaS. The $KNbO_3$ OPA uses the fundamental light from the laser to generate the mid-IR light, whereas doing DFG in AgGaS requires that we first generate near-IR light (signal and idler) from the BBO OPA. We have used both methods and have found that the $KNbO_3$ OPA is more stable, giving less noise. This might be because the DFG requires an additional non-linear process that can introduce more noise, but we cannot rule out the bad condition of our AgGaS crystal. We prefer to generate mid-IR light using the $KNbO_3$ OPA; our design is copied from Preston,[4] and it can produce ~10 μJ of idler at 3.3 μm. There is, however, one caveat for generating mid-IR light with our $KNbO_3$ OPA and that is that we can no longer find a replacement of this crystal. There are no companies that we are aware of making and cutting $KNbO_3$ crystals.

2.3 Experimental approaches: light detection and data acquisitions (LabView code)

The experiments described in this thesis all use a pump-probe technique, which depending on the properties and wavelengths of the pump and probe pulses can occur in several variations. In this section, we discuss the combinations of pump-probe detection schemes and the data acquisition used in the study of hydrogen abstraction reactions by Cl or Br atoms.

2.3.1 Three beam experiment with single-point detection

For the study of Br atom-reactions in this thesis, we use three laser pulses: a photolysis pulse at 267 or 400 nm, a near-IR pump pulse at ~ 1500 - 1700 nm, and a probe pulse at 400 nm. We generate these wavelengths utilizing SHG or THG and a BBO OPA as described in the Chapter 2.2. Figure 1 shows a schematic of our three beam experiment. Because we want to see the effects of both the photolysis and the near-IR pump pulses, we need to control these beams and sequence when they are on and off so that we can calculate the difference in the transient absorption signal.

We operate two choppers at 500 and 250 Hz, which are at a half and a quarter of the 1 kHz repetition rate of the Legend. The combination of each chopper state gives four different states as shown in the top of Figure 2: photolysis (on)/near-IR pump (off)/probe (on), photolysis (off)/near-IR pump (on)/probe (on), photolysis (on)/near-IR pump (on)/probe (on), photolysis (off)/near-IR pump (off)/probe (on). We measure the intensity of the probe light under these four conditions and calculate the three transient absorption signals:

the photolysis alone,

$$\Delta A_{phot} = A_{phot} - A_0 = -\log\left(\frac{I^S_{phot}}{I^R_{phot}}\right) + \log\left(\frac{I^S_0}{I^R_0}\right), \qquad (1)$$

the near-IR pump alone,

Figure 1. The schematic of the three-beam experiment with 400 nm, single-point detection.

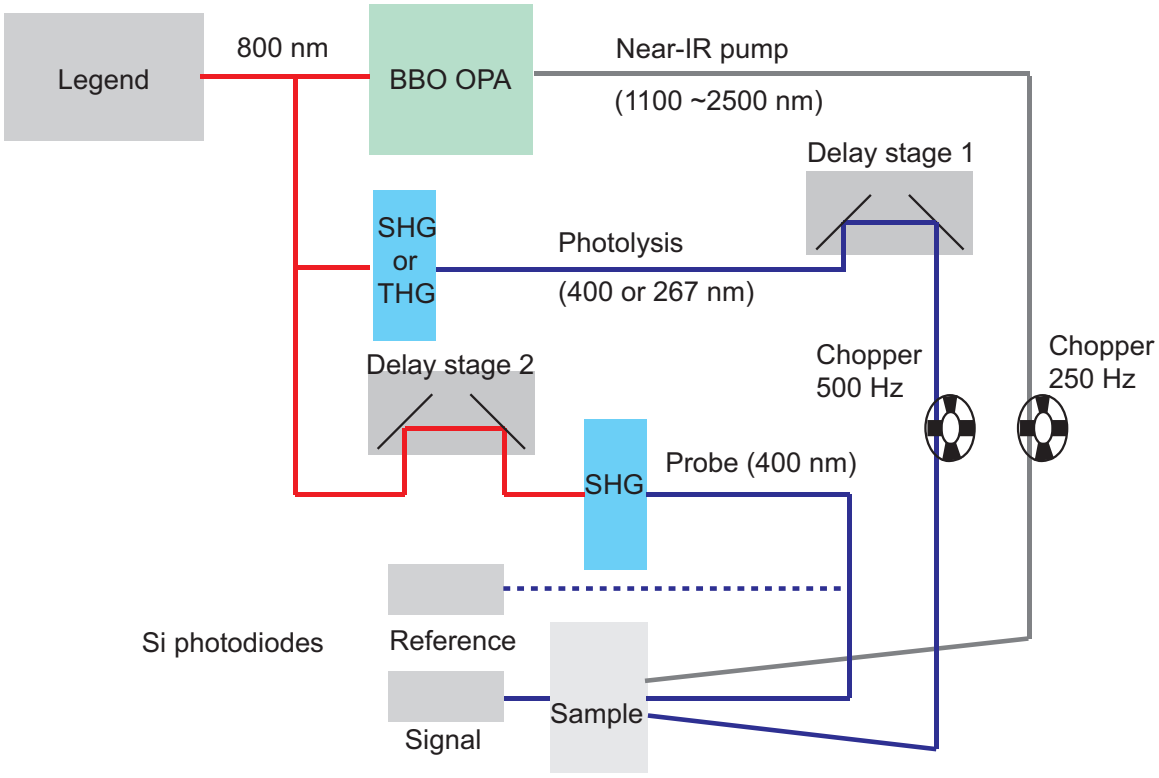
Legend
800 nm
BBO OPA
Near-IR pump
(1100 ~2500 nm)
Delay stage 1
SHG
or
THG
Photolysis
(400 or 267 nm)
Chopper
500 Hz
Chopper
250 Hz
Delay stage 2
SHG
Probe (400 nm)
Si photodiodes
Reference
Sample
Signal

$$\Delta A_{vib} = A_{vib} - A_0 = -\log\left(\frac{I^S_{vib}}{I^R_{vib}}\right) + \log\left(\frac{I^S_0}{I^R_0}\right), \quad (2)$$

and both beams,

$$\Delta A_{phot+vib} = A_{phot+vib} - A_0 = -\log\left(\frac{I^S_{phot+vib}}{I^R_{phot+vib}}\right) + \log\left(\frac{I^S_0}{I^R_0}\right). \quad (3)$$

Finally, we calculate the difference signal by subtracting both (1) and (2) from (3),

$$\Delta\Delta A = \Delta A_{phot+vib} - \Delta A_{phot} - \Delta A_{vib}. \quad (4)$$

Here, I^S and I^R denote the intensity of the probe light on the signal and reference detector, respectively. The subscripts of 'phot', 'vib', 'phot+vib' and '0' mean the photolysis (on), the near-IR pump (on), both beams (on), and both beams (off), respectively. Our LabView code calculates all these transient absorption signals and the difference signal in real time.

Two translation stages control the timing of the photolysis and probe pulses relative to the near-IR pulse; see the bottom of Figure 2. The first translation stage varies the time delay of the photolysis pulse with-respect-to the near-IR pulse, and is shown in Figure 1 as 'delay stage 1' and in Figure 2 as 'delay 1'. Meanwhile, the second translation stage varies the time delay of the probe pulse with-respect-to the near-IR pulse, and is shown in Figure 1 as 'delay stage 2' and in Figure 2 as 'delay 2'. Since we do not scan 'delay stage 1' during the course of the experiments, we use our smaller translation stage (166 ps delay, Newport), leaving our larger translation stage (1.6 ns delay, Aerotech) for 'delay stage 2'.

A pair of single Si photodiodes detects the signal and reference beams, separately. They convert the intensity of the light into a voltage, and the details of their usage and implementation are described in Sheps[1] and Crowther.[2] These photodiodes have seen a great deal of use because they are our most sensitive and least noisy detectors. With the alignment techniques described by

Figure 2. The combinations of two chopper states (top) and timing between the photolysis, near-IR pump, and probe pulses (bottom).

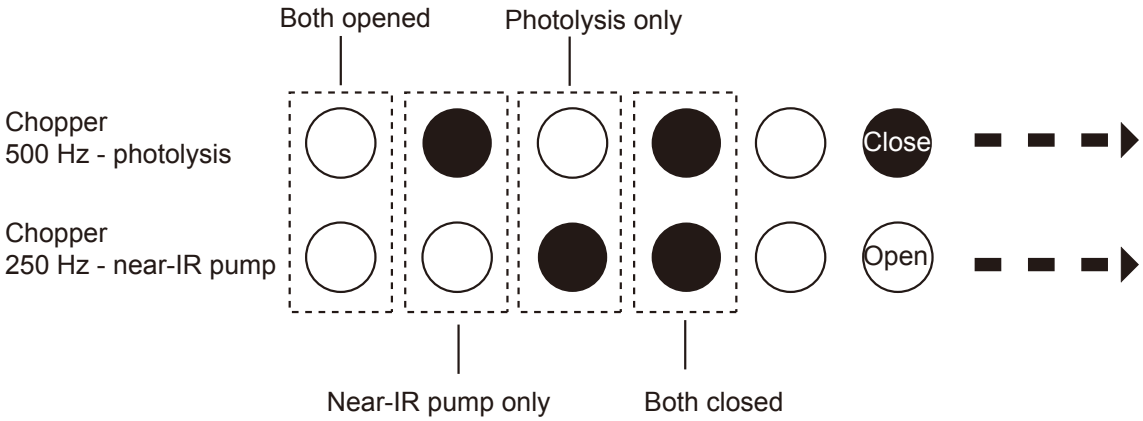
Both opened
Photolysis only
Chopper
500 Hz - photolysis
Chopper
250 Hz - near-IR pump
Close
Open
Near-IR pump only
Both closed

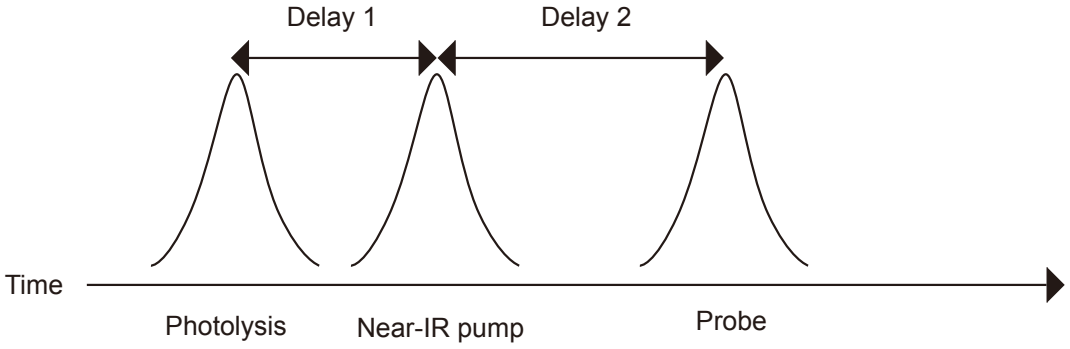
Delay 1
Delay 2
Time
Photolysis
Near-IR pump
Probe

Preston,[4] we can get the noise level as low as 10 μOD for the average of 2000 transient absorption signals. Because of the low noise level, we need to use single-point detection in the three-beam experiments to observe the small difference signals (0.5 ~ 1 mOD).

2.3.2 Broadband UV/VIS continuum probe experiment

Even though the single-point detection provides a good signal-to-noise ratio in the measurement, we often need to see the transient absorption spectrum and its temporal evolution to assign the origin of the absorption feature we observe. We use a pair of 512 pixel Si photodiode arrays and UV/VIS continuum light to carry out this continuum probe experiment. For these experiments, the mechanical shutters control the pulse sequences and the reading of the voltages from the arrays. The theses of Cox[6] and Crowther[2] contain the details of the Si photodiode arrays and the broadband UV/VIS continuum probe experiments; some additional comments are given below.

In our experiments on the Cl atom reactions (Chapter 3), we expand the spectral window of detection to the shorter wavelength region to investigate the dynamics of an unknown photoproduct near 300 nm. In doing so, we observed the 267 nm scatter from photolysis light on the Si photodiode arrays. However, it was not just a sharp negative peak. It showed broad negative-going patterns with multiple peaks and the position of the peak maximum seemed to be inconsistent. This unusual shape is due to multiple scattering events of the photolysis pulse from the CaF_2 windows of the sample cell. Each of the two CaF_2 windows can reflect the photolysis light at their front and back faces. These different scattering events do not appear at the same pixel on the array because they follow different beam paths to the detector. To reduce this interference, we put an iris in the probe beam path right after the sample cell. As we close down

the iris, we block some of scattered light and the scatter signal converges, as expected, to a sharp negative peak near the pixel that corresponds to 267 nm.

In the same set of experiments, we observed the deposition of an unknown photoproduct on the CaF_2 windows that deposition changed the dynamics of the real signal. To avoid this issue, we move the sample cell along the horizontal axis between each time delay so that we are looking at a clean spot on the window at each time delay. The small stepper motor, which we use for moving the CaF_2 substrate in the continuum generation, also works great for moving the sample cell.

Finally, in our experiments on the Br atom reactions (Chapter 4), we have set up a three-beam experiment that also uses the UV/VIS continuum probe and the Si photodiode arrays. The pulse sequences and the shutter states for these three beam experiments are well explained in Preston's thesis.[4] Unfortunately, the shot-to-shot noise we experience is much worse (about 1 or 2 mOD) than that of the single-point detection, and we were not able to observe any difference signal.

2.3.3 Broadband IR probe experiment

We use time-resolved IR spectroscopy to study the hydrogen abstraction reactions of Cl atoms in Chapter 3. The basic scheme of this experiment is similar to Orr-Ewing and coworkers,[7] except for the specification of mercury-cadmium-telluride (MCT) array detector and the IR optical parametric amplifier (OPA); they use a 128 pixel MCT array detector and a commercial IR OPA, whereas we use a 64 pixel MCT array detector and our homebuilt $KNbO_3$ OPA.[7]

Our group has quite recently started to use the MCT array detector, and we only have one publication (in 2013) that uses this detector.[8] T.J. Preston, a former graduate student, made large

progresses toward advancing our knowledge of these MCT array detectors, and he set up the current operation, data acquisition, and post-manipulation of the data from the array detector.[4] Because the responses of each pixel in the arrays are different, there is an offset for each pixel, which usually appears as a linear function across the arrays. Additionally, our 64-pixel array detector is, in fact, two 32-pixel units side by side, and both of these units have a different IR response. Therefore, we need to adjust for this baseline offset in each unit separately, after data collection. In the LabView code written by Preston for post-manipulation of the data, we fit our raw data with a linear or first order polynomial function using the first and last two pixels of each 32-pixle array unit separately, and subtract the fitted values from the raw data to remove the baseline offset. This method provided reliable data processing in our previous study on the isomerization of halomethanes. However, we found that if there is signal at the edges of the array, it gets exaggerated by this procedure. As shown in Figure 3, if there is a negative going signal near the end of the arrays, the baseline correction procedure of Preston raises up that signal. This exaggerates the signal, while making the negative feature at the edge of the detector less prominent. These manipulations sometimes result in assigning an artifact as real signal. For the systems that we discuss in this thesis, using the edge pixels to fit the baseline is not reliable. Particularly in the reactions of Cl atoms, the transient absorption spectrum reveals complicated features for the HCl signals (v=0 and v=1) and the interference from solute absorptions. The complicated spectra that we are trying to untangle had required us to modify our method for the baseline fitting.

In 2014, we improved our LabView code for data acquisitions and manipulations. Ryan Kieda, another former graduate student, introduced the KOALA (Kinetics Observed After Light Absorption) program[9] to the group, after visiting the Orr-Ewing group in Bristol. One of the key

features of this program is its baseline fit function, which has proven to provide more reliable data processing. In KOALA, we can choose up to five pixel-ranges for the baseline fit. Therefore, we can avoid regions where signal exists and remove the baseline offset without loosing any important information from the data (Figure 3). We have implemented an early version of KOALA, and its associated LabView codes, to our old LabView code, allowing us to collect baseline corrected data (that we are confident in) in real time. We also use KOALA for post-processing.

Another improvement made to our LabView code is the ability to take a scan with randomly ordered delay times. This is especially useful when there is unwanted deposition on the cell windows, like in the reaction of Cl atoms described in Chapter 3. Taking scans with the random delay times averages over the effects of the unknown species to minimize its contribution to our data; we average multiple scans for the traces analyzed.

Finally, we have also set up the three-beam experiment for studying Br atom reactions using the broadband IR probe and the IR array detector (Figure 4). This experiment is the ultimate goal of the condensed phase bimolecular reaction lab, and we tried, for the first time, to look at the production of HBr from a vibrationally driven reaction. We have modified our LabView codes so that we calculate three transient absorption spectra and the difference spectra based on the equations (1) – (4). Contrary to the broadband UV/VIS probe experiment, the noise is not an issue for this IR probe, three-beam experiment because the $KNbO_3$ OPA is very stable. Using the average of 50,000 transient absorption measurements, we are able to get ~10 μOD variations across the arrays in the difference spectrum as shown in Figure 5. Regrettably, we have not found any signature of HBr production. We think that this is most likely due to the small magnitude of the HBr signal. We intend to pursue this signal for a while longer. When we

Figure 3. The comparison between the transient absorption spectra obtained from the old and new baseline fitting methods. Both transient absorption spectra come from the same raw data, but their baselines are corrected for in a different manner.

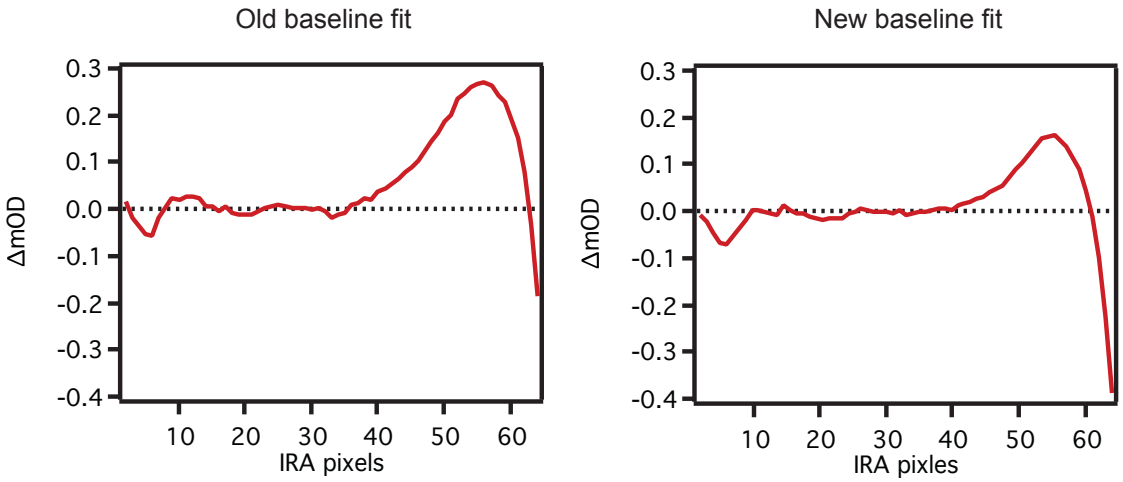
Old baseline fit
New baseline fit
ΔmOD
0.3
0.2
0.1
0.0
-0.1
-0.2
-0.3
-0.4
10
20
30
40
50
60
IRA pixels
IRA pixles

Figure 4. The schematic of the three-beam experiment with broadband IR detection.

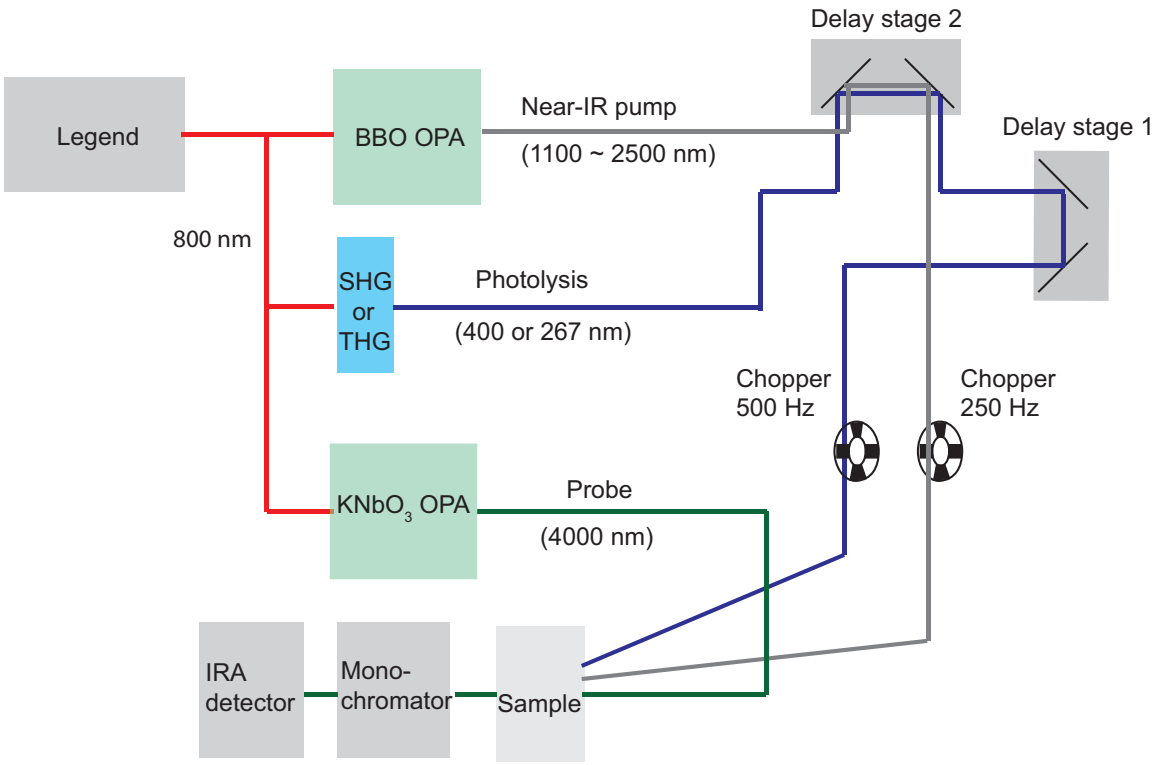
Delay stage 2
Legend
BBO OPA
Near-IR pump
(1100 ~ 2500 nm)
Delay stage 1
800 nm
SHG
or
THG
Photolysis
(400 or 267 nm)
Chopper
500 Hz
Chopper
250 Hz
KNbO3 OPA
Probe
(4000 nm)
IRA
detector
Mono-
chromator
Sample

Figure 5. The noise level in the difference signal of the three-beam experiment with the broadband IR probe.

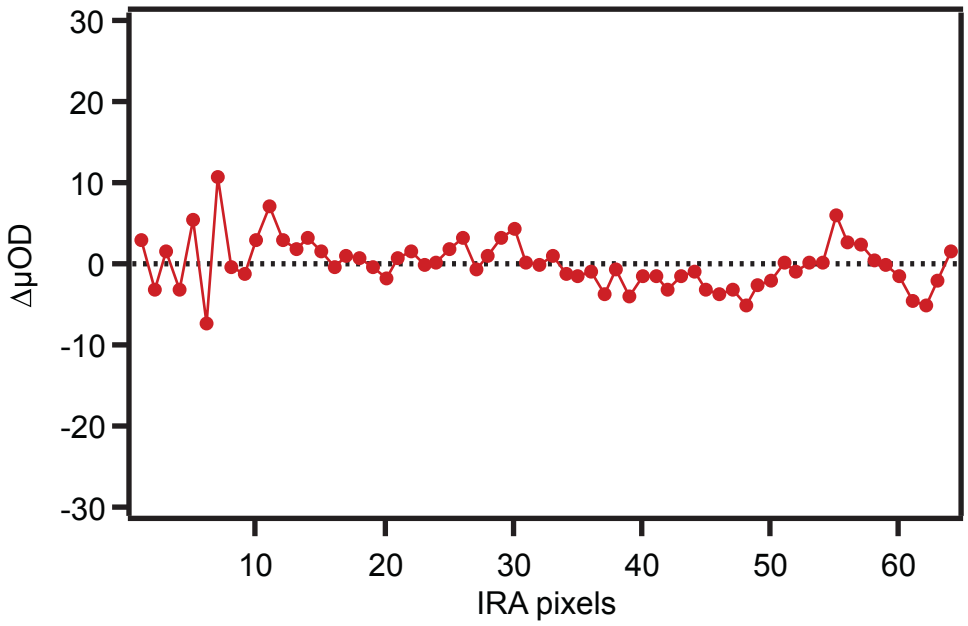
30
20
10
0
-10
-20
-30
ΔμOD
10
20
30
40
50
60
IRA pixels

attempted this experiment, we were still using the old baseline fitting method. Perhaps, implementing the new baseline fitting procedure into the data acquisition of three-beam experiment will allow us to find the tiny signal from the products of the vibrationally driven reaction.

References

(1) Sheps, L., University of Wisconsin-Madison, 2005.

(2) Crowther, A. C., University of Wisconsin-Madison, 2008.

(3) Carrier, S. L., University of Wisconsin-Madison, 2009.

(4) Preston, T. J., University of Wisconsin-Madison, 2012.

(5) King, A. M., University of Wisconsin-Madison, 2001.

(6) Cox, M. J., University of Wisconsin-Madison, 2006.

(7) Abou-Chahine, F.; Greaves, S. J.; Dunning, G. T.; Orr-Ewing, A. J.; Greetham, G. M.; Clark, I. P.; Towrie, M. *Chem. Sci.* **2013**, *4*, 226.

(8) Preston, T. J.; Shaloski, M. A.; Crim, F. F. *J. Phys. Chem. A* **2013**, *117*, 2899.

(9) Grubb, M. P.; Orr-Ewing, A. J.; Ashfold, M. N. R. *Rev. Sci. Instrum.* **2014**, *85*, 064104.

Chapter 3

Time-Resolved Spectroscopic Studies of Cl Atom Reactions with 2,3-Dimethylbutane, 2,3-Dimethyl-2-butene, and 2,5-Dimethyl-2,4-hexadiene in Solution

3.1 Introduction

The reactions of Cl atoms with various organic molecules are of interest in gas phase studies because of their importance in atmospheric chemistry. Reaction of Cl atoms with hydrocarbons in the stratosphere prohibits the catalytic destruction of stratospheric ozone by sequestering Cl atoms and forming the reservoir compound, HCl.[1] Also, the sea-salt aerosol releases Cl_2 by oxidation of Cl^- ions and subsequent photolysis of Cl_2 produces Cl atoms in the marine boundary layer. These Cl atoms initiate oxidation of hydrocarbons and contribute to ozone formation.[2]

Fundamentally, reactions of Cl atoms with small hydrocarbons are prototypical examples for understanding reaction mechanisms and testing theoretical work on reaction dynamics. The vast majority of experimental and theoretical work on Cl atom reactions investigate Cl reacting with alkanes, and thus these reaction mechanisms are known in great detail. In particular, the reactions of Cl atoms with methane (or its isotopologues) have been extensively studied, with the

state-to-state reaction dynamics and bond- and vibrational mode-specific chemistry being established.[3,4]

The reaction between Cl atoms and alkenes, on the other hand, have not been as well studied, even though it has equal importance in atmospheric chemistry.[5] Furthermore, the reactions of Cl atoms with alkenes have richer chemistry than the reactions with alkanes. In alkane reactions, the direct hydrogen abstraction is the only possible reaction channel; however in the reactions between Cl atoms and alkenes, the addition of Cl to a C=C bond can also occur, along with subsequent elimination of HCl (addition–elimination or indirect hydrogen abstraction). In the gas phase, the relative contribution of each of these pathways depends on the thermodynamics of a given reaction and the experimental conditions, such as temperature and pressure.[5] Distinguishing between direct and indirect hydrogen abstractions is not easy, because both channels produce the same reaction products. In a recent gas phase velocity-map ion imaging study, Preston *et. al*. observed bimodal rotational distribution of HCl (v=0) products from the reaction of Cl atoms with propene.[6] Based on direct-dynamics simulations, they attributed this distribution to the presence of two different reaction mechanisms, direct and indirect hydrogen abstraction.[6] They also found that these two reaction channels are connected *via* a loose transition state (TS) associated with large excursions of the Cl atom from the equilibrium geometry of the Cl-propene addition complex.[6] Likewise, Jolland *et. al*. reported roaming-like dynamics in the addition–elimination reactions of Cl atoms with isobutene.[7] Despite these insights, there is still debate as to whether the direct or indirect pathway dominates the overall reaction dynamics.

By virtue of recent improvements in transient IR absorption spectroscopy there has been great progress in the condensed phase studies of bimolecular reactions,[8,9] still these studies are

limited. Since Hochstrasser and coworkers made the first observation of HCl formation from Cl atom reaction with cyclohexane in real time (with ps time resolution),[10] there have only been a few studies of Cl atom reaction dynamics that monitor product formation.[11,12] Moreover, there were no condensed phase studies of Cl atoms with alkenes until Orr-Ewing and coworkers reported the time-resolved IR measurements of Cl reactions with 2,3-dimethyl-2-butene (DMBE) in chlorinated solvents.[12] Additionally, this study observed for the first time the formation of vibrationally excited HCl products in the condensed phase.

Herein, we report the reaction dynamics of Cl atom reactions with 2,3-dimetylbutane (DMB) and 2,5-dimethyl-2,4-hexadiene (DMHD) in chlorinated solvents. As shown in Figure 1, DMB has a similar structure to that of DMBE, but is a saturated hydrocarbon. In DMHD, there are four methyl substituents as in DMBE, but it has one more C=C bond. Therefore, this series of molecules allows for a systematic comparison of their reaction dynamics with an increase in the number of C=C bonds and molecular complexity. For the reaction of Cl atoms with DMHD, we observe vibrationally excited HCl products in the v=1 level and their greater productions than in the reaction between Cl atoms and DMBE. In addition, the reaction between Cl atoms and DMHD exhibits larger bimolecular reaction rate coefficient ($\sim 10^{11}$ $M^{-1}s^{-1}$), exceeding a common diffusion-limited reaction rate, compared to the reaction of Cl atoms with DMBE. Our quantum calculations show that the energy profiles of both reactions are similar. Thus, the influence of C=C bond on encountering reactants and the difference in the molecular geometries may enhance the rate of the reaction between Cl atoms and DMHD. Interestingly, the reaction rates measured in this study show a nonintuitive solvent dependent behavior within a conventional diffusion-limited regime. It probably requires a more sophisticated model to understand this trend.

Figure 1. Hydrogen abstraction reaction channels of DMB, DMBE, and DMHD and their calculated ΔE values.

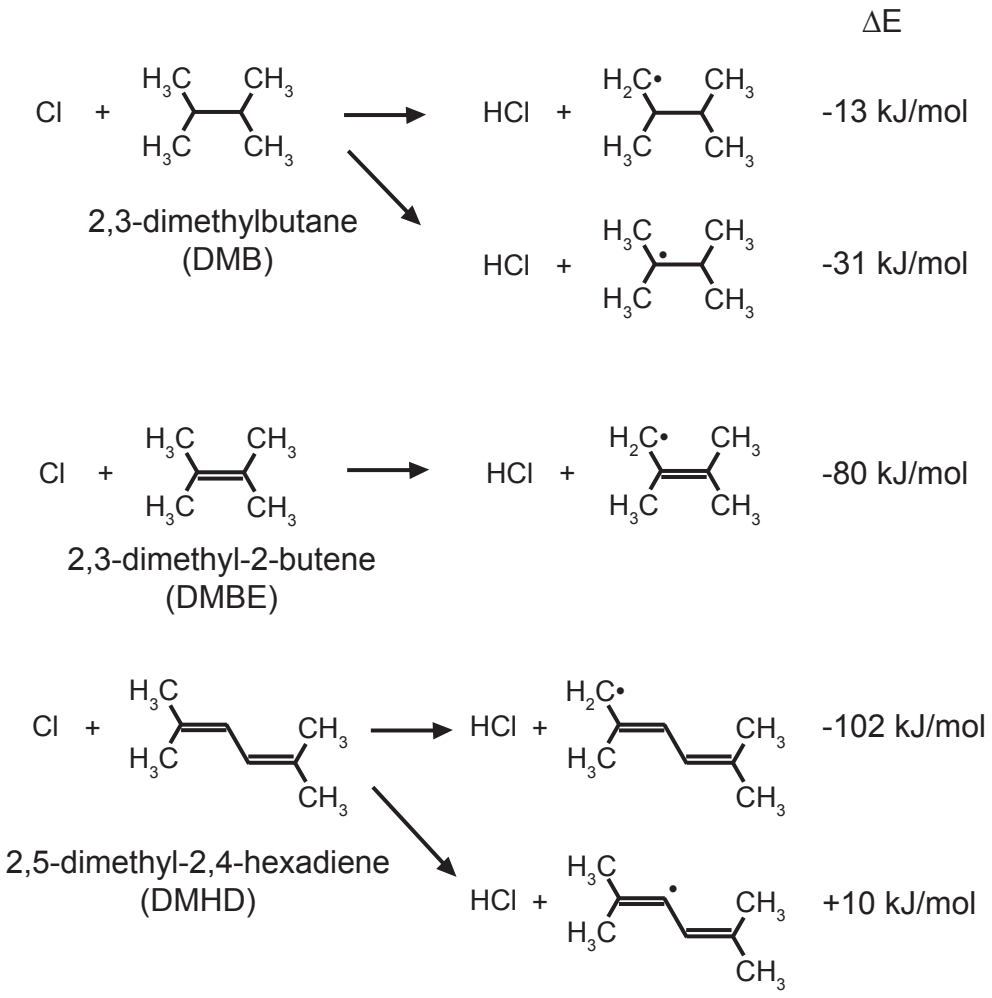
ΔE
Cl +
HCl +
-13 kJ/mol
2,3-dimethylbutane
(DMB)
HCl +
-31 kJ/mol
Cl +
HCl +
-80 kJ/mol
2,3-dimethyl-2-butene
(DMBE)
Cl +
HCl +
-102 kJ/mol
2,5-dimethyl-2,4-hexadiene
(DMHD)
HCl +
+10 kJ/mol

3.2 Experimental methods

We use 2,3-dimethylbutane (DMB) (Aldrich, 98%), 2,3-dimethyl-2-butene (DMBE) (Aldrich, 98%), 2,5-dimethyl-2,4-hexadiene (DMHD) (Aldrich, 96%), CCl_4 (Sigma-Aldrich, Reagent grade 99.9%), and $CDCl_3$ (Aldrich, 99.8 atom % D) as received. For these experiments, the concentrations of DMB and DMBE are 0.2, 0.5, and 0.75 M, whereas we use lower concentrations of DMHD (0.1, 0.2, and 0.35 M) to avoid the formation of photoproduct, as described below.

The apparatus for broadband infrared transient absorption measurements is similar to that used in our recent condensed phase study of photoisomerization of polyhalomethanes.[13] The third harmonic of an ultrafast Ti:sapphire laser provides 267 nm photolysis light with a 1 kHz repetition rate. We use 1 μJ of photolysis light to photolyze the CCl_4 or $CDCl_3$ solvent molecules and generate Cl atoms in solution, thus initiating a reaction. For these broadband infrared probe experiments, a continuum-seeded double-pass optical parametric amplifier using a potassium niobate crystal generates tunable probe light near 3.6 μm, which covers the fundamental (v=1 ← v=0) and excited state (v=2 ← v=1) transitions of HCl. The photolysis and probe paths cross each other in the sample solution at a small angle and a computer-controlled mechanical translation stage controls the time delay between the two pulses. A peristaltic pump flows the sample solution through a cell with MgF_2 windows and a 300 μm thick polytetrafluoroethylene spacer. A 0.25 m Ebert monochromator equipped with a 300 grooves/mm grating disperses the infrared probe light onto a 64 pixel mercury-cadmium-telluride array detector. We calibrate the array detector using the absorption peaks of 1,4-dioxane, which is contained in a thin space between two CaF_2 windows. The resolution of the array detector is about 2.1 cm^{-1}/pixel in this wavelength region, giving a spectral width of roughly 134.4 cm^{-1} (2.1 cm^{-1}/pixel × 64 pixel).

Since capturing both the ground and excited state bands of HCl simultaneously requires a spectral width of about 200 cm^{-1}, we take two separate scans each using a different spectral window of the probe beam and merge these two scans during data processing. We calculate a transient absorption spectrum from the probe signals with and without the photolysis pulse using a mechanical chopper that operates at one-half of the laser repetition rate. We average 10,000 transient absorption spectra at each time delay, and we use a total of 46 time delay points to create one scan. The data presented in this study are the average of three scans.

Between each data acquisition cycle, corresponding to collection of 1,000 transient absorption spectra, a small DC gear motor translates the sample cell perpendicular to the direction of the probe beam to avoid deposition of unknown photoproduct on the cell windows. In addition, the time delay steps are randomly ordered and both the photolysis and probe beams are blocked while the translation stage moves to the next time delay position to minimize the formation of photoproduct. We are particularly careful with the DMHD solutions, as with high concentrations and long irradiation times we have observed deposition onto the windows. The transient absorption bands of HCl are not present when this unknown photoproduct deposits onto the windows. We ensure that all of the transient absorption spectra look normal, without any interference from photoproduct, although we do not notice any deposition in the DMB and DMBE solutions. For the same reason, we clean the MgF_2 windows before and after each scan and make a fresh sample solution for each experiment.

The details of our broadband electronic transient absorption apparatus are described elsewhere.[13] Briefly, we generate UV/VIS continuum probe light by focusing 400 nm light (which is the second harmonic of the Ti:sapphire laser) into a CaF_2 substrate. The continuum spans from roughly 280 nm to over 600 nm. We split the continuum light using a neutral density

filter to generate reference and signal beams; the signal passes through the sample, whereas the reference does not. Both beams are dispersed onto a pair of 512 pixel Si photodiode arrays by 600 grooves/mm holographic gratings enclosed in a modified Czerny-Turner spectrometer. Fast mechanical shutters block and unblock the photolysis and probe pulses such that we can calculate the transient absorption based on the reference corrected probe signals with and without the photolysis pulse.

We use KOALA (Kinetics Observed After Light Absorption), recently developed by Grubb *et. al*.,[14] for post data processing of both the IR and UV/VIS transient absorption data. For the analysis of the IR probe data, we use KOALA to subtract the negative-time signal and use a linear (or quadratic) baseline fit of the raw experimental spectrum to eliminate the contributions from baseline offsets. In the data processing of the UV/VIS continuum probe, we use KOALA to correct the negative-time signal of the raw spectrum and to deconvolute the Cl-solvent complex absorption band from the absorption of unknown species by fitting Gaussian curves to the experimental transient absorption spectrum.

We use the Gaussian09 suite of programs[15] to perform *ab initio* calculations on the isolated and implicitly solvated reactants, products, and possible entrance and exit channel complexes. Since there are no thermodynamic data available for the reactions of DMB, DMBE, and DMHD with a Cl atom, we use the CBS-QB3 method to estimate the overall reaction energy with a high degree of accuracy. This method extrapolates the energy to the complete basis set limit based on a series of single-point energy calculations with various basis sets and is widely used for the calculations of reaction energetics due to its high thermochemical accuracy (~ 2 kcal mol^{-1}).[6,7,16] To calculate the energy profiles, we use density functional theory (B3LYP) with a 6-311G++ (d,p) basis set to determine the energy of all local minima and the transition state of

each reaction and apply the implicit solvent model, IEFPCM (polarizable continuum model using the integral equation formalism variant) to account for the solvent effects of CCl_4, $CHCl_3$, and CH_2Cl_2. We verify the validity of the transition state by the presence of one imaginary vibrational frequency, and an IRC (intrinsic reaction coordinate) calculation confirms that the transition state connects the local minima for each reaction.

3.3 Results

Although there are no available experimental values for the overall energy change (ΔE) of the Cl reactions with DMB, DMBE, and DMHD, we estimate them from the quantum calculations with the CBS-QB3 method to compare the energetics of these reactions. Figure 1 shows the possible reaction pathways of hydrogen abstraction reactions and their calculated ΔE values. For DMB, there are two hydrogen abstraction channels because it has two distinct types of hydrogen atoms, 12 hydrogens bonded to primary carbons and 2 hydrogens bonded to tertiary carbons. Abstraction of either type of hydrogen has a relatively mild exoergicity, with the calculated ΔE being -13 or -31 kJ/mol for the abstractions from primary carbons and from tertiary carbons, respectively. The hydrogen abstraction from the tertiary position is more exoergic because it produces a more stable tertiary alkyl radical (in comparison to a primary alkyl radical generated by hydrogen abstraction from a primary carbon). However, neither abstraction channel can provide enough energy to populate a quantum of vibrational excitation in HCl. Formation of HCl (v=1) requires 34.5 kJ/mol, as deduced from the IR absorption center frequency in the gas phase (2880 cm^{-1}).

For the Cl atom reaction with DMBE, there is only one abstraction channel. Namely, abstraction of an allylic hydrogen from one of the four methyl groups. The calculation shows that

ΔE = -80 kJ/mol for this reaction. The large exoergicity in the reaction with DMBE is attributed to the formation of a resonance stabilized allylic radical. The calculated ΔE is consistent with that estimated by Preston *et. al.* from their CBS-QB3 calculations.[6] In gas phase experiments, the reaction produces vibrationally excited HCl up to v=2, although given the reaction energetics (ΔE) and the collision energy there is roughly 116 kJ/mol of excess energy, enough to populate the v=3 level.[6] In the condensed phase study, however, only HCl in v=0 and v=1 are detected, which is still one less quantum than predicted by ΔE (-80 kJ/mol) without a consideration of the collision energy.[12]

There are two abstraction channels for the Cl reaction with DMHD; the Cl atom can abstract either the allylic or vinylic hydrogen atom. The vinylic hydrogen abstraction is endoergic by 10 kJ/mol and is likely not the major path. We expect that the vinylic hydrogen abstraction does not contribute significantly to our experiments. As in the reaction with DMBE, the allylic hydrogen abstraction from DMHD is highly exoergic by 102 kJ/mol. The calculated ΔE for this allylic hydrogen abstraction reaction is well above the energy required for populating the v=2 state of HCl, but it is just below the energy of the v=3 state. Therefore, if following the same trend as in the DMBE reaction, we would expect to see vibrationally excited HCl products in the Cl reaction with DMHD, with population up to v=1 in the condensed phase. Our results, described below, show that this is indeed the case.

3.3.1 Reaction of Cl atoms with 2,3-dimethylbutane (DMB)

We initiate reaction by photolytically preparing Cl atoms in the sample solution. In this study, we generate Cl atoms by two-photon photolysis of the chlorinated solvents CCl_4 and $CDCl_3$ at 267 nm. Abou-Chahine *et. al.* have recently investigated the detailed dynamics of

photodissociation and isomerization of liquid CCl_4 and $CHCl_3$.[17] Two-photon excitation of CCl_4 (or $CHCl_3$) at 267 nm cleaves a C–Cl bond resulting in fragments of CCl_3 (or $CHCl_2$) and Cl. The nascent Cl atom immediately forms a charge-transfer complex with surrounding solvent molecules, Cl–CCl_4 (or Cl–$CHCl_3$). The Cl-solvent complex can recombine to re-form the parent molecule, or it can isomerize to form *iso*-CCl_3–Cl (or *iso*-$CHCl_2$–Cl). Transient absorption bands at 330 and 500 nm were assigned to the absorption of the Cl-solvent complex and the isomer, respectively. Using these spectral signatures, the authors mapped out a complete picture of photoinduced reactions in liquid CCl_4 and $CHCl_3$. Over the course of photodissociation, recombination, and isomerization, if the Cl atoms encounter a reaction partner, like an alkane or an alkene, reaction will occur because these exothermic reactions are diffusion-limited. In previous studies, we have successfully demonstrated our ability to follow reactions of Cl atoms with alkanes and alcohols following photolysis of Cl_2 at 350 nm or two-photon photolysis of CCl_4 and CH_2Cl_2 at 267 nm in real time utilizing ultrafast spectroscopy in the ultraviolet and visible to monitor the decay of the above mentioned Cl-solvent complex.[11,18] We have also successfully monitored the evolution of the HCl product as a function of time delay using time-resolved infrared spectroscopy, which provides picosecond time resolution with vibrational mode selectivity.[11]

Figure 2 shows contour plots of transient absorption measurements and their spectra at selected time delays for reaction of DMB in CCl_4 and $CDCl_3$. In the transient absorption measurements of a 0.5 M DMB solution in CCl_4, an absorption band at 2830 cm^{-1} grows in as the time delay increases. In the $CDCl_3$ solution, a broader band at 2820 cm^{-1} appears and grows in intensity with an increase in time delay. The peak positions of these bands match those of the steady-state absorption peaks of HCl in CCl_4 and $CDCl_3$,[12] although there are interferences from

Figure 2. Contour plots of transient absorption (top) and the corresponding spectra at selected time delays (bottom) for the reaction of Cl with 0.5 M DMB in (a) CCl_4 and (b) $CDCl_3$.

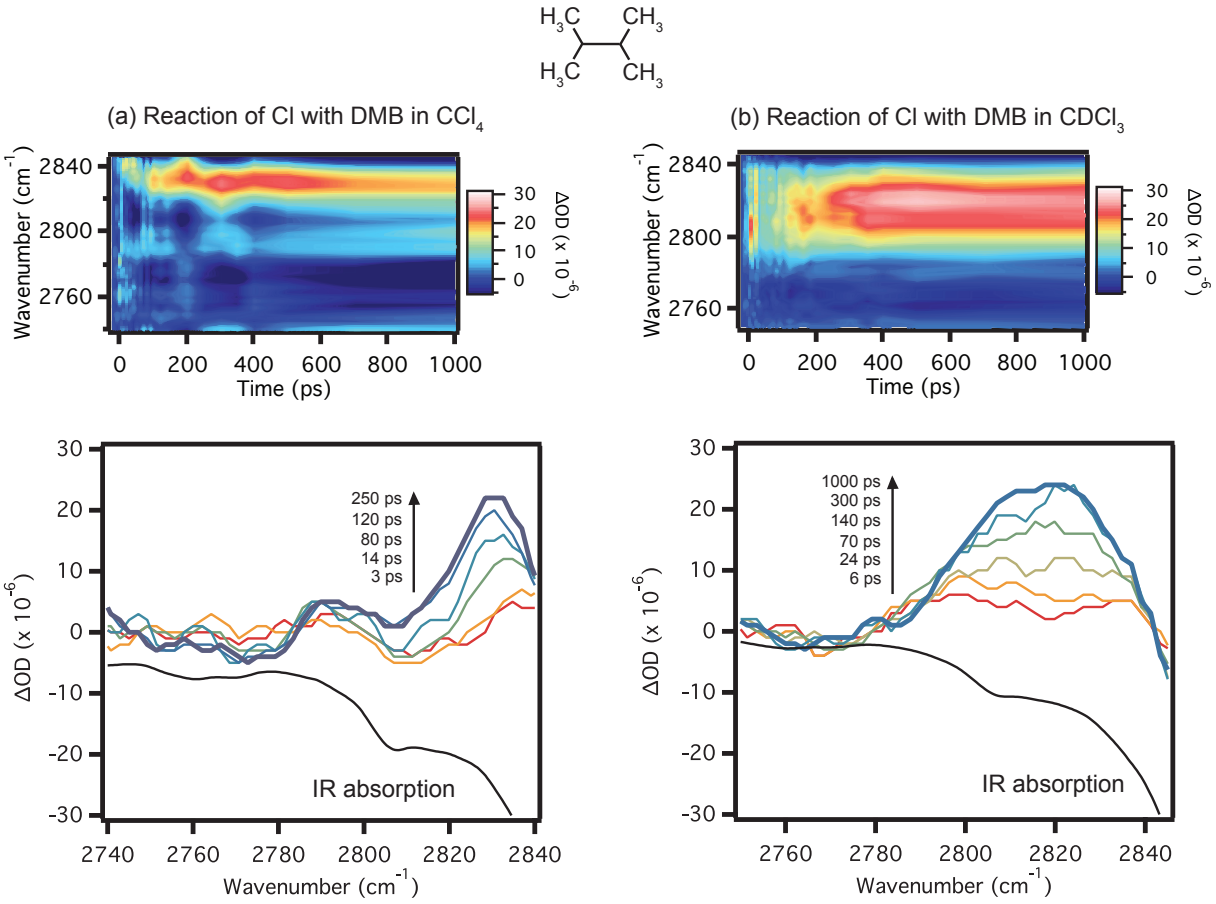
H3C CH3
H3C CH3
(a) Reaction of Cl with DMB in CCl4
(b) Reaction of Cl with DMB in CDCl3
Wavenumber (cm-1)
Time (ps)
ΔOD (x 10-6)
250 ps
120 ps
80 ps
14 ps
3 ps
1000 ps
300 ps
140 ps
70 ps
24 ps
6 ps
IR absorption
ΔOD (x 10-6)
Wavenumber (cm-1)

the changing absorption of DMB in the transient absorption spectra. Since the HCl peak resides close to the large absorption feature of DMB that starts at 2780 cm^{-1}, interference from DMB is inevitable and acts as a negative-signal in the transient absorption spectrum. The negative-signal from absorption of DMB at 2807 cm^{-1} and the blue shift of the HCl absorption peak in CCl_4 make the transient absorption band look narrower than in $CDCl_3$. As expected from the calculated ΔE, we do not observe the v=2 ← v=1 hot band that would appear about 105 cm^{-1} lower than the fundamental (v=1 ← v=0). In order to analyze the time evolution of the HCl molecule to infer the reaction dynamics, we integrate the intensities of 10 pixels (corresponding to 21 cm^{-1}) around the band maximum and display this integrated intensity against time delay, as shown in Figure 2. The growth rate and magnitude of the HCl band depend on the DMB concentration, implying a bimolecular reaction. We model our kinetic scheme on work from Orr-Ewing and coworkers[12] and use a global-fitting program to analyze simultaneously the time traces of the three different concentrations studied. The kinetic model accounts for three categorized processes: in-cage reactions, diffusion processes, and in-bulk reactions. The Cl atoms created *via* photolysis can promptly react with their nearest reaction partners; these reactions will occur on a very fast time scale before the Cl atoms can escape from their first solvation cage (in-cage reactions). The remaining Cl atoms that do not react within the first solvation cage will diffuse out of the cage to the bulk solvent (diffusion) and will react on a relatively slow time scale with reaction partners within the bulk solvent (in-bulk reactions). We represent these processes through a series of chemical reactions, each with an associated rate constant, as shown below.

In-cage reaction:

$$Cl_c + RH \xrightarrow{k_{0c}} HCl\,(v=0)_c + R \qquad (1a)$$

Diffusion:

$$Cl_c \xrightarrow{k_d} Cl_b \qquad (1b)$$

$$HCl\ (v=0)_c \xrightarrow{k_d} HCl\ (v=0)_b \qquad (1c)$$

In-bulk reaction:

$$Cl_b + RH \xrightarrow{k_{0b}} HCl\ (v=0)_b + R \qquad (1d)$$

Here, we use the same notation as Orr-Ewing and coworkers;[12] the subscripts of c and b denote a species (or a reaction) in the cage and in the bulk, respectively, the subscript d denotes a diffusion process, and the subscript 0 denotes a reaction producing HCl (v=0). We assume that the concentration of RH (hydrogen donor) is much larger than that of Cl, thus k_{0c} and k_{0b} are the pseudo first order rate constants. We numerically integrate these equations to fit our integrated intensity data. We constrain the diffusion rate constant, k_d to values that lie within the error range obtained by Abou-Chahine *et. al*. from the fit of their DMBE experimental data.[12] This kinetic model fits nicely with our experimental data, as illustrated with solid lines in Figure 3. We summarize the resulting rate coefficients in Table 1. Note that K_{0c} and K_{0b} are the corresponding bimolecular reaction rates given by dividing the pseudo first order rate constants, k_{0c} and k_{0b}, by the DMB concentrations. The bimolecular reaction rate in the bulk, K_{bi}, is the same as K_{0b} for the DMB reaction because no HCl (v=1) is produced. However, $K_{bi} = K_{1b} + K_{0b}$ if a reaction produces both HCl (v=0) and (v=1), as is the case for the DMBE and DMHD reactions. The uncertainties of each rate coefficient are the standard deviations from the average of each rate coefficient obtained by fitting three sets of data, where each set contains three different concentrations. The K_{bi} for the reaction of DMB and Cl in CCl_4 and $CDCl_3$ are 1.5 (± 0.5) × 10^{10} $M^{-1}s^{-1}$ and 0.7 (± 0.1) × 10^{10} $M^{-1}s^{-1}$, respectively (Table 1). These values are comparable to

Figure 3. Time dependent integrated intensities of the HCl (v=0) band for the reaction of Cl with varying concentrations of DMB in (a) CCl_4 and (b) $CDCl_3$. The concentrations of DMB are 0.2 M (black), 0.5 M (red), and 0.75 M (blue). The solid lines are the fit from the kinetic model.

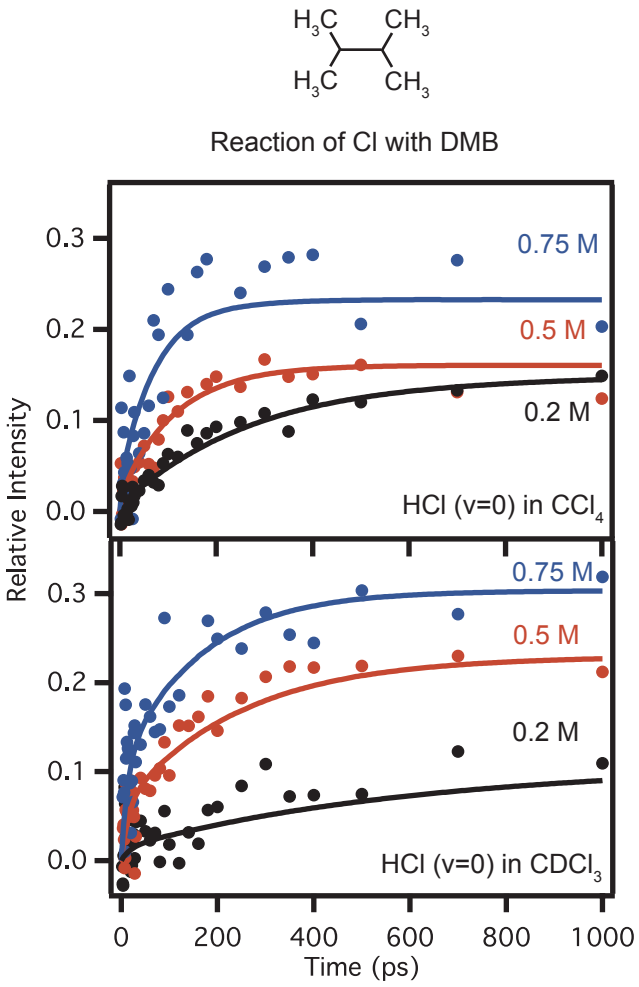
H3C CH3
H3C CH3
Reaction of Cl with DMB
0.75 M
0.5 M
0.2 M
HCl (v=0) in CCl4
0.75 M
0.5 M
0.2 M
HCl (v=0) in CDCl3
Relative Intensity
0.0
0.1
0.2
0.3
0
200
400
600
800
1000
Time (ps)

Table 1. Bimolecular reaction coefficients (in 10^{10} $M^{-1}s^{-1}$) and HCl (v=1) branching ratios for the reaction of Cl with DMB, DMBE, and DMHD in CCl_4 and $CDCl_3$.

	DMB		DMBE		DMHD	
	CCl_4	$CDCl_3$	CCl_4	$CDCl_3$	CCl_4	$CDCl_3$
K_{1c}	-	-	8.1 ± 0.4	9.1 ± 2.5	22.3 ± 1.1	21.7 ± 5.8
K_{0c}	6.7 ± 1.9	4.4 ± 0.3	54.5 ± 0.6	30.3 ± 1.9	66.8 ± 3.4	26.2 ± 4.7
K_{1b}	-	-	0.9 ± 0.2	0.4 ± 0.2	2.2 ± 0.7	0.3 ± 0.1
K_{0b}	1.5 ± 0.5	0.7 ± 0.1	2.7 ± 0.1	1.3 ± 0.4	15.3 ±0.9	6.4 ± 1.5
K_{bi}	1.5 ± 0.5	0.7 ± 0.1	3.6 ± 0.3	1.7 ± 0.6	17.5 ± 1.6	6.7 ± 1.6
Γ (v=1)	-	-	0.14 ± 0.01	0.23 ± 0.05	0.23 ± 0.06	0.40 ± 0.12

bimolecular reaction rates for other alkanes in the condensed phase. For example, the bimolecular reaction rate for the reaction of *n*-pentane with Cl is 7.7 (± 2.1) × 10^9 $M^{-1}s^{-1}$ in CCl_4.[11,18] However, they are an order of magnitude smaller than those of the gas phase congener; the gas phase reaction rate of DMB and Cl is 12.4 (± 0.4) × 10^{10} $M^{-1}s^{-1}$.[19] This follows the same trend as we have seen in previous studies of condensed phase reactions of Cl atoms with several other alkanes.[11,18]

3.3.2 Reaction of Cl atoms with 2,3-dimethyl-2-butene (DMBE)

As mentioned above, Orr-Ewing and coworkers have recently reported the reaction dynamics of Cl atom reaction with DMBE in CCl_4 and $CDCl_3$.[12] One of the most intriguing results of the Cl + DMBE reaction dynamics is the detection of vibrationally excited HCl products in the condensed phase; this observation was a first. This reaction is exoergic enough to populate up to the v=2 excited vibrational state of HCl as predicted by ΔE, and the experiment shows production of HCl (v=1). This indicates that despite any perturbations from the solvent, vibrationally excited HCl forms, and even though collisions occur with the solvent molecules on a hundred femtosecond timescale, the vibrational motion of the nascent HCl is not completely dampened by the solvent. In fact, DMBE itself provides an efficient pathway for vibrational relaxation of HCl (v=1) *via* vibration-to-vibration (V-V) energy transfer, which changes the relaxation time of HCl (v=1) from 4.7 ns to 50 ps (in 1 M DMBE solution in CCl_4).[12]

Figure 4 displays the contour plots of our transient absorption measurements and the corresponding spectra at certain time delays. An additional band at 2710 cm^{-1} appears in CCl_4 along with the fundamental band of HCl at 2828 cm^{-1}. In $CDCl_3$, these two bands shift to lower energy by 5 and 10 cm^{-1}, locating at 2705 and 2818 cm^{-1}. (As in the DMB reaction, an

Figure 4. Contour plots of transient absorption (top) and the corresponding spectra at selected time delays (bottom) for the reaction of Cl with 0.5 M DMBE in (a) CCl_4 and (b) $CDCl_3$.

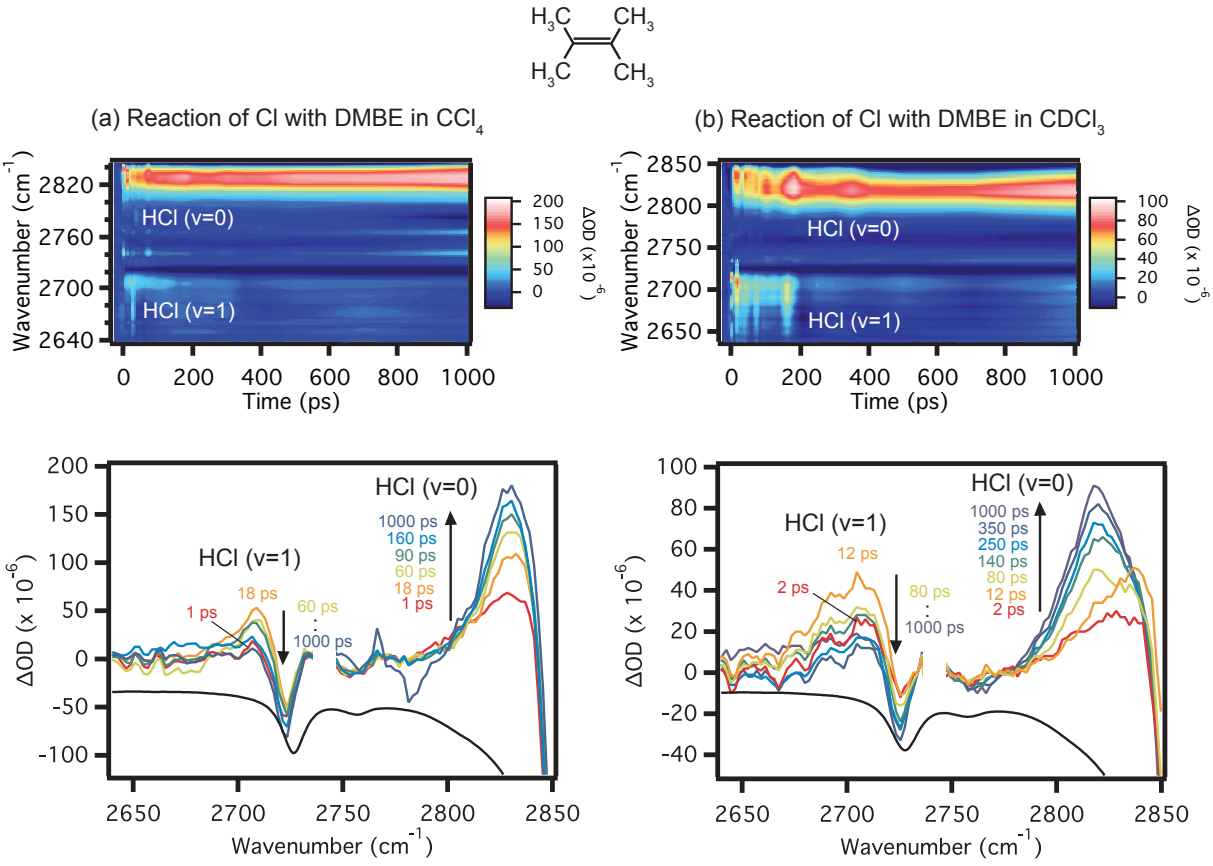
H3C CH3
H3C CH3
(a) Reaction of Cl with DMBE in CCl4
(b) Reaction of Cl with DMBE in CDCl3
Wavenumber (cm-1)
HCl (v=0)
HCl (v=1)
Time (ps)
ΔOD (x 10-6)
ΔOD (x 10-6)
1 ps
18 ps
60 ps
1000 ps
1000 ps
160 ps
90 ps
60 ps
18 ps
1 ps
2 ps
12 ps
80 ps
1000 ps
1000 ps
350 ps
250 ps
140 ps
80 ps
12 ps
2 ps
Wavenumber (cm-1)

interference from the changing absorption of DMBE results in the negative-signals at 2725 cm^{-1} and above 2850 cm^{-1}.) Orr-Ewing and coworkers assigned the new feature appearing at 2710 cm^{-1} in CCl_4 (and 2705 cm^{-1} in $CDCl_3$) to the HCl (v=2 ← v=1) hot band. This hot band grows in on a similar time scale to the rise of the fundamental band until ~20 ps and then decays at the rate of the V-V energy transfer with DMBE. The close proximity of the C-H stretching band of DMBE (starting from 2820 cm^{-1}) and the fundamental band of HCl (2828 cm^{-1}) implies that near-resonant V-V energy transfer can occur from HCl (v=1 → v=0) to DMBE (v_{C-H}=0 → v_{C-H}=1).

Figure 5 illustrates that our transient absorption measurements (taken at three different concentrations) show the same dynamics as Orr-Ewing and coworkers reported. Again, we adopted their kinetic model to fit our integrated intensity data. Since HCl (v=1) is a product of the DMBE +Cl reaction, they incorporate this state and the accompanying vibrational relaxation into the kinetic model, as shown below.

In-cage reaction and relaxation:

$$Cl_c + RH \xrightarrow{k_{0c}} HCl\,(v=0)_c + R \qquad (2a)$$

$$Cl_c + RH \xrightarrow{k_{1c}} HCl\,(v=1)_c + R \qquad (2b)$$

$$HCl\,(v=1)_c \xrightarrow{k_{rc}} HCl\,(v=0)_c \qquad (2c)$$

Diffusion:

$$Cl_c \xrightarrow{k_d} Cl_b \qquad (2d)$$

$$HCl\,(v=0)_c \xrightarrow{k_d} HCl\,(v=0)_b \qquad (2e)$$

$$HCl\,(v=1)_c \xrightarrow{k_d} HCl\,(v=1)_b \qquad (2f)$$

In-bulk reaction and relaxation:

$$Cl_b + RH \xrightarrow{k_{0b}} HCl\,(v=0)_b + R \qquad (2g)$$

Figure 5. Time dependent integrated intensities of the HCl (v=0, black and grey) and the HCl (v=1, red and blue) bands for reaction of Cl with varying concentrations of DMBE in (a) CCl_4 and (b) $CDCl_3$. The DMBE concentrations are 0.2 M (open triangles), 0.5 M (circles), and 0.75 M (closed triangles). The solid lines are the fit from the kinetic model.

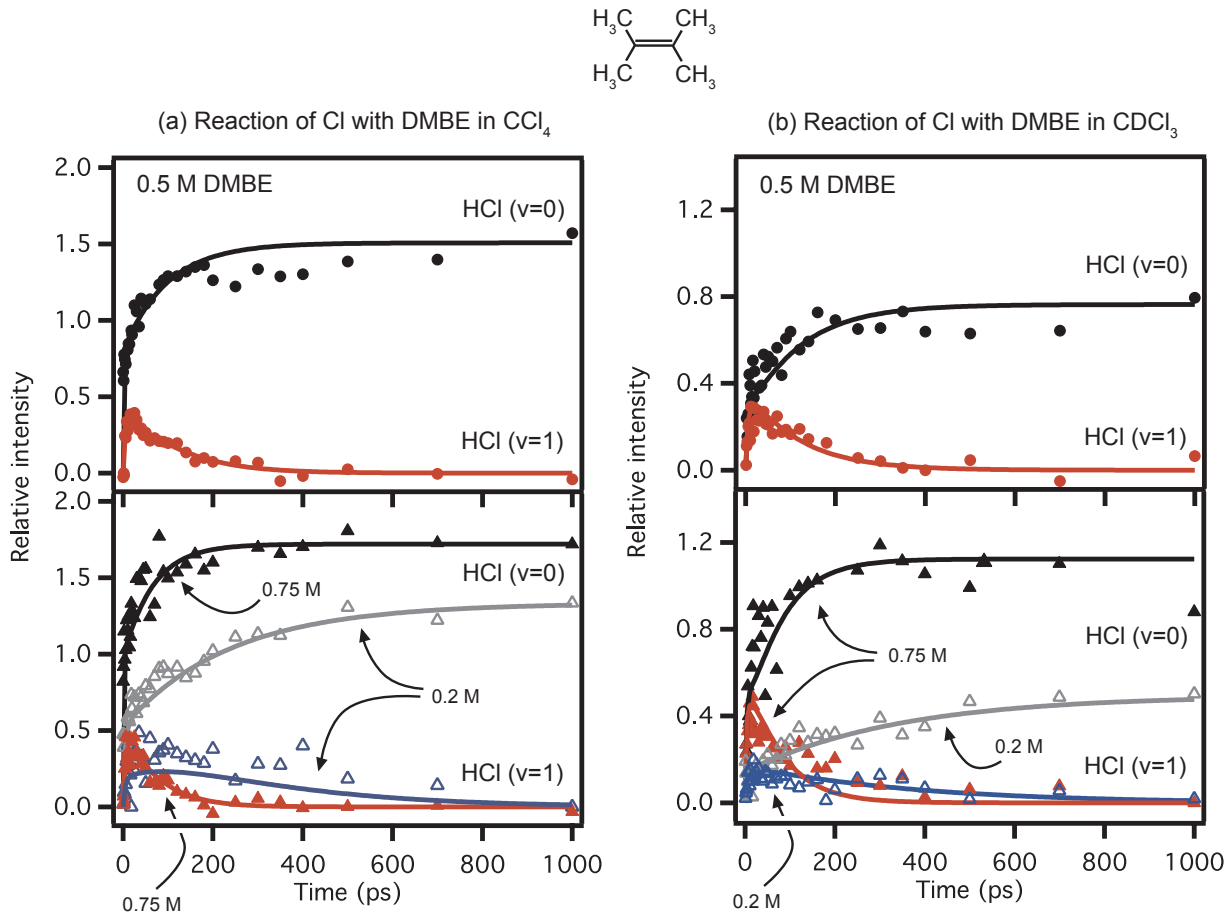
H3C CH3
H3C CH3
(a) Reaction of Cl with DMBE in CCl4
(b) Reaction of Cl with DMBE in CDCl3
0.5 M DMBE
HCl (v=0)
HCl (v=1)
0.75 M
0.2 M
Relative intensity
Time (ps)
0.75 M
0.2 M

$$Cl_b + RH \xrightarrow{k_{1b}} HCl\ (v=1)_b + R \qquad (2h)$$

$$HCl\ (v=1)_b \xrightarrow{k_{rb}} HCl\ (v=0)_b \qquad (2i)$$

The notation is as before, and with the subscript 1 denoting a reaction producing HCl (v=1) and the subscript r denoting the vibrational relaxation of HCl (v=1). In our global fitting, we fix k_{rc} to 0 for the same reason that the former investigators addressed; its value is always negligible during many trials of fitting when we free it as a floating parameter. This means that the nascent HCl (v=1) products do not encounter a significant number of DMBE molecules before diffusing out of the initial solvation cage and, thus, no vibrational energy transfer occurs within the solvent cage. Additionally, we fix the vibrational relaxation rate in the bulk solvent, k_{rb}, to 2×10^{10} $s^{-1}M^{-1}$ as in the former study where the authors estimated it from their IR pump-probe experiments. We also use a scaling factor of 2 to compensate for the difference in the transition moments of the hot band (v=2 ← v=1) and the fundamental band of HCl and correct the population of HCl (v=1) based on its signal intensity. Since the HCl (v=0) signal that we observe comes from population difference between HCl (v=1) and HCl (v=0), we subtract the corrected population of HCl (v=1) from the population of HCl (v=0) in the kinetic model to fit the experimental HCl (v=0) signal. Orr-Ewing and coworkers used this same strategy. Our fits obtain a total bimolecular reaction rate in the bulk solvent, K_{bi}, of 3.6 (± 0.3) × 10^{10} $M^{-1}s^{-1}$ in CCl_4 and 1.7 (± 0.6) × 10^{10} $M^{-1}s^{-1}$ in $CDCl_3$ (Table 1). These values match those previously reported. We also define a branching ratio of HCl (v=1) as:

$$\Gamma(v=1) = \frac{HCl(v=1)}{HCl(v=1)+HCl(v=0)} = \frac{K_{1c}+K_{1b}}{K_{1c}+K_{1b}+K_{0c}+K_{0b}} \qquad (3)$$

This ratio identifies what fraction of the total HCl molecules produced are vibrationally excited (in v=1), revealing the energy disposal of the reaction. The branching ratios, Γ, derived from the above equation in our experiments are 0.14 ± 0.01 in CCl_4 and 0.23 ± 0.05 in $CDCl_3$, which are again consistent with those reported in the former study. The branching ratio for this reaction has not been determined in the gas phase. However, these values are significantly smaller than the branching ratio of a illustrative gas phase reaction, such as the Cl + propene reaction (Γ (v=1) = 0.48 ± 0.06),[20] implying that while the solvent does not completely suppress the production of vibrational products, it does perturb the reaction dynamics and, in this comparison, the fraction of vibrationally excited products diminishes.

3.3.3 Reaction of Cl atoms with 2,5-dimethyl-2,4-hexadiene (DMHD)

We wish to increase further our understanding of the reaction dynamics of Cl + alkene reactions. To this end, we study the reaction of Cl with DMHD in the condensed phase. DMHD is another alkene with which we can classify these hydrogen abstraction reactions. Moreover, the presence of two distinct types of hydrogen atoms makes it a slightly more complex reactant. To this end, the DMHD experiments that follow enrich the available Cl + alkene studies and promote insight into bimolecular reaction dynamics in the condensed phase.

As expected from the calculated overall reaction energy, the IR transient absorption measurements for the reaction of Cl + DMHD in CCl_4 and $CDCl_3$ show evidence of both ground state and vibrationally excited HCl (see Figure 6). In CCl_4 (and $CDCl_3$), we assign the band at 2717 cm^{-1} (2709 cm^{-1}) as the v=2 ← v=1 hot band and the band at 2830 cm^{-1} (2816 cm^{-1}) as the fundamental stretch of HCl. As with the DMBE solutions, the transient absorption spectra show negative-going signals near the high-energy side of each band due to the changing absorption of

Figure 6. Contour plots of transient absorption (top) and the corresponding spectra at selected time delays (bottom) for the reaction of Cl with 0.2 M DMHD in (a) CCl_4 and (b) $CDCl_3$.

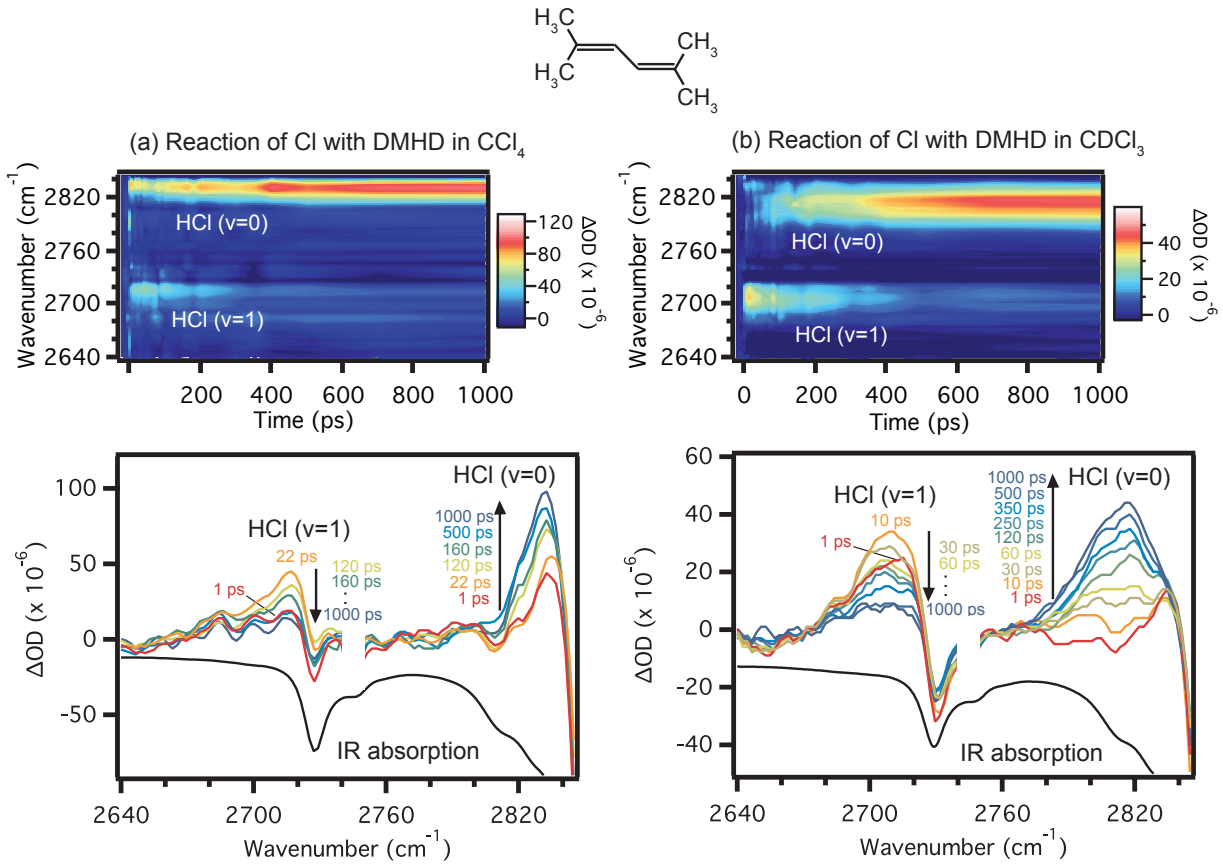
(a) Reaction of Cl with DMHD in CCl4
(b) Reaction of Cl with DMHD in CDCl3
Wavenumber (cm-1)
Time (ps)
HCl (v=0)
HCl (v=1)
ΔOD (x 10-6)
ΔOD (x 10-6)
Wavenumber (cm-1)
1 ps
22 ps
120 ps
160 ps
1000 ps
1000 ps
500 ps
160 ps
120 ps
22 ps
1 ps
10 ps
30 ps
60 ps
1000 ps
1000 ps
500 ps
350 ps
250 ps
120 ps
60 ps
30 ps
10 ps
1 ps
IR absorption

the DMHD. The hot band at 2717 cm^{-1} (2709 cm^{-1}) grows in during the first 20 ps and then decays away, while the fundamental band at 2830 cm^{-1} (2816 cm^{-1}) simply grows monotonically. The time dependence of these spectral signatures is analogous to those of the hot band and fundamental band of HCl observed in the DMBE reactions with Cl, further supporting their assignment as HCl product signals of the v=1 and v=0 vibrational states.

Figures 7 and 8 show the time dependent integrated intensities for the v=0 and v=1 HCl signals. Also note that despite a careful search below ~2600 cm^{-1}, we did not observe any signal that could be assigned to a transition from the v=2 state of HCl. The fundamental band grows in monotonically, as in the Cl + DMBE reactions, in both CCl_4 and $CDCl_3$. In both solvents, the hot band decays on the same time scale as in the Cl + DMBE reactions; recall that the V-V energy transfer rate governs this decay. Also, the C-H stretching band of DMHD resides near the fundamental band of HCl. Thus, it is likely that a near-resonant V-V energy transfer also occurs between the HCl (v=1) product of this reaction and the DMHD reactant.

In the reaction of Cl and DMHD, the time dependence of both the ground and excited state HCl signals looks qualitatively similar to the DMBE reactions: the monotonic growth of the HCl (v=0) band and the rise-and-decay of the HCl (v=1) band. Their dynamics depend on the sample concentrations and solvents in a manner that is similar to the Cl + DMBE reaction; however, the maximum intensities of the HCl (v=1) signal relative to the HCl (v=0) signal from 10 to 20 ps are much higher than in the DMBE reactions. This indicates that the initial branching ratio into the v=1 and v=0 states of HCl is different, with the reaction of Cl atoms with DMHD producing more vibrationally excited HCl than the reaction of Cl atoms with DMBE.

For a quantitative analysis, we fit these data using the same kinetic model implemented

Figure 7. Time dependent integrated intensities of the HCl (v=0, black) and the HCl (v=1, red) bands for the reaction of Cl with 0.2 M DMHD in (a) CCl_4 and (b) $CDCl_3$. In both (a) and (b), the lower plot shows an enlarged view of early time. The solid lines are the fit from the kinetic model.

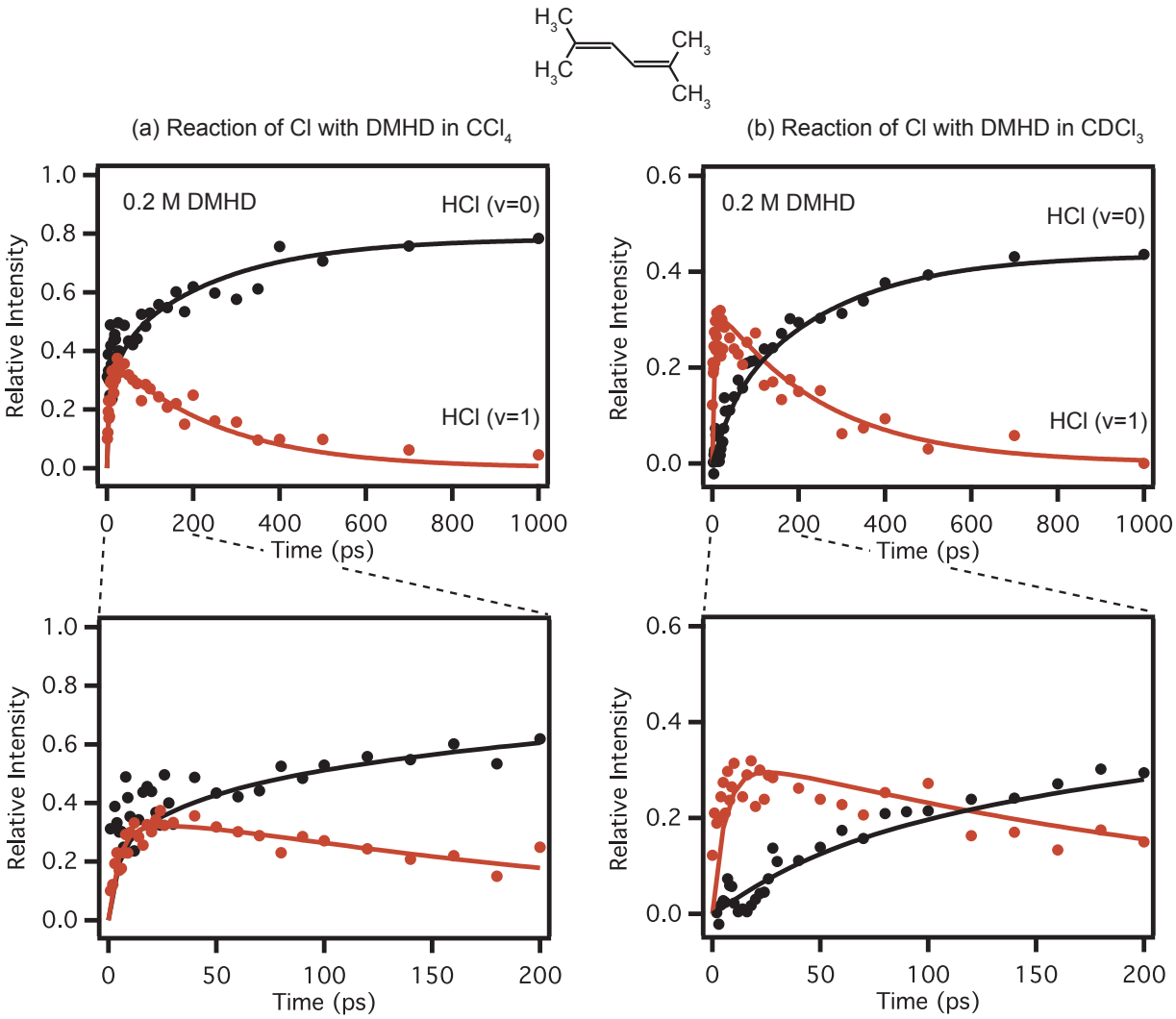
H3C
CH3
H3C
CH3
(a) Reaction of Cl with DMHD in CCl4
(b) Reaction of Cl with DMHD in CDCl3
0.2 M DMHD
HCl (v=0)
HCl (v=1)
Relative Intensity
Time (ps)

Figure 8. Time dependent integrated intensities of the HCl (v=0, black and grey) and the HCl (v=1, red and blue) bands for the reaction of Cl with varying concentrations of DMHD in (a) CCl_4 and (b) $CDCl_3$. The DMHD concentrations are 0.1 M (open triangles) and 0.35M (circles). In both (a) and (b), the lower plot shows an enlarged view of early time. The solid lines are the fit from the kinetic model.

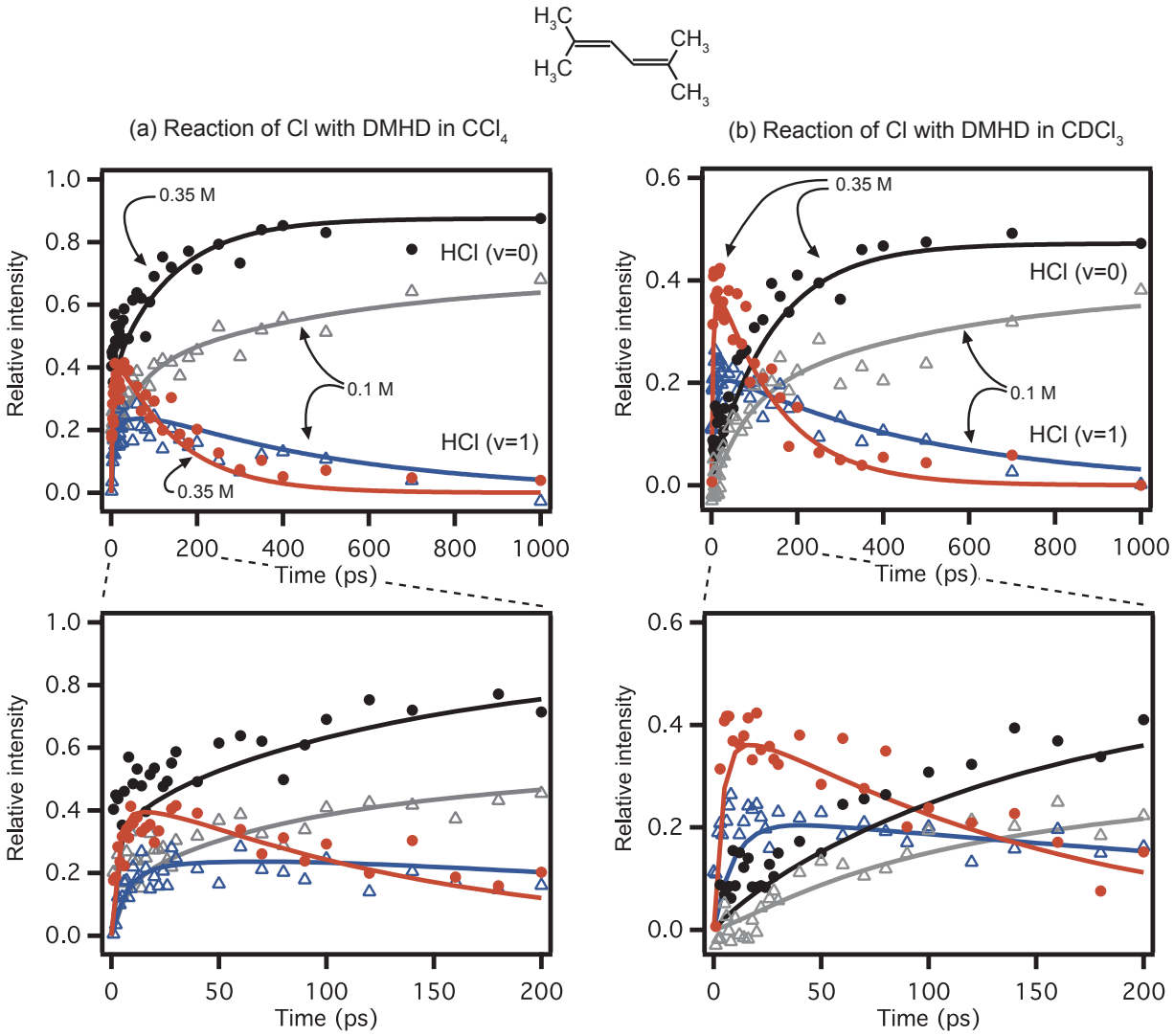
H3C
CH3
H3C
CH3
(a) Reaction of Cl with DMHD in CCl4
(b) Reaction of Cl with DMHD in CDCl3
Relative intensity
Time (ps)
0.35 M
0.1 M
HCl (v=0)
HCl (v=1)

for the DMBE reaction dynamics (Equation 2). In the global fitting of the DMHD data, we again found that allowing k_{rc} to float results in a negligibly small value so we fixed k_{rc} at 0, thus assuming no vibrational relaxation (V-V energy transfer) in the initial solvation cage. We also constrained the diffusion rate coefficient, k_d, so that it does not largely deviate from the reported values in the DMBE reactions. Although we did not carry out IR pump-probe experiments of an HCl solution in the presence of DMHD to estimate the vibrational relaxation (or V-V energy transfer) rate of HCl (v=1), we presumed that there is no large difference in the relaxation rates of HCl (v=1) between DMBE and DMHD. Therefore, we use the vibrational relaxation rate determined by Orr-Ewing and coworkers for HCl (v=1) in a DMBE solution as the k_{rb} for the reactions of Cl + DMHD. For validation, we fit the decay of the HCl (v=1) signal from its maximum at ~ 20 ps using a single-exponential function, and find that the fit yields $\tau \approx 250$ ps for the 0.2 M DMHD solution in CCl_4. This decay rate matches the V-V energy transfer rate of HCl (v=1) in the DMBE reactions, supporting our assumption.

The kinetic schemes, using the above-mentioned fixed parameters, give a nice fit to the DMHD data for all three concentrations, as displayed by the solid lines in Figures 6 and 7; Table 1 summarizes the resulting rate coefficients. The total bimolecular reaction rate constants, K_{bi}, reveal that the abstraction of a hydrogen atom from DMHD by Cl is very fast, approaching the diffusion limit; K_{bi} = 17.5 (± 1.6) × 10^{10} $M^{-1}s^{-1}$ in CCl_4 and 6.7 (± 1.6) × 10^{10} $M^{-1}s^{-1}$ in $CDCl_3$. These rates are 4- or 5-fold larger than those of Cl + DMBE reactions. The branching ratios of HCl (v=1), Γ, derived from Equation 3 are 0.23 ± 0.06 in CCl_4 and 0.40 ± 0.12 in $CDCl_3$, showing a 2-fold increase over those of Cl + DMBE. Furthermore, there is clear difference between reaction in CCl_4 and $CDCl_3$; the Cl + DMHD reaction in $CDCl_3$ is slower and produces more HCl in the excited vibrational state (v=1).

To complement the IR transient absorption data, we measure broadband electronic transient absorption for the Cl + DMHD reaction in CCl_4 to confirm that the fast reaction rates obtained by detecting product formation (IR transient absorption) match those obtained by detecting the reactant loss. As mentioned earlier, we follow the dynamics of the Cl atom after photolyzing CCl_4 with 267 nm light by monitoring the absorption band of the Cl-solvent complex at 330 nm. Without reaction partners in solution, like in neat CCl_4, Cl atoms (or Cl-solvent complexes) recombine to the parent CCl_4 or isomerize to iso-CCl_3–Cl molecules that result in a broad absorption band having a maximum at 500 nm. However, for the DMHD solution in CCl_4 another absorption band emerges at 300 nm. Figure 9 shows that this feature is intense and results in the Cl-solvent complex band appearing more like a shoulder to this feature. This unexpected band appears immediately after interaction with the photolysis light and decays, by about half, on a time scale that is similar to its "shoulder". However, we find that the actual band is largely dependent on the DMHD concentration, while its "shoulder" is not. Increasing the concentration of DMHD drastically increases the band at 300 nm; the intensity the "shoulder" near 340 nm stays roughly the same. Further increasing the concentration begins to obscure the unexpected band because of interference from the DMHD absorption, which begins to dominate and shows a tail up to 290 nm (Figure 10(a)). From looking at the concentration dependence, we believe that the band at 300 nm originates from the solute, DMHD, while the "shoulder" at 340 nm is unlikely to relate to the solute and is instead an independent band that is due to the Cl-CCl_4 complex.

DMHD can form a radical cation in acetonitrile by absorbing 267 nm light. According to a laser flash photolysis study of DMHD in acetonitrile, the laser excitation at 267 nm ejects one electron from neutral DMHD generating a radical cation, $DMHD^{\bullet+}$, and the transient absorption

Figure 9. Electronic transient absorption measurements showing in (a) contour plots of 2 mM DMHD in CCl_4, (b) the corresponding spectra at selected time delays for the 2 mM solution, and (c) transient spectra of 0.5, 1, and 2 mM DMHD in CCl_4 at a 2 ps time delay.

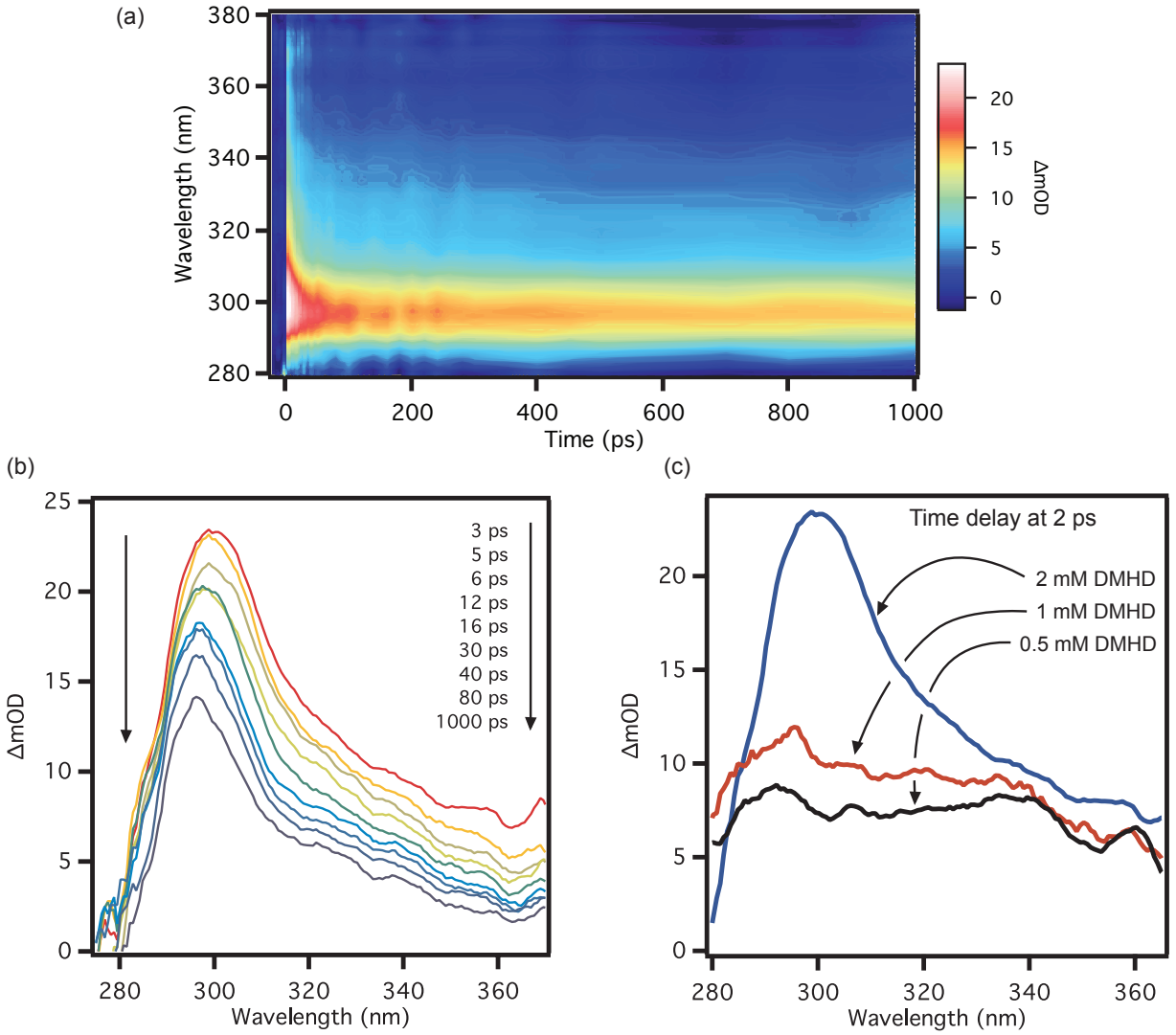
(a)
Wavelength (nm)
Time (ps)
ΔmOD
(b)
ΔmOD
Wavelength (nm)
3 ps
5 ps
6 ps
12 ps
16 ps
30 ps
40 ps
80 ps
1000 ps
(c)
Time delay at 2 ps
2 mM DMHD
1 mM DMHD
0.5 mM DMHD
ΔmOD
Wavelength (nm)

Figure 10. UV/VIS absorption spectra of DMHD in CCl_4: (a) before (UVoff) and after (UV on) irradiation with 267 nm light for 15 minutes, (b) the difference spectrum (UV on - UV off), and (c) its enlarged view.

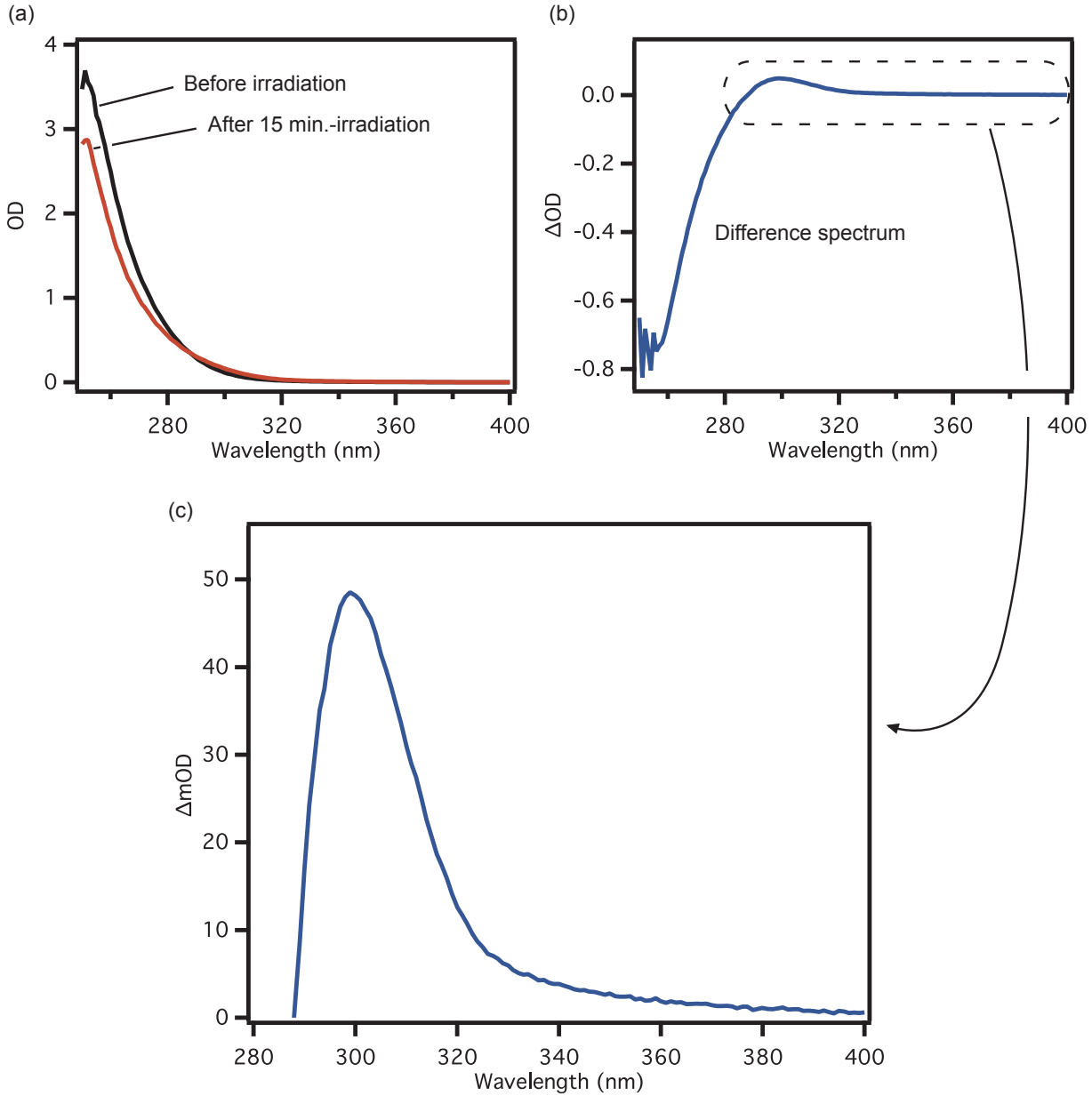
(a)
Before irradiation
After 15 min.-irradiation
OD
Wavelength (nm)
(b)
Difference spectrum
ΔOD
Wavelength (nm)
(c)
ΔmOD
Wavelength (nm)

spectrum shows a peak maximum at 365 nm along with a broad, weak band that spans from 400 to 580 nm.[21] The lifetime of $DMHD^{\bullet+}$ was estimated to be ~5 μs in the same study. However, our electronic transient absorption measurements show no absorption feature near 365 nm, presumably due to the different solvent. We consider it unlikely that the band at 300 nm is due to the $DMHD^{\bullet+}$ absorption because of the 65 nm shift is considerably large for a solvent effect. Moreover, we observe the 300 nm band in a steady-state UV/VIS absorption measurement (see Figure 10). We irradiate a diluted DMHD solution in CCl_4 with 267 nm laser light for 15 minutes and measure the UV/VIS absorption spectrum. The difference spectrum between the initial (non-irradiated) and irradiated spectra shows a strong depletion of DMHD at 250 nm and small absorptive increase at 300 nm. Note that the enlarged difference spectrum displayed in Figure 10(c) is *nearly* the same as the transient absorption spectrum of DMHD in CCl_4 (see Figure 9). We emphasize *nearly* because the difference is valuable; the difference is the "shoulder" to the lower energy side, the Cl-solvent complex signal. We think that the band at 300 nm observed in both the time-resolved and steady-state measurements of the DMHD solution comes from the same species, and that this species is unlikely to be the radical cation ($\tau \sim 5$ μs). We also rule out the possibility of triplet excited state absorption of DMHD. A pulse radiolysis study finds a $T_1 \rightarrow T_n$ absorption feature for DMHD at 290 ~ 320 nm, but the lifetime of T_1 is ~ 80 ns.[22] Rather, we argue that the band at 300 nm is due to the formation of unknown photoproduct. Indeed, we observe deposition onto the sample cell windows after long irradiation of 267 nm light on the sample or even after the ultrafast transient absorption measurements for concentrations over 0.35 M. Excitation of DMHD at 267 nm may possibly drive some of the excited population to another stable minimum. A conical intersection may be involved, and photoinduced reaction processes

involving conical intersections are known to occur on a very fast time scale in conjugated molecules. For instance, the ultrafast photoisomerization of rhodopsin and the internal conversion of ethylene *via* conical intersection occur on ~200 fs time scale.[23,24] Such processes could explain the instantaneous appearance of the unexpected band (at 300 nm) in our transient absorption. As a final note, we do not consider the electronically excited DMHD as a contaminant in the Cl + DMHD reaction because it will relax down to the ground state through conical intersection on a few hundred femtosecond time scale before it has a chance to react with the Cl atoms.

Given that the observed transient absorption spectrum consists of two bands havingdifferent origins, we disentangle their dynamics by fitting the experimental spectrum with two Gaussian curves in KOALA (see Figure 11). We first fit the Cl-CCl_4 complex band in the transient absorption spectrum of neat CCl_4 using one Gaussian to obtain a position and width for the curve. We then use these values to fix the position and width of the Cl-CCl_4 complex band when fitting the DMHD solution. We fit the whole spectrum by varying all of the fit parameters for the Gaussian curve of the unexpected band (Gaussian1 in Figure 11(a)) and only the height for the Gaussian curve of the Cl-CCl_4 complex band (Gaussian2 in Figure 11(a)). The total fit and the experimental spectra agree nicely for each time delay. The integrated area for each of these two Gaussian curves shows different behaviors (see Figure 11(b)). The Cl-solvent complex band (Gaussian2) shows decay as a predominant feature, while the integrated area of Gaussian1 shows little change in intensity. Furthermore, the decay of Gaussian1 is even less pronounced at lower concentrations (< 2 mM). (We only show the 2 mM DMHD data due to the inferior quality of the lower concentration data.) Fitting the decay of Gaussian1 from the 2 mM DMHD solution using a single exponential function, we obtain a time constant of ~ 47 ps. We suspect that this

Figure 11. Analysis of the broadband electronic transient absorption spectra: (a) a representative fit of the transient absorption spectrum of 2 mM DMHD in CCl_4 at a 2 ps time delay using two Gaussian curves and (b) the time dependent integrated area for these Gaussian curves in neat CCl_4 (open circles) and 0.5 mM (closed circles, black), 1 mM (red), and 2 mM (blue and green) DMHD solutions. The solid lines are the fit using the Smoluchowski model (b, top) and a single exponential function (b, bottom). The dashed line in (b, top) is the Smoluchowski fit for neat CCl_4.

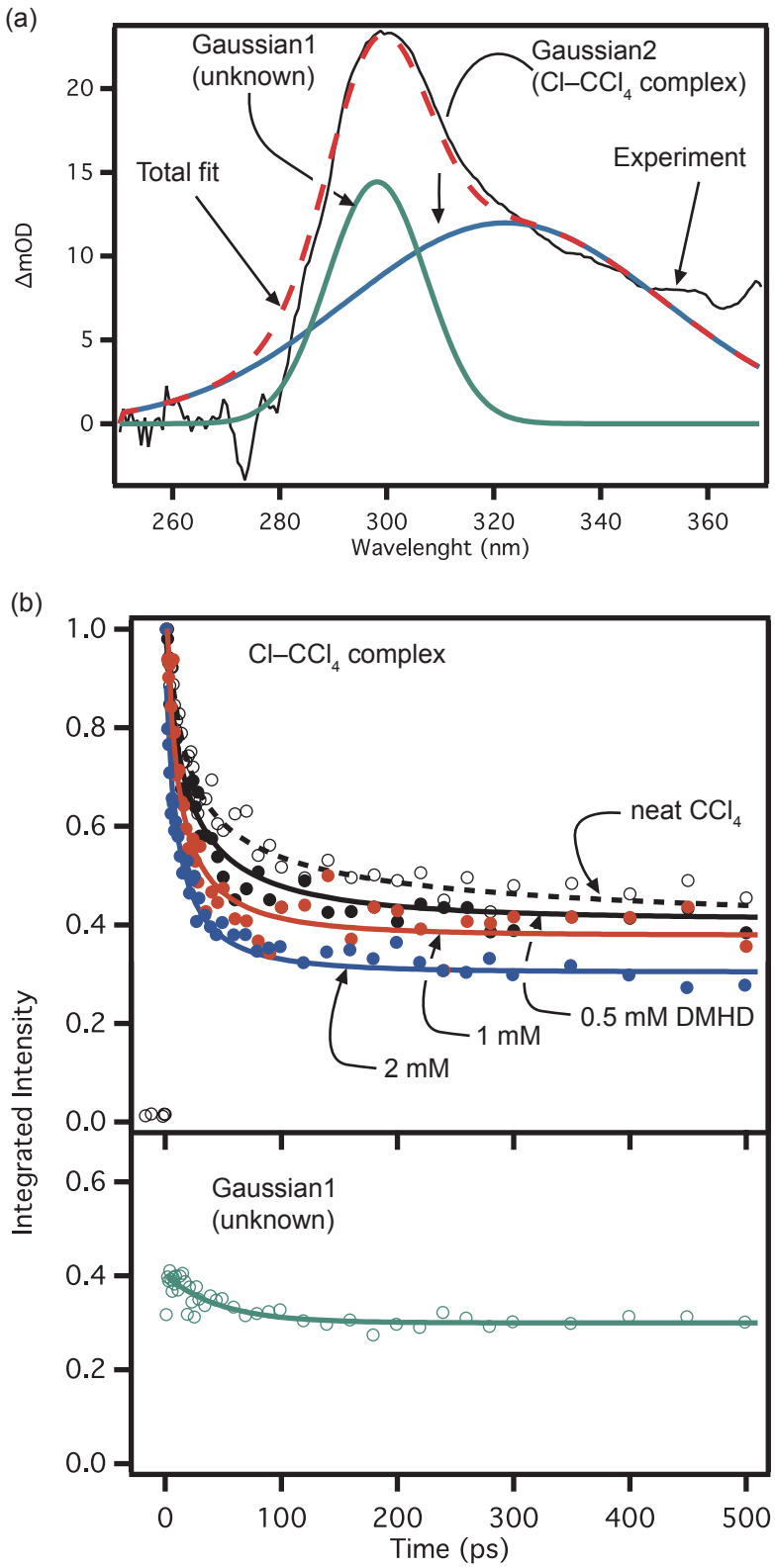
(a)
Gaussian1
(unknown)
Gaussian2
(Cl–CCl4 complex)
Total fit
Experiment
ΔmOD
20
15
10
5
0
260
280
300
320
340
360
Wavelenght (nm)
(b)
Cl–CCl4 complex
neat CCl4
0.5 mM DMHD
1 mM
2 mM
Integrated Intensity
1.0
0.8
0.6
0.4
0.2
0.0
Gaussian1
(unknown)
0
100
200
300
400
500
Time (ps)

species is actually stable on the time scale of this study, but that an imperfection in the deconvolution of the two absorption bands leads to the perceived small decay. On the other hand, the rate of decay of the Cl-CCl_4 complex band gradually increases as the concentration increases, indicating a bimolecular reaction.

We use the Smoluchowski model to fit the time dependent dynamics of the Cl-CCl_4 complex band and obtain the bimolecular reaction rate coefficient from the disappearance of Cl-CCl_4 complex (a reactant) as in previous work by the Crim[11,18,25-27] and Orr-Ewing[17] groups. The Smoluchowski model is based on the theory of diffusion and, thus, is well suited for describing geminate recombination of radical photoproducts and diffusion-controlled reactions in the condensed phase.[28-30] In the electronic transient absorption measurements, we observe both diffusive geminate recombination and reaction with solute by monitoring the dynamics of Cl-CCl_4 complexes. Each of these processes gives rise to the signal, showing a non-exponential and exponential decay, respectively. The Smoluchowski model takes these into accounts for data analysis. We describe the time dependent survival probability (or concentration) of the Cl-solvent complex in neat CCl_4 as:

$$\mathrm{P}(t) = [\mathrm{Cl}]_0 \left\{1 - Aefc\left(\frac{B}{\sqrt{t}}\right)\right\} \exp(-k_1 t) \tag{4}$$

where $[Cl]_0$ is an initial concentration and the exponential term represents a reactive loss of the complex. The term in the parenthetical term with the complementary error function, *efc*, arises from diffusive geminate recombination of the complex, where $A = R_{rec}/r_0$ and $B = (r_0 - R_{rec})/(4D_{rec})^{1/2}$. The overall picture explained by Equation 4 is that once the Cl-CCl_4 and CCl_3 fragments equilibrate at a relative distance, r_0, after dissociation, they move with a relative diffusion constant, D_{rec}, and recombine when they reach an effective radius, R_{rec}. In neat CCl_4, the reactive loss of the complex, namely the reaction of Cl-CCl_4 with CCl_4, is negligible ($k_1 \approx 0$).

The fit of the Cl-CCl_4 band in our transient absorption measurements of neat CCl_4 yields A = 0.642 and B = 0.080 $ns^{1/2}$ (dashed line in Figure 10(b, top)). These values are consistent with our previous study.[11]

In the DMHD solution, the Cl-CCl_4 complexes have an additional loss channel beyond recombination with a CCl_3 radical; they can also react with the solute. We express the time dependent survival probability of the complex for this reactive process as:

$$\mathrm{P'}(t) = \exp\left\{-4\pi R_{\mathrm{rxn}} D_{\mathrm{rxn}} C_{\mathrm{solute}} \left(1 + \frac{2R_{\mathrm{rxn}}}{\sqrt{\pi D_{\mathrm{rxn}} t}}\right) t\right\} \tag{5}$$

where R_{rxn} is the effective radius for the reaction, D_{rxn} is the relative diffusion constant of the reactants, and C_{solute} is the concentration of the solute. Therefore, combining Equations 4 and 5 gives the total survival probability of the Cl-CCl_4 complex in the DMHD solution. Thus, we fit the time dependent integrated area of Gaussian2 with

$$\mathrm{S}(t) = \mathrm{P}(t)\mathrm{P}'(t) + \mathrm{S}_{\infty} \tag{6}$$

where S_∞ is a baseline offset that persists at long time delay, which is mainly due to absorption of the unknown photoproduct not captured by Gaussian1. In the fitting procedure, we fixed A and B to the values that we obtained for neat CCl_4, k_1 to 0, and C_{solute} to the sample concentration. The relative diffusion constant, D_{rxn}, is the sum of the diffusion constants of the Cl-CCl_4 complex and the solute, DMHD; we calculate each diffusion constant using the Stokes–Einstein equation

$$D = \frac{k_{\mathrm{B}}\mathrm{T}}{6\pi\eta a} \tag{7}$$

where k_B is the Boltzmann constant, T is the temperature, η is the solvent viscosity, and a is the radius of the diffusing particle. To estimate the radius of the Cl-CCl_4 complex and the DMHD molecule, we optimized each geometry using density functional theory and a 6-311G++(d,p) basis set to determine the distance between the center of mass and the furthest atom.

Consequently, we fix D_{rxn} to 1.38 nm^2ns^{-1}. We note that our calculated D_{rxn} (Cl-CCl_4:DMHD) is close to the D_{rxn} (Cl-CCl_4:1,5-hexadiene) calculated by Orr-Ewing and coworkers, 1.27 nm^2ns^{-1}.[17] Using the R_{rxn} that we obtain from the fit, we derive the bimolecular reaction rate coefficient using the relation

$$k_{bi} = 4\pi R_{rxn} D_{rxn} \quad (8)$$

Finally, using the separate fits of the Cl-CCl_4 complex band (Gaussian2) for the 0.5, 1, and 2 mM DMHD solutions, results in averaged bimolecular reaction rate constant, k_{bi} = 23.3 (± 5.7) × 10^{10} $M^{-1}s^{-1}$ (solid lines in Figure 10(b, top)). This value estimated by monitoring the disappearance of reactants also indicates that the bimolecular reaction rate of Cl + DMHD is very fast and close to the diffusion limit. More importantly, both rate constants obtained from IR and electronic transient absorption measurements for this reaction in CCl_4 are in good agreement with each other (within an error range). This means that disappearing Cl atoms (or complexes) are directly associated with the formation of HCl in the v=0 and v=1 states.

3.3.4 Quantum calculations for the reaction profiles of Cl + DMB, DMBE, and DMHD reactions

To elucidate the detailed reaction energetics, including the transition state (TS), we perform *ab initio* electronic structure calculations at the UB3LYP level of theory with a 6-311G++(d,p) basis set. We also apply an IEFPCM of CCl_4, $CHCl_3$, and CH_2Cl_2 to the calculations for evaluating the solvent effects on each reaction.

For the Cl + DMB reaction, we calculate the energy profiles for both hydrogen abstraction channels, abstracting hydrogen from the primary and tertiary carbons (Figure 12). Our gas phase calculations for both channels are in agreement with the results of Wang *et. al.*,

Figure 12. Calculated energy profiles of Cl + DMB reactions in the gas phase (black), CCl_4 (red), and $CHCl_3$ (blue) and the representative calculated structures of the complexes and TS taken from the gas phase calculations. DMB(p)$^{\bullet}$ and DMB(t)$^{\bullet}$ are the alkyl radicals that form after a hydrogen is abstracted from primary and tertiary carbons, respectively. The energy levels do not include the ZPE correction.

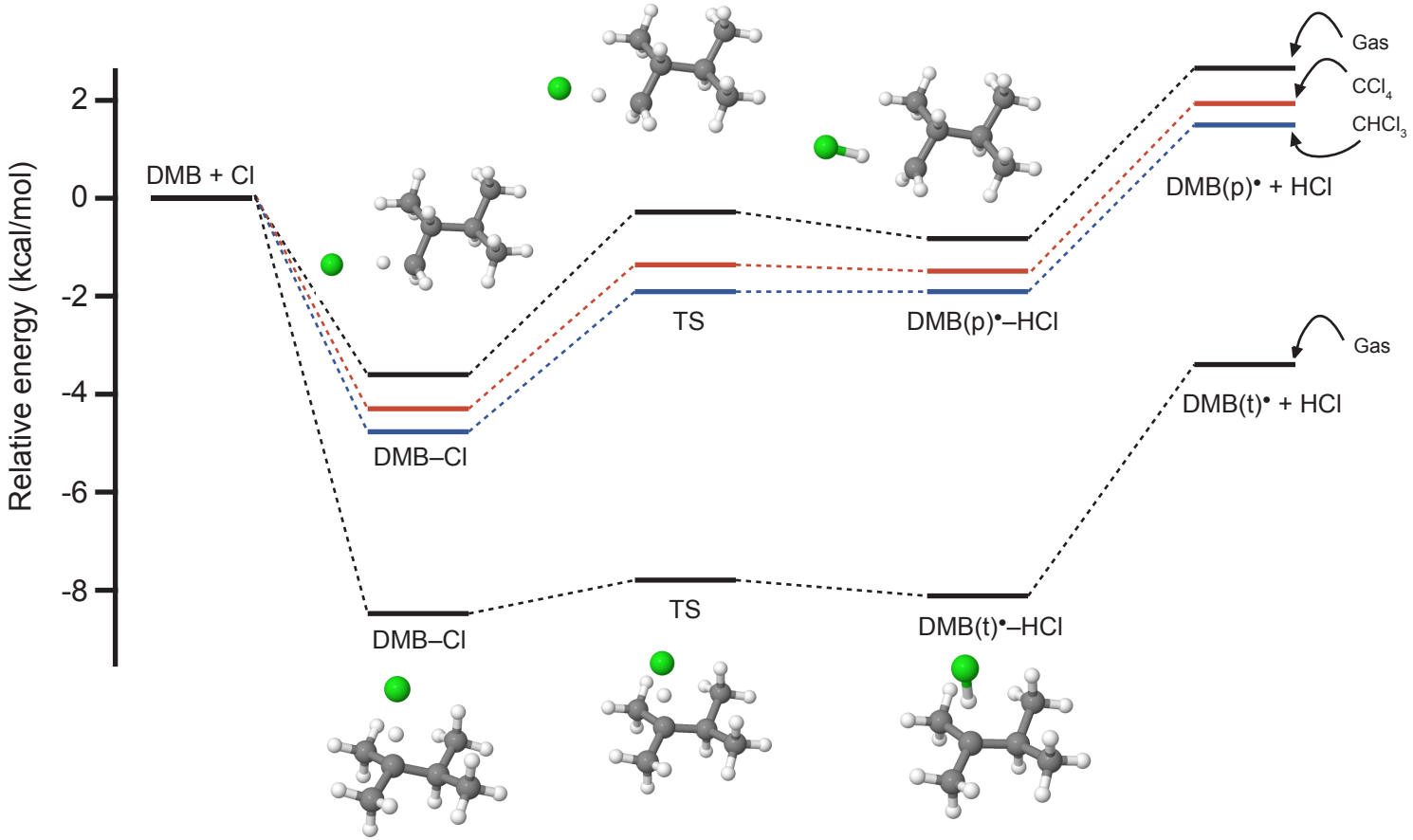
Relative energy (kcal/mol)
2
0
-2
-4
-6
-8
DMB + Cl
DMB–Cl
TS
DMB(p)•–HCl
DMB(p)• + HCl
Gas
CCl4
CHCl3
DMB–Cl
TS
DMB(t)•–HCl
DMB(t)• + HCl
Gas

who calculated the energy profiles of the Cl + DMB reaction using the same level of theory and basis set as in this study.[31] We find the TS structures and the energy minima for the van der Waals complexes of reactants (DMB–•Cl) and products (DMB•–HCl) that form in the entrance and exit channels, respectively (Figure 12). The TS structures for both reaction channels show a collinear Cl–H–C geometry, similar to other Cl + alkane reactions.[32] Similarly, the reactant and product complexes also have a collinear configuration, implying that they share the same TS. We use IRC calculations to confirm that these local minima share the one TS obtained. We display each energy level without a zero-point energy (ZPE) correction. The TS lies slightly below the energy levels of the reactant- and product-complexes when the ZPE correction is included, and the harmonic approximation often overestimates the ZPE at local minima causing of the relative energy of the TS to be incorrect.[31,33] Displaying the energy levels without the ZPE correction makes the primary carbon-reaction channel endoergic; correcting for the ZPE results in the reaction becoming exoergic by 2.48 kcal/mol, which is consistent with the ΔE obtained from our CBS-QB3 calculation.

The solvent environment given by the IEFPCM stabilizes the energies of the reactants, complexes, TS, and products in the primary carbon-reaction channel (Figure 12). The dielectric constant increases as the solvent changes from to CCl_4, and $CHCl_3$, and the energy levels stabilize with this increase. Using the IEFPCM with CH_2Cl_2 as a solvent, which has a higher dielectric constant than CCl_4 and $CHCl_3$, we are not able to locate the TS, presumably due to a flattening of the potential energy surface (PES) near the TS as a result of the solvent effect. The solvent stabilizes the TS more than it does the energy of the DMB•–HCl complex. For the same reason, we can not find any TS in the tertiary carbon-reaction channel when applying IEFPCM. Since the energy difference between the TS and the product complex is already negligible in the

gas phase calculation, even a small solvent stabilization makes the PES flat near the TS. This implies that the solvent effect on the tertiary carbon-reaction channel follows the same trend as the primary carbon-reaction channel. Although the solvent stabilizes the energy levels for the primary reaction channel, the energy barriers stays almost the same (3.32 kcal/mol for the gas phase, 2.94 kcal/mol for CCl_4, and 2.86 kcal/mol for $CHCl_3$) because both the reactant complex and the TS energy levels stabilize in a similar fashion. More importantly, the TS for both channels lies below the asymptote of the reactants, indicating barrierless reactions.

The TS calculations for the reactions of Cl atoms with the alkenes DMBE and DMHD reveal different features from the energy profiles of the Cl + DMB reaction (Figures 13 and 14). In the gas phase calculations, we only find the energy minimum that corresponds to the product complexes (DMBE$^{\bullet}$–HCl and DMHD$^{\bullet}$–HCl); there do not appear to be any reactant complexes or TSs for either reaction. Joalland *et. al*. reported similar results for the calculation of Cl atom reaction with isobutene.[7] Their gas phase calculations show that the direct hydrogen abstraction channel of the Cl + isobutene reaction is barrierless and has no reactant complex or TS; only the local minimum of the product complex (isobutyl$^{\bullet}$–HCl) exists.[7] Also, the authors found an indirect abstraction channel, an addition–elimination reaction pathway that precedes *via* roaming, and this TS connects the addition complexes (1-chloro-2-methylpropyl and 2-chloro-2-methylpropyl radicals) and the product complex.[7] In the condensed phase, it is likely that collisions with the solvent stabilize the addition complexes, thus forming stable radical adducts from which the subsequent elimination reaction is unlikely. For instance, the activation energy of the addition–elimination reaction path for the isobutyl$^{\bullet}$–HCl addition complex is large (>18.7 kcal/mol), according to the calculations of Joalland *et. al*.[7] Further, density functional theory calculations determine a well depth for the addition complex in the Cl + allene reaction of about

Figure 13. Calculated energy profiles of the Cl + DMBE reactions in the gas phase (black), CCl_4 (red), $CHCl_3$ (blue), and CH_2Cl_2 (green). The representative structures are the reactants complex (left), TS (middle), and products complex (right) taken from the IEFPCM (CCl_4) calculations. DMBE$^{\bullet}$ is the allyl radical that form after hydrogen is abstracted. The energy levels do not include the ZPE correction.

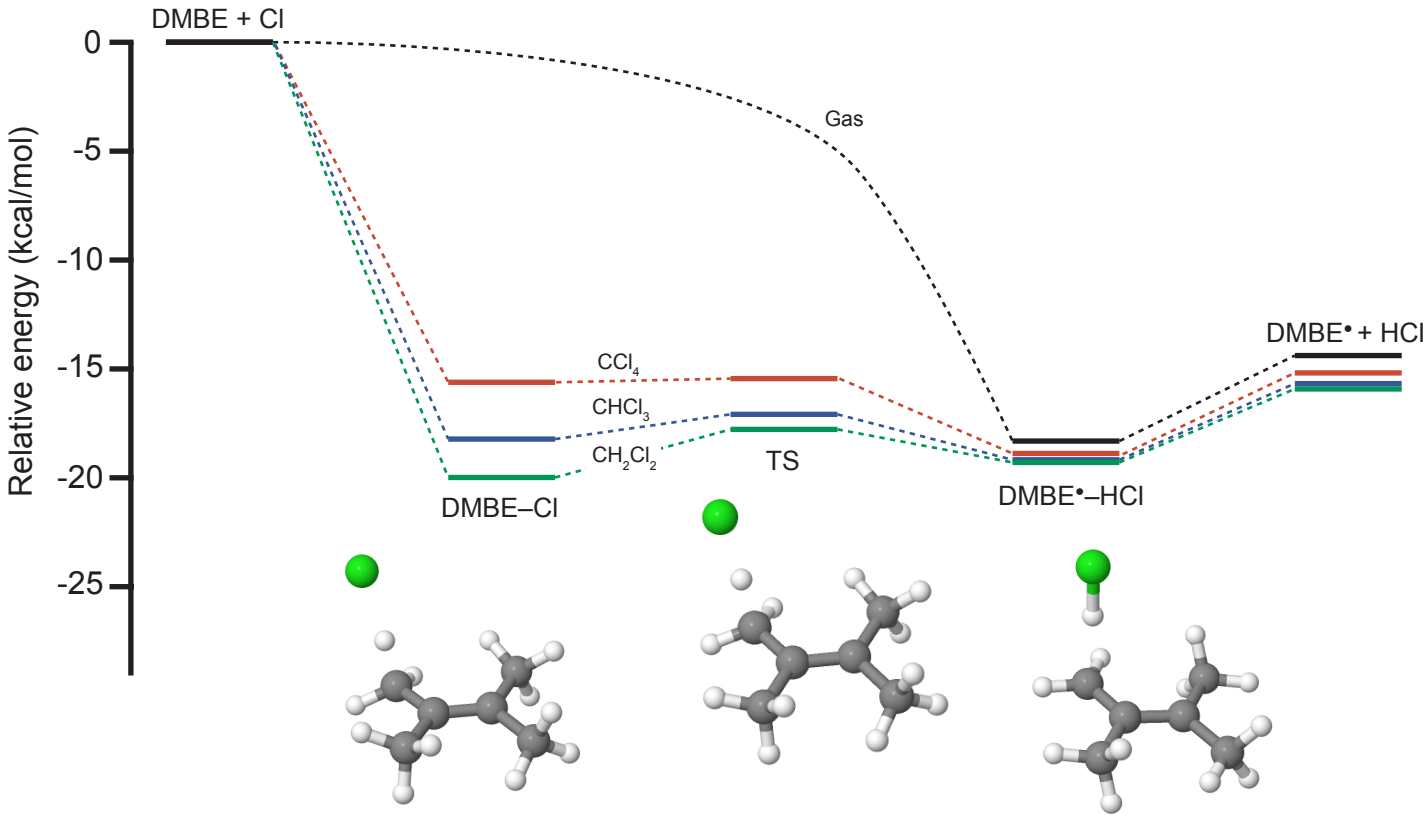
DMBE + Cl
0
-5
-10
-15
-20
-25
Relative energy (kcal/mol)
Gas
CCl4
CHCl3
CH2Cl2
TS
DMBE–Cl
DMBE•–HCl
DMBE• + HCl

Figure 14. Calculated energy profiles of the Cl + DMHD reactions in the gas phase (black), CCl_4 (red), $CHCl_3$ (blue), and CH_2Cl_2 (green). The representative structures are the reactants complex (left), TS (middle), and products complex (right) taken from the IEFPCM (CCl_4) calculations. DMHD$^{\bullet}$ is the allyl radical that form after hydrogen is abstracted. The energy levels do not include the ZPE correction.

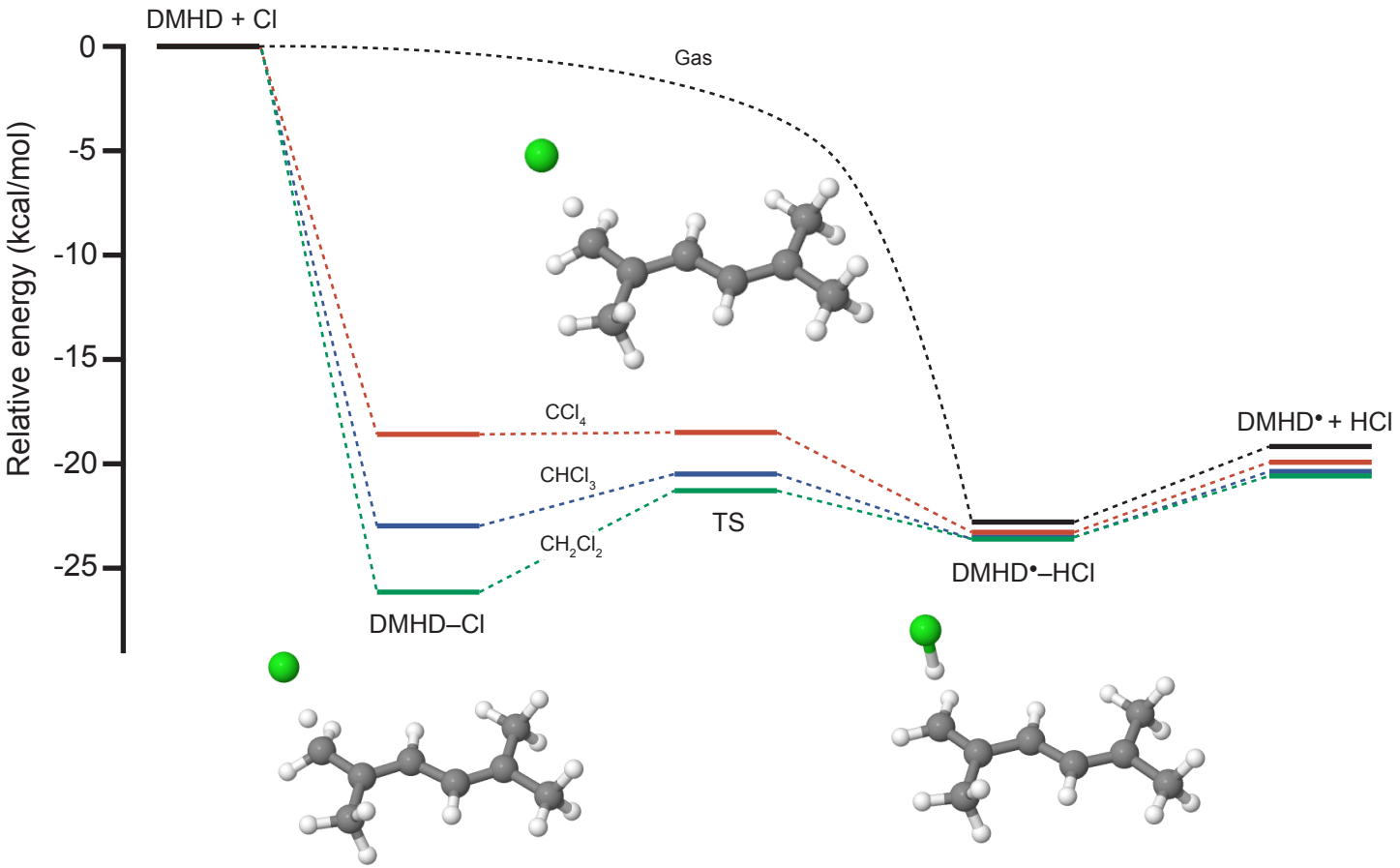
DMHD + Cl
Gas
0
-5
-10
-15
-20
-25
Relative energy (kcal/mol)
CCl4
CHCl3
CH2Cl2
TS
DMHD•–HCl
DMHD• + HCl
DMHD–Cl

40 kcal/mol,[34] and the activation energy of the addition–elimination path is estimated to be about 43.3 kcal/mol.[5] Moreover, the large amplitude motions (which describe a roaming like mechanism) of the addition complexes that can lead to products are less probable in the presence of the surrounding solvent molecules.[6] Therefore, we expect the contribution of the addition–elimination reaction to the production of HCl to be negligible in our measurements, and we do not consider this reaction path in our calculations.

Using IEFPCM to examine the solvent effect, results in changes to the energy profiles of both the Cl + DMBE and the Cl + DMHD reactions (Figures 13 and 14). Interestingly, solvation *via* the IEFPCM of all three solvents (CCl_4, $CHCl_3$, and CH_2Cl_2) recovers the energy levels for the reactant complex, TS, and product complex in both the DMBE and DMHD reactions. As displayed in Figures 13 and 14, the reactant complexes that we obtain here are different from the addition complexes that are involved in the addition–elimination reaction path. In these reactant complexes, a Cl atom aligns linearly with one of the methyl hydrogens, instead of being added to a carbon atom to give a chlorinated radical. The corresponding TS structures also possess a collinear Cl–H–C geometry, like in the Cl + DMB reaction. These geometries indicate that the pathway recovered by solvation is the direct abstraction reaction path. When changing the solvent between CCl_4, $CHCl_3$, and CH_2Cl_2, the energy of the reactant complex decreases and this stabilization is greater than that of the TS, resulting in a slight increase in the energy barrier from the reactant to product complexes. The barrier changes from 0.16, 1.14, and 2.22 kcal/mol for the Cl +DMBE reaction, and it changes to 0.09, 2.48, and 4.86 kcal/mol for the Cl + DMHD reaction as the dielectric constant increases from 2.24, 4.81, and 8.93 (CCl_4, $CHCl_3$, and CH_2Cl_2).[35] As in the case of DMB, the TSs lie below the reactant asymptote, making both reactions barrierless.

3.4 Discussion

3.4.1 Effects of solvation on the reactions of Cl atoms

As mentioned above, the reaction rates of Cl + alkane in the condensed phase are, in general, an order of magnitude smaller than those measured in the gas phase. For Cl atom reactions with *n*-pentane, *n*-hexane, *n*-heptane, and cyclohexane, the bimolecular reaction rates in the condensed phase are ~ 10 to 20 times smaller than those in the gas phase.[18,19] The bimolecular reaction rate of the Cl + DMB reaction follows the same trend. We measure its condensed phase reaction rate to be 1.5 (± 0.5) × 10^{10} $M^{-1}s^{-1}$ in CCl_4 and 0.7 (± 0.1) × 10^{10} $M^{-1}s^{-1}$ in $CDCl_3$, these values are roughly 8 and 18 times smaller than the gas phase reaction rate, 12.4 (± 0.4) × 10^{10} $M^{-1}s^{-1}$.[19]

For the Cl + DMBE and the Cl + DMHD reactions, a direct comparison of the bimolecular reaction rates between the gas and condensed phases is impossible due to the lack of gas phase reaction rates. However, we can compare the gas phase reaction rate of the Cl atom reaction with 2-methyl-2-butene (the closest analogue of DMBE with a known rate) to the K_{bi} of the Cl + DMBE reactions we measure in this study. Ezell *et. al*. investigated the gas phase reactions of chlorine atom with a series of alkenes, and the bimolecular reaction rate of the Cl + 2-methyl-2-butene reaction was determined to be 3.95 (± 0.32) × 10^{10} cm^3 $molecule^{-1}$ s^{-1} (2.38 (± 0.19) × 10^{11} M^{-1} s^{-1}).[36] Using this gas phase value for comparison, we might consider the condensed phase reaction rate of the Cl + DMBE reaction (3.6 (± 0.3) × 10^{10} M^{-1} s^{-1} in CCl_4) to be roughly 10 times smaller than its gas phase analogue. However, the reported gas phase reaction rate for 2-methyl-2-butene includes contributions from the Cl addition reaction (which forms a chlorinated radical adduct) and both the direct and indirect (addition–elimination)

hydrogen abstraction reactions (which form HCl and an alkyl radical). Ezell *et. al*. developed a structure–reactivity model to separate the contributions of these three reaction pathways in reaction of Cl atoms with alkenes.[36] They describe the overall reaction rate as the sum of the addition reaction (k_{add}), the hydrogen abstraction reactions from allyl carbons (k_{allyl}), and hydrogen abstractions from all other carbons that can donate a hydrogen (k_{alkyl}). In their model, k_{alkyl} is calculated by using the structure–reactivity model already developed for the Cl + alkane reactions. Once they have determined k_{alkyl} they fit their data with a generalized reduced gradient nonlinear optimization code, and minimize the difference between the calculated and measured reaction rates to obtain the best fit for k_{add} and k_{allyl}. According to their model, the hydrogen abstraction reaction rate of the Cl + 2-metyl-2-butene reaction is 6.14×10^{10} M^{-1} s^{-1}.[36] While this value is still larger than the condensed phase reaction rate of the Cl + DMBE reaction, these two values are now much closer than in the alkane case. We can further extend this model to the Cl + DMBE reaction, adding the contribution of one more methyl group to the hydrogen abstraction reaction rate of the Cl + 2-methyl-2-butene reaction, and the resulting reaction rate is 8.19×10^{10} M^{-1} s^{-1}.

This model does not distinguish between direct abstraction and the addition–elimination pathway when estimating hydrogen abstraction reaction rates. However, the recent gas phase study of the Cl + DMBE reaction strongly suggests that the contribution of addition–elimination reaction channel is not significant even under single collision conditions.[6] Moreover, Orr-Ewing and coworkers recently carried out quasi-classical trajectory calculations on the Cl + propene reaction to assess the contributions of the direct and indirect hydrogen abstraction pathways. The calculations observe only a small fraction of the trajectories sampling the addition reaction pathway, further eluding that the indirect abstraction channel is a minor pathway that likely does

not contribute significantly to the overall reaction rate.[37] For the Cl + DMBE reaction, the addition pathway is likely to be even more unfavorable due to the larger number of allyl carbons, which not only provide energetically accessible hydrogens but, also, sterically hinder the Cl atom's approach to the double bond. Therefore, we expect the real gas phase reaction rate for the direct hydrogen abstraction of the Cl + DMBE reaction to be larger than the value estimated by the structure–reactivity model in the above. With the gas phase rate constant of 8.19×10^{10} M^{-1} s^{-1}, to our best approximation, the gas phase reaction rate for this reaction is larger, by more than a factor of 2, than the condensed phase reaction rate in CCl_4.

Stabilizing or destabilizing the relative energies of reactants, products, and the TS is one of the important roles of the solvent, and this relative energy changes alter the activation energies and influence the bimolecular reaction rate in the condensed phase.[38] Electrostatic and other intermolecular influences of a solvent can affect a reaction rate by shifting energy levels and changing the activation energy: in addition to these static effects, the solvent can also dynamically influence a reaction rate *via* collisions over the course of a reaction.[8] Many theoretical models attempt to account for this dynamic solvent effect, often termed as solvent friction or solvent collisions, in their predictions of reaction rates.[8] For example, the Langevin equation describes the frictional and stochastic forces imposed on the reacting species by the solvent along a reaction coordinate.[39] In addition, Kramers theory describes the way in which the solvent friction can induce re-crossing of the TS from the exit channel back toward the entrance channel, causing a smaller reaction rate than predicted by transition state theory.[40] The still more sophisticated Grote-Hynes theory, considers a time-dependent solvent friction based on the generalized Langevin equation;[41,42] both the Langevin equation and Kramers theory use a constant solvent friction.

Figures 12, 13, and 14 show the results of our quantum calculations, and indicate that the energy profiles of the reactions in the condensed phase are not remarkably different from those in the gas phase in terms for all three reactions; in all cases of the condensed phase calculations, the TS is located lower in energy than the reactants, and the energy difference between the reactant complex and the TS is small. As long as there is not sufficient cooling to stabilize the reactant complex, all three of these reactions can proceed in a barrierless fashion regardless of the phase. Therefore, it seems that the static effects of the solvent on the reactions are trivial. This indicates that the dynamic effects of the solvent play an important role in reducing the reaction rates of the Cl + DMB and DMBE reactions in the condensed phase. This is in agreement with the encounter-limited rates obtained for all three of these reactions.

In comparing condensed phase reactions to their gas phase counterparts in terms of the branching ratios and the degree of vibrational excitation in products, a general trend is emerging as more condensed phase studies of bimolecular reactions become available. In general, the condensed phase reactions yield a lower degree of vibrational excitation and, for a given vibrational product, a lower branching into vibrationally excited products.[9,12,43,44] The f_v(v=1) of the Cl + DMBE reactions in the condensed phase is smaller than that of the Cl + propene reactions in the gas phase, as mentioned earlier.[20] Moreover, a recent gas phase study demonstrated that the Cl + DMBE reaction produces HCl products that are in higher vibrational levels in the gas phase than those accessed in the condensed phase.[6] A recent review paper proposes three plausible explanations for this dampened vibrational excitation of the HCl products in the condensed phase reactions.[9] The dampening could occur because of coupling of the post-TS motions of the developing products and the solvent bath modes, because of the displacement of the TS due to a modified reacting form of Cl atoms in solution (complexation of

the radical with solvent molecules), or because of differing contributions of the addition–elimination reaction path. However, as mentioned above, the recent gas phase study of Cl + DMBE and the quasi-classical trajectory calculations of Cl + propene encourage us to discount the last explanation.[6,37] Although there is no comparable gas phase study for the Cl + DMHD reaction, it seems that this reaction also follows the general trend because we observe less vibrational excitation of HCl products in the Cl + DMHD reactions than its calculated ΔE predicts.

Within the condensed phase, the branching ratio of vibrationally excited HCl products, Γ (v=1), clearly exhibits a solvent viscosity dependence in the reactions of Cl atoms with both DMBE and DMHD; in the less viscous solvent, $CDCl_3$, Γ (v=1) is larger and *vice versa*. Our electronic structure calculations predict that the locations of the TS for both reactions are nearly the same and do not change significantly for the different solvents. The H-Cl bond lengths at the calculated TSs are roughly 1.50 to 1.60 Å for the Cl + DMBE reactions and roughly 1.52 to 1.65 Å for the Cl + DMHD reactions, depending on the solvent used. Therefore, it seems that the reduced solvent friction is the major attribute that leads to the increased Γ (v=1) in $CDCl_3$, rather than the static effects that may change the shape or location of the TS. Furthermore, the nearly two-fold increase in the Γ (v=1) obtained in $CDCl_3$ strongly correlates with the ratio of the viscosities between CCl_4 (viscosity at RT, 0.908 cP) and $CDCl_3$ (viscosity at RT, 0.537 cP).[35] Thus, we belive that the solvent friction (the first explanation given above) dampens the vibrations, so the more viscous solvent yields a lower Γ (v=1).

The trend in the branching ratios follows the solvent viscosity, but the bimolecular reaction rates, K_{bi}, do not follow solvent viscosity as expected. A simple diffusion model predicts that encounter-limited reactions follow the solvent viscosity; the more viscous the solvent, the

smaller the reaction rate. Yet, our results show that the reaction rates increase in the more viscous solvent, CCl_4. This diffusion model is clearly too simplified for these systems. One aspect that increases the complexity of the reactions studied is the use of the solvent as the precursor for the Cl atoms. Using two different molecular Cl sources will result in different initial energies for the Cl atoms, which can affect how quickly they leave the solvent cage and, thus, the reaction rates. There will also be different complex formation energetics and dynamics. To really understand the observed solvent effects, more sophisticated simulations, such as molecular dynamics (MD) with empirical valence bond (EVB) model, may need to be performed.[45]

3.4.2 Comparisons of the reactions of Cl atoms with DMB, DMBE, and DMHD

Since all three of the Cl atom reactions in this study are encounter-limited with the TS playing a minimal role in their reaction dynamics, the endothermicity and molecular structures are responsible for the differing dynamics and reaction rates. In both solvents, the reaction rates of the Cl + DMBE reaction are about twice those of the Cl + DMB reaction even though DMB has two more hydrogen atoms available for abstraction. Since the molecular structures of DMB and DMBE are very similar and these reactions are in the encounter-limited regime, the difference in the reaction rates likely reflects the effects of the C=C bond. If we add one more C=C bond, as with DMHD, the bimolecular reaction rates become even faster. The reaction rate of the Cl + DMHD reactions approaches the diffusion limit, in fact, the reaction rate in CCl_4 seems to be even a bit faster ($\sim 10^{11}$ $M^{-1}s^{-1}$ *vs*. $\sim 10^{10}$ $M^{-1}s^{-1}$). A condensed phase bimolecular reaction rate can be faster than the diffusion limit when there are intermolecular forces between the reactants or a long-range transfer occurs.[46] Reactions of solvated electrons are good

examples.[46] For example, the interaction between a charge and permanent dipole of solvated electrons with aromatic molecules can result in rate on the order of 10^{11} $M^{-1}s^{-1}$;[47] long-range electron transfer reactions also occur in the reactions of solvated electrons.[46] In the reaction of Cl atoms with alkenes, the strongly electrophilic Cl atoms and the electron density and π character of the C=C bonds in alkenes make attractive forces probable. Perhaps, intermolecular forces direct the Cl atoms and DMHD molecules toward each other at long range, so the reactants approach is not simply dictated by diffusion, then upon encounter they immediately react. If we assume that the two-fold increase in the reaction rates of the Cl + DMBE reactions from the Cl + DMB reactions is due to the effects of the C=C bond, then we could adopt a doubling of the reaction rate with the addition of a C=C bond. However, then the magnitude of the rate of increase in the Cl + DMHD reactions is an unexpectedly high four- or five-fold increase from the Cl + DMBE reactions. It is conceivable that this discrepancy is due to the differences in molecular geometries.

Figure 15 presents a comparison of the optimized structures for DMBE and DMHD. The DMBE structure is more compact than the DMHD. In the DMBE structure, the closest H–H distances between adjacent methyl groups are 1.9 Å for the parallel direction to C=C bond and 2.5 Å for the perpendicular direction to C=C bond. In the DMHD structure, the closest H–H distances between adjacent methyl groups are 2.6 Å, and the closest H–H distances between methyl group and vinyl hydrogen are 2.3 and 2.0 Å. These calculations show that in DMHD there is an easier approach for the Cl atoms. These steric effects specify the cone of acceptance for the reactions and the possible steering of the intermolecular interactions.

In looking at the branching ratios of HCl (v=1), Γ (v=1), we find that Γ (v=1) is larger in the Cl + DMHD reaction than in the Cl + DMBE reactions by roughly a factor of 2. Since the

Figure 15. Energy optimized structures of DMBE (left) and DMHD (right).

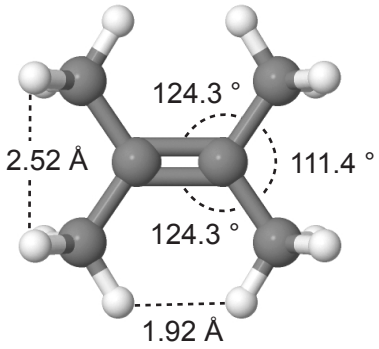

DMBE

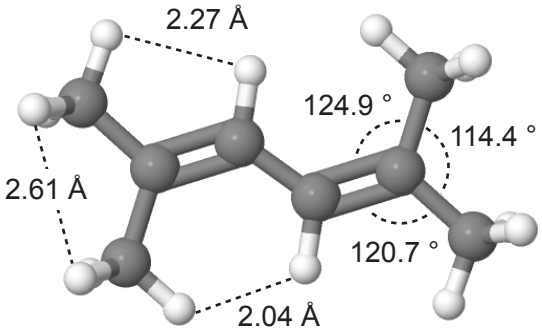

DMHD

locations of the TSs along the H–Cl reaction coordinate do not differ much, as mentioned above, the exoergicity of the reactions appear to dictate the difference in their branching ratios. Both reactions are apparently barrierless (the TS lies below the initial energy of the reactants) and highly exoergic. The Cl + DMHD reaction is more exoergic and, thus, has more energy available to products, in particular more energy that can be deposited into the vibrationally excited HCl products, resulting in a higher branching ratio, Γ (v=1), than for the Cl + DMBE reaction.

3.5 Summary

We have investigated the reactions of Cl atoms with a saturated hydrocarbon (DMB) and an unsaturated hydrocarbons having two C=C bonds (DMHD) in chlorinated solvents, extending upon the recent study of the Cl + DMBE reactions.[12] Using two-photon excitation at 267 nm, we photolyze CCl_4 and $CDCl_3$ to generate Cl atoms in solution. We follow the hydrogen abstraction reactions of these Cl atoms by monitoring the formation of the HCl products with transient IR absorption measurements. Based on CBS-QB3 calculations, the Cl + DMHD reaction is highly exoergic by 102 kJ/mol, while the Cl + DMB reaction is mildly exoergic (13 or 31 kJ/mol). As a result, the Cl + DMHD reaction produces vibrationally excited HCl (up to v=1), like in the Cl + DMBE reaction, and the Cl + DMB reaction produces only ground state HCl. The bimolecular reaction rates of all three reactions are encounter-limited; 1.5 (± 0.5) × 10^{10} $M^{-1}s^{-1}$ for Cl + DMB, 3.6 (± 0.3) × 10^{10} $M^{-1}s^{-1}$ for Cl + DMBE, and 17.5 (± 1.6) × 10^{10} $M^{-1}s^{-1}$ for Cl + DMHD. The detailed energy profile calculations indicate that all three reactions are barrierless, supporting these fast reaction rates. The reaction rates of the Cl + DMB reaction in the condensed phase are slower than the corresponding gas phase reaction rates by an

order of magnitude, which is comparable to reactions of Cl atoms with other alkanes. The reaction rates of the Cl + DMBE reactions in the condensed phase is slower than in the gas phase (using rates that are approximated by a structure-reactivity model). Calculations suggest that dynamic solvent effects are mainly responsible for the reduced reaction rates in the condensed phase. Exocergicity and solvent friction dictates the branching ratios of HCl (v=1).

Overall, the reaction dynamics of Cl atom reactions in the condensed phase are akin to those in the gas phases; we find fast reaction rates without significant energy barriers and energy disposals into the products based on the exoergicity of the reaction. However, the solvent still plays a crucial role in damping the vibrations of nascent HCl products, allowing for more vibrational excitation in a less viscous solvent. Interestingly, the bimolecular reaction rate of the Cl + DMHD reaction in CCl_4 seems to exceed those of common diffusion-limited reactions. This may be indicative of an attractive intermolecular force acting on the reactants. Plus, the bimolecular reaction rates do not follow the expected trend in the solvent viscosity even though the reactions are in an encounter-limited regime; a simple diffusion model breaks down and a more sophisticated theory needs to come into play.

References

(1) Wayne, R. P. *Chemistry of atmospheres. An introduction to the atmospheres of Earth, the planets, and their satellites.. RP Wayne. Clarendon Press, Oxford, England.* **1985**, *1*.

(2) Finlayson-Pitts, B. J. *Chem. Rev.* **2003**, *103*, 4801.

(3) Yoon, S.; Holiday, R. J.; Crim, F. F. *J. Chem. Phys.* **2003**, *119*, 4755.

(4) Holiday, R. J.; Kwon, C. H.; Annesley, C. J.; Fleming Crim, F. *J. Chem. Phys.* **2006**, *125*, 133101.

(5) Taatjes, C. A. *Int. Rev. Phys. Chem.* **1999**, *18*, 419.

(6) Preston, T. J.; Dunning, G. T.; Orr-Ewing, A. J.; Vázquez, S. A. *J. Phys. Chem. A* **2014**, *118*, 5595.

(7) Joalland, B.; Shi, Y.; Kamasah, A.; Suits, A. G.; Mebel, A. M. *Nat. Commun.* **2014**, *5*.

(8) Orr-Ewing, A. J. *J. Chem. Phys* **2014**, *140*, 090901.

(9) Orr-Ewing, A. J. *Annu. Rev. Phys. Chem.* **2015**, *66*, 119.

(10) Raftery, D.; Iannone, M.; Phillips, C. M.; Hochstrasser, R. M. *Chem. Phys. Lett.* **1993**, *201*, 513.

(11) Sheps, L.; Crowther, A. C.; Carrier, S. L.; Crim, F. F. *J. Phys. Chem. A* **2006**, *110*, 3087.

(12) Abou-Chahine, F.; Greaves, S. J.; Dunning, G. T.; Orr-Ewing, A. J.; Greetham, G. M.; Clark, I. P.; Towrie, M. *Chem. Sci.* **2013**, *4*, 226.

(13) Preston, T. J.; Shaloski, M. A.; Crim, F. F. *J. Phys. Chem. A* **2013**, *117*, 2899.

(14) Grubb, M. P.; Orr-Ewing, A. J.; Ashfold, M. N. R. *Rev. Sci. Instrum.* **2014**, *85*, 064104.

(15) Frisch, M. J.; Trucks, G. W.; Schlegel, H. B.; Scuseria, G. E.; Robb, M. A.; Cheeseman, J. R.; Scalmani, G.; Barone, V.; Mennucci, B.; Petersson, G. A.; Nakatsuji, H.; Caricato, M.; Li, X.; Hratchian, H. P.; Izmaylov, A. F.; Bloino, J.; Zheng, G.; Sonnenberg, J. L.; Hada, M.; Ehara, M.; Toyota, K.; Fukuda, R.; Hasegawa, J.; Ishida, M.; Nakajima, T.; Honda, Y.; Kitao, O.; Nakai, H.; Vreven, T.; Montgomery Jr., J. A.; Peralta, J. E.; Ogliaro, F.; Bearpark, M. J.; Heyd, J.; Brothers, E. N.; Kudin, K. N.; Staroverov, V. N.; Kobayashi, R.; Normand, J.; Raghavachari, K.; Rendell, A. P.; Burant, J. C.; Iyengar, S. S.; Tomasi, J.; Cossi, M.; Rega, N.; Millam, N. J.; Klene, M.; Knox, J. E.; Cross, J. B.; Bakken, V.; Adamo, C.; Jaramillo, J.; Gomperts, R.; Stratmann, R. E.; Yazyev, O.; Austin, A. J.; Cammi, R.; Pomelli, C.; Ochterski, J. W.; Martin, R. L.; Morokuma, K.; Zakrzewski, V. G.; Voth, G. A.; Salvador, P.; Dannenberg, J. J.; Dapprich, S.; Daniels, A. D.; Farkas, Ö.; Foresman, J. B.; Ortiz, J. V.; Cioslowski, J.; Fox, D. J.; Gaussian, Inc.: Wallingford, CT, USA, 2009.

(16) Montgomery, J. A.; Frisch, M. J.; Ochterski, J. W.; Petersson, G. A. *J. Chem. Phys.* **1999**, *110*, 2822.

(17) Abou-Chahine, F.; Preston, T. J.; Dunning, G. T.; Orr-Ewing, A. J.; Greetham, G. M.; Clark, I. P.; Towrie, M.; Reid, S. A. *J. Phys. Chem. A* **2013**, *117*, 13388.

(18) Sheps, L.; Crowther, A. C.; Elles, C. G.; Crim, F. F. *J. Phys. Chem. A* **2005**, *109*, 4296.

(19) Aschmann, S. M.; Atkinson, R. *Int. J. Chem. Kinet.* **1995**, *27*, 613.

(20) Pilgrim, J. S.; Taatjes, C. A. *J. Phys. Chem. A* **1997**, *101*, 5776.

(21) Lew, C. S. Q.; Brisson, J. R.; Johnston, L. J. *J. Org. Chem.* **1997**, *62*, 4047.

(22) Gorman, A. A.; Gould, I. R.; Hamblett, I. *J. Photochem.* **1982**, *19*, 89.

(23) Polli, D.; Altoe, P.; Weingart, O.; Spillane, K. M.; Manzoni, C.; Brida, D.; Tomasello, G.; Orlandi, G.; Kukura, P.; Mathies, R. A.; Garavelli, M.; Cerullo, G. *Nature* **2010**, *467*, 440.

(24) Tao, H.; Allison, T. K.; Wright, T. W.; Stooke, A. M.; Khurmi, C.; van Tilborg, J.; Liu, Y.; Falcone, R. W.; Belkacem, A.; Martinez, T. J. *J. Chem. Phys.* **2011**, *134*, 244306.

(25) Elles, C. G.; Cox, M. J.; Barnes, G. L.; Crim, F. F. *J. Phys. Chem. A* **2004**, *108*, 10973.

(26) Crowther, A. C.; Carrier, S. L.; Preston, T. J.; Crim, F. F. *J. Phys. Chem. A* **2008**, *112*, 12081.

(27) Crowther, A. C.; Carrier, S. L.; Preston, T. J.; Crim, F. F. *J. Phys. Chem. A* **2009**, *113*, 3758.

(28) Rice, S. A. *Diffusion-Limited Reactions*; Elsevier: Amsterdam, 1985; Vol. 25.

(29) Tachiya, M. *Radiat. Phys. Chem. (1977)* **1983**, *21*, 167.

(30) Thomsen, C. L.; Madsen, D.; Poulsen, J. A.; Thøgersen, J.; Jensen, S. J. K.; Keiding, S. R. *J. Chem. Phys.* **2001**, *115*, 9361.

(31) Wang, D.; Phillips, D. L.; Fang, W.-H. *J. Phys. Chem. A* **2003**, *107*, 1551.

(32) Murray, C.; Orr-Ewing, A. J. *Int. Rev. Phys. Chem.* **2004**, *23*.

(33) Jordan, M. J. T.; Del Bene, J. E. *J. Am. Chem. Soc.* **2000**, *122*, 2101.

(34) Farrell, J. T.; Taatjes, C. A. *J. Phys. Chem. A* **1998**, *102*, 4846.

(35) *CRC Handbook of Chemistry and Physics*; 87th ed.; CRC Press: Boca Raton, FL, 2012-2013.

(36) Ezell, M. J.; Wang, W.; Ezell, A. A.; Soskin, G.; Finlayson-Pitts, B. J. *Phys. Chem. Chem. Phys.* **2002**, *4*, 5813.

(37) Hornung, B.; Preston, T. J.; Pandit, S.; Harey, J. N.; Orr-Ewing, A. J. *Unpublished work*.

(38) Crim, F. F. *Faraday Discuss.* **2012**, *157*, 9.

(39) Nitzan, A. *Chemical Dynamics in Condensed Phases*; Oxford University Press: Oxford, 2006.

(40) Kramers, H. A. *Physica* **1940**, *7*, 284.

(41) Grote, R. F.; Hynes, J. T. *J. Chem. Phys.* **1980**, *73*, 2715.

(42) Grote, R. F.; Hynes, J. T. *J. Chem. Phys.* **1981**, *75*, 2191.

(43) Greaves, S. J.; Rose, R. A.; Oliver, T. A. A.; Glowacki, D. R.; Ashfold, M. N. R.; Harvey, J. N.; Clark, I. P.; Greetham, G. M.; Parker, A. W.; Towrie, M.; Orr-Ewing, A. J. *Science* **2011**, *331*, 1423.

(44) Dunning, G. T.; Glowacki, D. R.; Preston, T. J.; Greaves, S. J.; Greetham, G. M.; Clark, I. P.; Towrie, M.; Harvey, J. N.; Orr-Ewing, A. J. *Science* **2015**, *347*, 530.

(45) Glowacki, D. R.; Rose, R. A.; Greaves, S. J.; Orr-Ewing, A. J.; Harvey, J. N. *Nat. Chem.* **2011**, *3*.

(46) Rice, S. A. *Diffusion-limited reactions*; Amsterdam ; New York : Elsevier, c1985., 1985.

(47) Schindewolf, U.; Wünschel, P. *Can. J. Chem.* **1977**, *55*, 2159.

Chapter 4

Time-Resolved Spectroscopic Studies of Vibrationally Driven Reactions of Br Atoms in Solution

4.1 Introduction

Vibrationally mediated chemistry is a fascinating concept by which vibrational excitation drives a reaction toward a particular outcome, perhaps altering the product distribution or reaction rate.[1] The concept of vibrational mediation has been well studied, experimentally and theoretically, for both uni and bimolecular reactions; particularly in the gas phase, where bond- and mode-selective chemistry is now well established.[2-9] Focusing on the influence of vibrations in bimolecular reactions, two key examples (both of which have been studied by our group) are the reaction of HOD + H and the reaction of CH_3D + Cl.

The reaction of HOD with H atoms does not occur under thermal conditions, yet with the use of initial vibrational excitation the reaction proceeds near the gas kinetic collision rate. Furthermore, excitation of these stretching overtones results in reaction almost exclusively *via* the initially excited bond. In addition, reaction of vibrationally excited HOH with H atoms supports a spectator model.[2,10-12] Another interesting case is the reaction of Cl atoms with

methane and its isotopologues; these reactions have proven to be the most prototypical of gas phase reactions. In the particular case of CH_3D + Cl, vibrations having similar amounts of energy but differing nuclear motions allow for chemical control. Moreover, the local mode character of CH_3D allows for good bond selectivity, forming CH_2D + HCl when a C-H oscillator is excited and CH_3 + DCl when the C-D oscillator is excited, and effective mode selectivity, such as a more effective coupling of the C-H stretch to the H-atom abstraction reaction coordinate than the bend. As with HOD, excitations of one or more C-H oscillators follow a spectator model; however, excitation having both C-H and C-D stretching character begin to deviate from the spectator picture.[5-7]

In the condensed phase, there has been significantly less effort to test the idea of vibrational mediation. The coherent control of a condensed phase reaction has been demonstrated for unimolecular processes such as the isomerization reaction of retinal using UV-pulse shaping with a genetic learning algorithm.[13] However, it is perhaps more intuitive to consider the influence of nuclear motions (like those associate with vibrational excitation) on a particular reaction coordinate. This fundamental approach has not been well tested in the condensed phase. In our previous study,[14] we investigated the influence of the C–H stretching coordinate on the isomerization process of trans-stilbene in $CDCl_3$ using overtone excitation. We found that excitation of the first overtone of the C–H stretch does not affect the lifetime of the S_1 state of trans-stilbene, and thus, it does not affect the isomerization rate.

In this study, we test the effects of vibrational excitation on the bimolecular reaction of Br atoms with organic molecules. Hydrogen abstraction *via* a Br atom is highly endoergic, which will suppress the thermally initiated reaction and make the effects of vibrational excitation more obvious in our measurements. In addition, typical endoergicities are close to 3000 cm^{-1}, a value

that is conveniently similar to the energy of the C–H stretch of most organic molecules. Therefore, vibrational excitation of the C–H stretch will provide enough energy to promote the Br reaction using fundamental or overtone excitation. The reaction energetics are given below for two examples that we report on, the reactions of Br atoms with methanol or dimethylsulfoxide (DMSO).[15]

$$Br + CH_3OH \longrightarrow HBr + CH_2OH^{\cdot} \qquad \Delta H = 2989\ cm^{-1}$$

$$\longrightarrow HBr + CH_3O^{\cdot} \qquad \Delta H = 6190\ cm^{-1}$$

$$Br + CH_3S(O)CH_3 \longrightarrow HBr + CH_3S(O)CH_2^{\cdot} \qquad \Delta H = 2269\ cm^{-1}$$

In our experiments, we photolyze either Br_2 or bromoform ($CHBr_3$) using 400 or 267 nm photons to generate Br atoms, and we use near-IR pulses to excite the overtone of the C–H stretch of various organic solvents (or the O–H stretch in the case of a methanol solution). We monitor the evolution of the Br–solvent complex or the $CHBr_3$-Br complex at 400 nm as a probe of the reaction dynamics of Br atoms. We observe an IR-dependent difference in the signal at 400 nm in methanol, DMSO, 2,3-dimethylbutane (DMB), and CH_2Cl_2 solutions. The difference signal has a negative offset, as compared to the baseline, that presumably represents the loss of the Br atom complex due to the reaction between Br atoms and vibrationally excited solvent molecules. Notably, the difference signals obtained in the methanol and DMSO solutions depend on the near-IR pump wavelength (whether it is resonant or off-resonant). While this reinforces our argument, there are possible explanations for this negative offset, like vibrational predissociation of the complex. The UV-probe results show vibrationally driven chemistry, but to claim unambiguously that we have realized the first vibrationally driven bimolecular reaction in the condensed phase, we aim to use an IR probe to monitor the formation of the HBr product.

4.2 Experimental methods

We describe the details of our apparatus elsewhere;[16] what follows is a brief description of our pump-probe setup. The third harmonic of an ultrafast Ti:sapphire laser provides 267 nm photolysis light with a 1 kHz repetition rate. The second harmonic of laser output generates 400 nm light, which we use for photolysis as well as a probe. We generate Br atoms by photolyzing Br_2 and $CHBr_3$ using 1-2 μJ of 400 nm and 267 nm light, respectively. We generate near-IR light with a double-pass BBO OPA. As stated above, we use 400 nm light as a single-wavelength probe, but we can also create a broadband continuum probe beam by focusing 800 nm light onto a CaF_2 window. A computer-controlled mechanical translation stage controls the time delay between the photolysis and near-IR pump pulses, and another stage controls the time delay between these two pump pulses and the probe pulse. All three beams cross each other in a sample solution that flows through a cell with MgF_2 windows and a 1 mm thick polytetrafluoroethylene (PTFE) spacer by means of a peristaltic pump. A pair of Si photodiode detectors monitors the 400 nm probe light to give signal and reference data. We use two mechanical choppers, each of which blocks/unblocks the photolysis and near-IR pump beams at a rate of 500 Hz and 250 Hz. The combinations of the two chopper states results in three different measurements, photolysis (on): near-IR pump (off), photolysis (off): near-IR pump (on), and photolysis (on): near-IR pump (on). We calculate three transient absorption signals based on these combinations of two chopper states; the signals from 'photolysis-only', 'near-IR-only', and 'both beams'. We also calculate a difference signal by taking the signal from 'both beams' and subtracting out the contributions from the other two signals, 'photolysis-only' and 'near-IR-only'. This procedure is done on-the-fly to obtain a difference signal in real time.

We use Br_2 (Sigma-Aldrich, ACS reagent grade ≥99.5%), $CHBr_3$ (Aldrich, 96%), CH_3OH (Sigma-Aldrich, ≥99.9%), DMSO (Sigma, ≥99.5%), DMB (Aldrich, 98%), and CH_2Cl_2 (Sigma-Aldrich, ≥99.5%) as received. The concentrations of the Br_2 and $CHBr_3$ solution are 0.12 M in these experiments.

4.3 Results and discussion

In this study, we envisage the overall reaction based on the dynamics of a reactant, the Br atom. We can monitor the evolution of the Br atoms by means of the absorption bands of either the Br–solvent complex or the *iso*-$CHBr_2$-Br isomer, depending on the Br atom precursor. Therefore, it is first important to understand the behavior of the Br atoms without introducing the IR excitation. With this in mind, we begin by discussing the electronic transient absorption measurements of these species acquired with a broadband continuum probe.

4.3.1 Broadband continuum probe experiments

When we use Br_2 as a precursor, the Br atoms formed from the 400 nm photolysis light quickly form a van der Waals complex with the solvent molecules. If no reaction occurs, they will eventually undergo geminate recombination to re-form the parent molecule, Br_2. Figure 1 shows the results of electronic transient absorption measurements for a solution of Br_2 in CH_3OH following 400 nm excitation. The band near 380 nm grows in immediately after the photolysis beam arrives (t=0) and maximizes after ~5ps. Then, it decays at a relatively fast rate until ~30 ps, at which point the rate of decay slows. This band is due to the absorption of the Br–CH_3OH complex, and its temporal behavior represents the formation of this complex and geminate recombination of Br_2. The hydrogen abstraction reactions of Br + CH_3OH is highly endothermic,

Figure 1. Transient absorption measurements of a Br_2 solution in CH_3OH using a broadband UV/VIS continuum probe after 400 nm excitation: (a) contour plot, (b) transient spectra at selected time delays, (c) the time-dependent absorption change for a probe wavelength of 380 nm, and (d) enlarged view of (c) in early time delays.

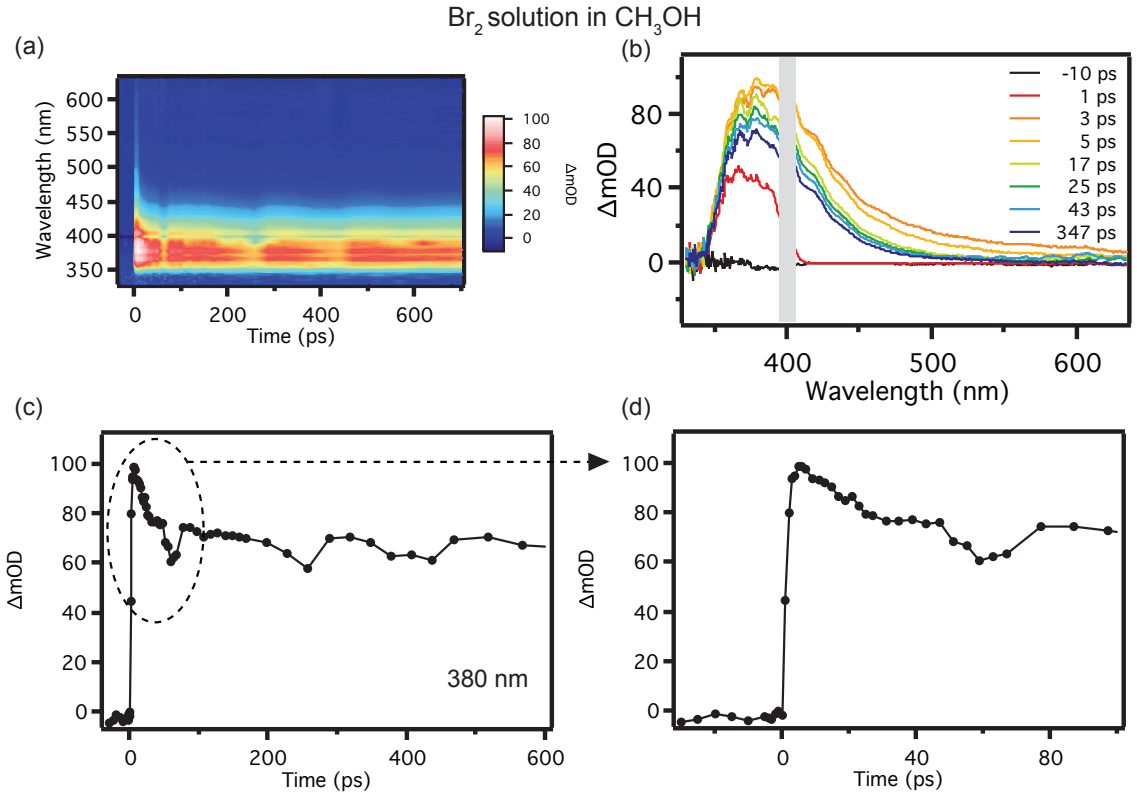
Br2 solution in CH3OH
(a)
Wavelength (nm)
600
550
500
450
400
350
0
200
400
600
Time (ps)
100
80
60
40
20
0
ΔmOD
(b)
ΔmOD
80
40
0
400
500
600
Wavelength (nm)
-10 ps
1 ps
3 ps
5 ps
17 ps
25 ps
43 ps
347 ps
(c)
ΔmOD
100
80
60
40
20
0
380 nm
0
200
400
600
Time (ps)
(d)
ΔmOD
100
80
60
40
20
0
0
40
80
Time (ps)

regardless of which hydrogen (CH_3 or OH) reacts. For this reason, we discount the possibility of thermally driven reactions between the Br atoms and the CH_3OH solvent. The data we obtain to monitor the dynamics of the Br–CH_3OH complex also contain information on the evolution of the Br_2. This is due to the overlap of the absorption spectrum of Br_2 with the transient absorption band of the complex; the steady-state absorption band of Br_2 in solution ranges from 350 nm to 550 nm, peaking near 420 nm. Without any information about the absorption cross sections of the Br–CH_3OH complex, the deconvolution of these two transient signals is non-trivial.

When we use $CHBr_3$ as a Br atom precursor the dynamics differ from the case of photolyzing Br_2. Figures 2 and 3 show the transient absorption spectra of a solution of $CHBr_3$ in DMB and CH_2Cl_2, respectively, and their time evolutions following Br atom generation using 267 nm photolysis light. In both solutions, the absorption band near 400 nm appears at early time delays and a broad absorption feature slowly grows in near 435nm (DMB solvent) and 480 nm (CH_2Cl_2 solvent). In our previous study, we observed very similar dynamics in the transient absorption measurements of a $CHBr_3$ solution in CCl_4; an absorption feature appeared in the shorter wavelength regions, near 400 nm, at early delay times, followed by the slow growth of a broad absorption band near 450 nm.[16] With the aid of time-resolved IR absorption spectroscopy and quantum calculations, we were able to assign the broad absorption band near 450 nm to *iso*-$CHBr_2$-Br and the absorption feature near 400 nm at early time delay to $CHBr_3$-Br van der Waals complex.[16] The time constants for the rise of the *iso*-$CHBr_2$-Br absorption band are 19 and 124 ps in CCl_4 (fitted with a double exponential).[16] We obtain similar time constants from the double exponential fit of this isomer signal in DMB (13 and 25 ps) and CH_2Cl_2 (11.4 and 87 ps) solutions; see Figures 2 and 3. The peak maximum of the broad absorption feature that appears at longer wavelengths red shifts as the solvent changes from DMB to CH_2Cl_2, while the absorption

Figure 2. Transient absorption measurements of a $CHBr_3$ solution in DMB using a broadband UV/VIS continuum probe after 267 nm excitation: (a) contour plot, (b) transient spectra at selected time delays, and (c) the time-dependent absorption change for a probe wavelength of 435 nm, (d) enlarged view of (c) in early time delays. The solid red line in (d) is the double exponential fit.

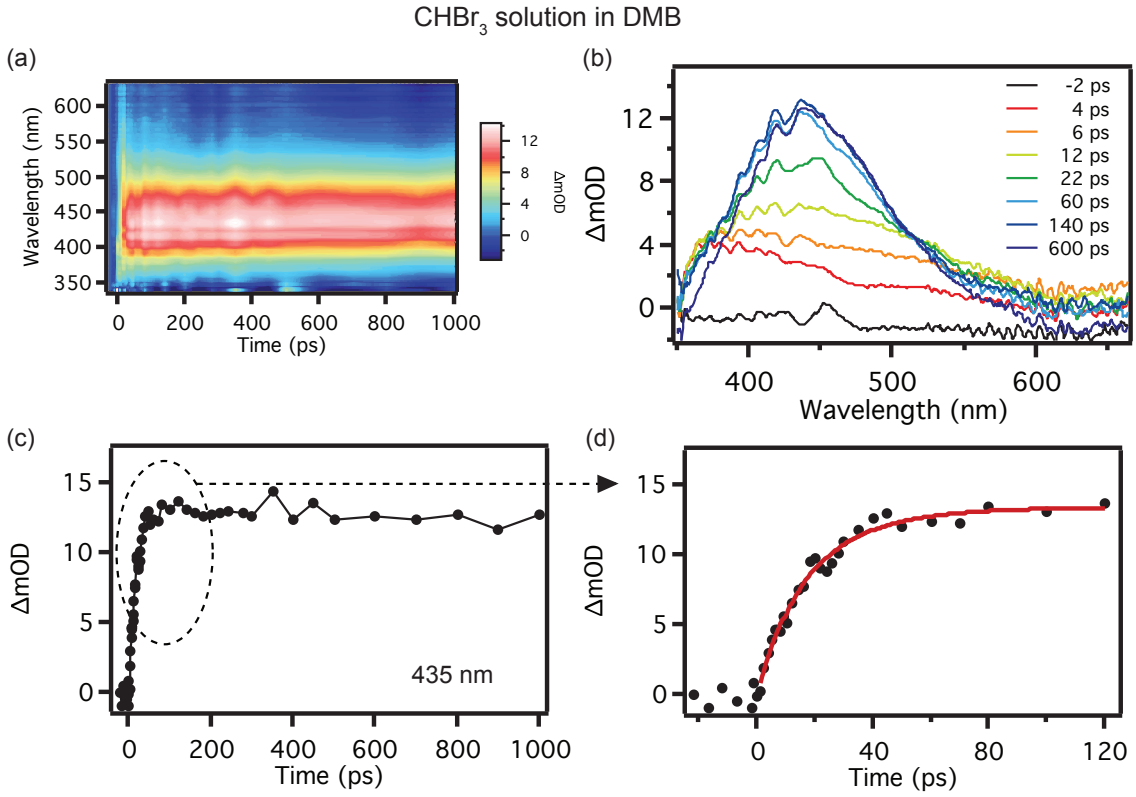
CHBr3 solution in DMB
(a)
Wavelength (nm)
600
550
500
450
400
350
0
200
400
600
800
1000
Time (ps)
12
8
4
0
ΔmOD
(b)
ΔmOD
12
8
4
0
400
500
600
Wavelength (nm)
-2 ps
4 ps
6 ps
12 ps
22 ps
60 ps
140 ps
600 ps
(c)
ΔmOD
15
10
5
0
435 nm
0
200
400
600
800
1000
Time (ps)
(d)
ΔmOD
15
10
5
0
0
40
80
120
Time (ps)

Figure 3. Transient absorption measurements of a $CHBr_3$ solution in CH_2Cl_2 using a broadband UV/VIS continuum probe after 267 nm excitation: (a) contour plot, (b) transient spectra at selected time delays, and (c) the time-dependent absorption change for a probe wavelength of 480 nm, (d) enlarged view of (c) in early time delays. The solid red line in (d) is the double exponential fit.

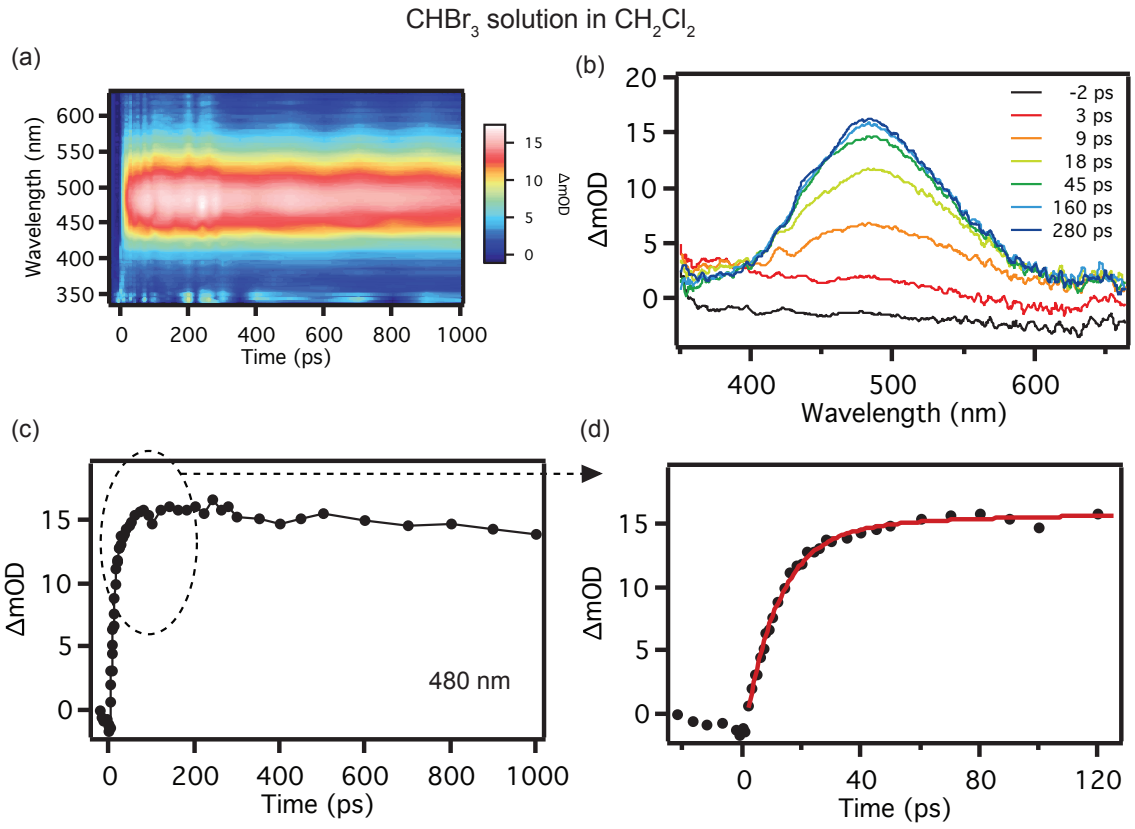
CHBr3 solution in CH2Cl2
(a)
Wavelength (nm)
600
550
500
450
400
350
0
200
400
600
800
1000
Time (ps)
15
10
5
0
ΔmOD
(b)
ΔmOD
20
15
10
5
0
-2 ps
3 ps
9 ps
18 ps
45 ps
160 ps
280 ps
400
500
600
Wavelength (nm)
(c)
ΔmOD
15
10
5
0
480 nm
0
200
400
600
800
1000
Time (ps)
(d)
ΔmOD
15
10
5
0
0
40
80
120
Time (ps)

band that appears at shorter wavelengths stays nearly the same. In the previous study we observed the same trend; the absorption band of *iso*-$CHBr_2$-Br shifts to lower energy as the solvent changes from a lower dielectric medium to a higher dielectric medium and the absorption band of $CHBr_3$-Br does not shift.[16] Therefore, we argue that as in the CCl_4 solvent study, *iso*-$CHBr_2$-Br and $CHBr_3$-Br are responsible for the two absorption features that we observe in the solutions of $CHBr_3$ in DMB and CH_2Cl_2.

Interestingly, the photolysis of $CHBr_3$ in DMSO (Figure 4) reveals different dynamics from the photolysis of CHBr3 in DMB and CH_2Cl_2. As in the photolysis of $CHBr_3$ in DMB and CH_2Cl_2 there is a broad absorption band that appears near 450 nm after photolysis of $CHBr_3$ in DMSO, but the rate of its appearance is quite different. The rise of this feature is complete within ~5 ps, after which it continuously decays. Also, in DMSO, no absorption feature appears near 400 nm at early delay times, indicating that the formation of $CHBr_3$-Br complex is insignificant. These aspects are reminiscent of our Br_2 in CH_3OH observations, perhaps suggesting the formation of a Br-solvent complex. Moreover, Sumiyoshi *et. al*. observed the same transient absorption feature in their pulse radiolysis study of DMSO/$CBrCl_3$ mixtures, and they assigned this feature to an absorption band of Br–DMSO complex.[17] The rise times, however, do not match since they used a diluted DMSO solution; they measured a rise time of a few hundred ns, which is much slower than we observe here. Therefore, we believe that the transient absorption band that appears following photolysis of $CHBr_3$ in DMSO is from the formation of the Br–DMSO complex, and this bands decays due to the geminate recombination of the $CHBr_3$. The interaction of a Br atom with DMSO would be stronger than with non-interacting solvents (such as CCl_4, CH_2Cl_2, and DMB) due to the high polarity of DMSO. This strong interaction seems to favor the formation of the Br–DMSO complex over the $CHBr_3$-Br complex, which is perhaps not

Figure 4. Transient absorption measurements of a $CHBr_3$ solution in DMSO using a broadband UV/VIS continuum probe after 267 nm excitation: (a) contour plot, (b) transient spectra at selected time delays, and (c) the time-dependent absorption change for a probe wavelength of 450 nm, (d) enlarged view of (c) in early time delays.

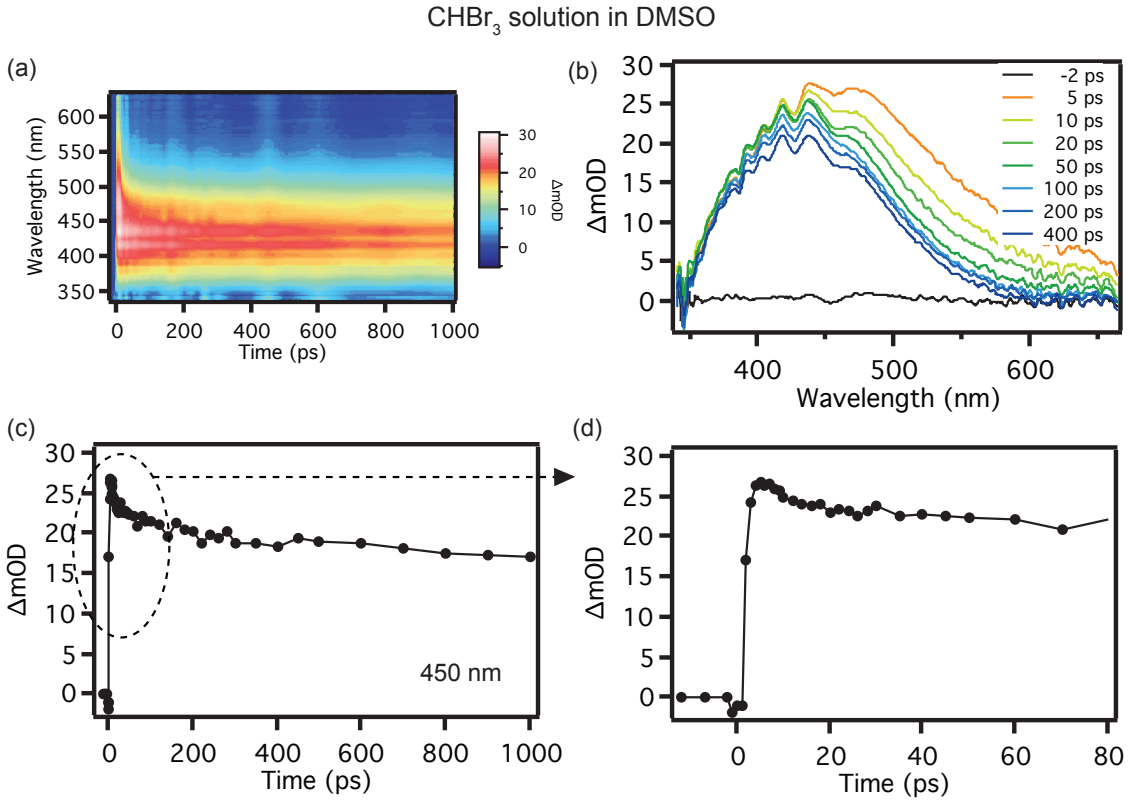
CHBr3 solution in DMSO
(a)
Wavelength (nm)
600
550
500
450
400
350
0
200
400
600
800
1000
Time (ps)
30
20
10
0
ΔmOD
(b)
ΔmOD
30
25
20
15
10
5
0
-2 ps
5 ps
10 ps
20 ps
50 ps
100 ps
200 ps
400 ps
400
500
600
Wavelength (nm)
(c)
ΔmOD
30
25
20
15
10
5
0
450 nm
0
200
400
600
800
1000
Time (ps)
(d)
ΔmOD
30
25
20
15
10
5
0
0
20
40
60
80
Time (ps)

surprising especially when considering the relative number densities of the DMSO and $CHBr_3$. Likewise, when this strong interaction is absent, as in the other solutions we have studied (CCl_4, CH_2Cl_2, and DMB), the $CHBr_3$-Br complex and not the Br-solvent complex forms.

4.3.2 Single wavelength (400 nm) probe experiments with photolysis and near-IR pump pulses

To realize vibrationally driven bimolecular reactions in the condensed phase, we need to consider the possible limitations of the experimental approaches. It is usually the case that the spectroscopy incorporated with a broadband detection scheme has a great advantage over single-point detection. Therefore, using a broadband continuum probe seems like a better way to investigate vibrationally driven reactions; however, we need to also consider the signal level and the noise associated with the measurement. The noise we observe when we use a broadband continuum probe pulse (1~2 mOD) is notably higher than when we use a single wavelength probe pulse (~100 μOD). We first attempted these experiments using a broadband probe, but it turned out that the population of reacting Br atoms was not sufficient to observe the reactive signal over the noise. Since the IR-driven signals that we are looking for are small, we need to use single-point detection. Another consideration is the IR photon density. Since we excite a solvent vibrational mode to promote the reaction, there are many molecules available for the IR excitation. Ideally, we would generate enough IR power to saturate the desired IR transition, but in practice saturating the fundamental transition is challenging. In the experiments discussed, we excite the first overtone of the C-H stretch of the solvent molecules. While the absorption cross section of the overtone is smaller than that of the fundamental, the OPA generates more near-IR light (needed for overtone excitation) than mid-IR light (needed for fundamental excitation), and

thus, we see better difference signals when we pump the overtone excitation. Based on these experiences, we employ photolysis and near-IR pump pulses to initiate the reaction and a 400 nm single wavelength probe pulse to monitor the reaction progress. We use 400 nm light as our probe because it is conveniently made *via* second harmonic generation of the laser output and it overlaps nicely with transient absorption features of interest for all of the solutions we investigate in this study.

Figure 5 shows a typical three beam scans of a solution of Br_2 in CH_3OH after excitation with 400 and 1700 nm light for the generation of Br and the O-H stretch overtone excitation of CH_3OH, respectively. From one scan we record four traces: the time evolutions of probe induced by (1) the photolysis pulse only, (2) the near-IR pump pulse only, (3) both the photolysis and the near-IR pump pulses and, finally, (4) the difference signal calculated by subtracting (1) and (2) from (3). This fourth trace, the difference signal, contains the desired information about the time evolution of the probe pulse that occurs only when both the photolysis and near-IR pump pulses interact with the sample. If the photolysis and near-IR pump beams do not mutually affect the sample, we would expect the difference signal just to be noise, (3) would just be the simple sum of (1) and (2).

In the Br_2 solution in CH_3OH, the 'photolysis-only' signal in Figure 5(a) looks the same as that at 380 nm in the continuum probe experiments displayed in Figure 1(c). This confirms that we probe the Br–solvent complex at 400 nm. For the 'near-IR pump-only' signal, there is nothing except a coherent artifact at a 0 ps time delay, as shown in Figure 5(b). This is as expected, because the near-IR excites the first overtone of the C–H stretch of CH_3OH and the CH_3OH does not show a spectral signature at 400 nm. At first glance, the 'photolysis and near-IR pump' seen in Figure 5(c) signal looks like the 'photolysis-only' signal seen in Figure 5(a).

Figure 5. Three beam scans for a Br_2 solution in CH_3OH: (a) 400 nm photolysis and 400 nm probe pulses, (b) 1700 nm IR pump and 400 nm probe pulses, (c) 400 nm photolysis, 1700 nm IR pump, and 400 nm probe pulses, and (d) the difference signal obtained by subtracting both (a) and (b) from (c). The 'offset' indicates depletion of the $Br–CH_3OH$ complex by IR pump excitation.

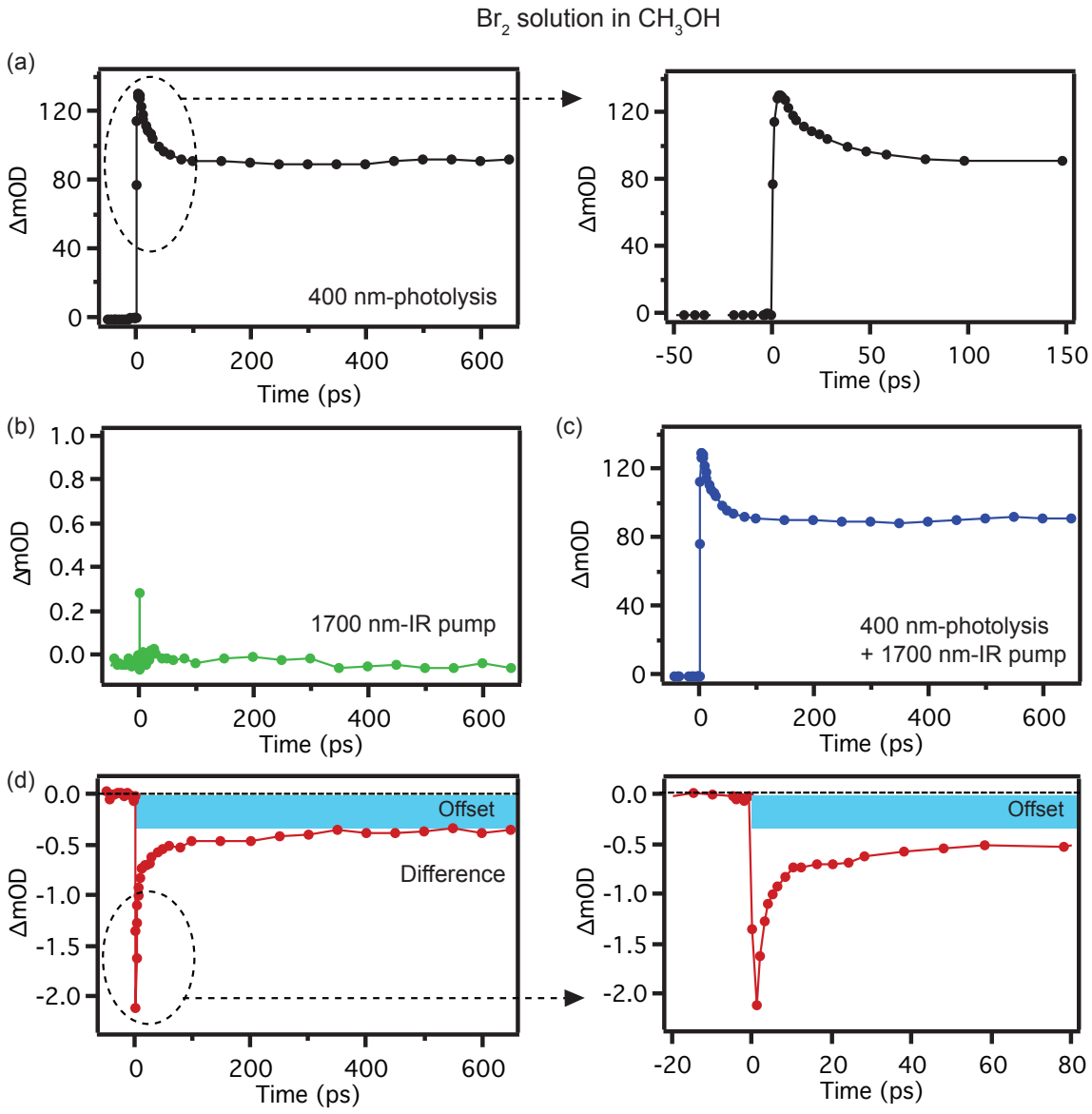
Br2 solution in CH3OH
(a)
ΔmOD
120
80
40
0
400 nm-photolysis
0
200
400
600
Time (ps)
-50
0
50
100
150
(b)
1.0
0.8
0.6
0.4
0.2
0.0
1700 nm-IR pump
(c)
400 nm-photolysis
+ 1700 nm-IR pump
(d)
Offset
Difference
-0.5
-1.0
-1.5
-2.0
-20
20
40
60
80

However, it becomes apparent in the difference signal (Figure 5(d)) that we observe a negative going-signal and a negative offset from the baseline at long delay time. The timing between the photolysis and near-IR pump beams is a controllable parameter, and in this case of the Br_2 solution in CH_3OH the signal is optimized when the near-IR pump beam arrives after the photolysis within a few picosecond interval. If the time delay is more than a few picoseconds, the difference signal disappears entirely. The relaxation of the C–H overtone excitation is probably very quick, likely dissipating into other specific modes or into the bath within a few picoseconds. To efficiently promote the reaction, we expect that the Br atoms have to encounter vibrationally excited CH_3OH molecules before the energy in the C–H overtone is lost. If the near-IR pump beam arrives sufficiently after the photolysis beam, the amount of Br atoms available for reaction will reduce due to geminate recombination.

The difference signal in the Br_2 solution in methanol shows a negative going dip at 0 ps, which recovers to a steady level that is below the initial baseline. The recovery of this signal is best fit by a double exponential fit, returning time constant of 2.2 and 62 ps. Unfortunately, these recovery times are not terribly consistent from scan to scan and their physical meaning is currently unclear. We know the difference signal is maximized when the photolysis precedes the IR pump, and we tentatively ascribe to the idea that the large depletion may reflect vibrational predissociation of the Br–methanol complexes and that the subsequent recovery indicates that following this predissociation there is some re-formation of the complex. We prefer to focus on the offset that persists even at the longest time delay in the difference signal. The magnitude of this offset also fluctuates from 500 μOD to 1 mOD across the scans, but we observe this offset consistently in every scan. If we continue with the idea of vibrational predissociation, this

negative offset could mean that some of the Br atoms find each other in solution to re-form Br_2. More interestingly, it could indicate reaction of the Br atoms with vibrationally excited CH_3OH molecules (created from the initial vibrational excitation or as a product of the vibrational predissociation) that contain enough energy to overcome the barrier to reaction. In other words, the offset observed in the Br–CH_3OH complex reflects the fraction of Br atoms that are no longer complexed to CH_3OH, either because of geminate recombination or because they have undergone a hydrogen abstraction reaction.

We also observe a negative offset in the difference signal of a $CHBr_3$ in DMSO solution (Figure 6). In this case, the near-IR pump beam is tuned to 1680 nm, which is one of two C–H overtones observed in DMSO. The timing between the photolysis and near-IR pump beams is the same as in the Br_2 solution in CH_3OH. Again, the 'photolysis-only' signal exhibits the same dynamics as in the continuum probe experiments displayed in Figure 4, confirming that at 400 nm we are detecting the same species, the Br–DMSO complex. The 'near-IR pump-only' signal shows nothing except a coherent artifact at 0 ps, just like in the Br_2 solution in CH_3OH. The difference signal of the $CHBr_3$ solution in DMSO is qualitatively similar to the Br_2 solution in CH_3OH, showing a negative dip, a recovery, and a long time negative offset. The magnitude of the negative offset varies from 1 to 2 mOD over every measurement of the $CHBr_3$ solution in DMSO.

In both the $CHBr_3$ solutions in DMB and CH_2Cl_2, we can detect both the $CHBr_3$-Br complex and the *iso*-$CHBr_2$-Br isomer using 400 nm light, but it is hard to distinguish between the two species due to the large overlap of their absorption bands at this wavelength. In the $CHBr_3$ solution in CH_2Cl_2 solution, we may possibly probe more $CHBr_3$-Br than the isomer because 400 nm is really at the edge of the isomer's absorption band in this solvent. The

Figure 6. Three beam scans for a $CHBr_3$ solution in DMSO: (a) 400 nm photolysis and 400 nm probe pulses, (b) 1680 nm IR pump and 400 nm probe pulses, (c) 400 nm photolysis, 1680 nm IR pump, and 400 nm probe pulses, and (d) the difference signal obtained by subtracting both (a) and (b) from (c). The 'offset' indicates depletion of the Br–DMSO complex by IR pump excitation.

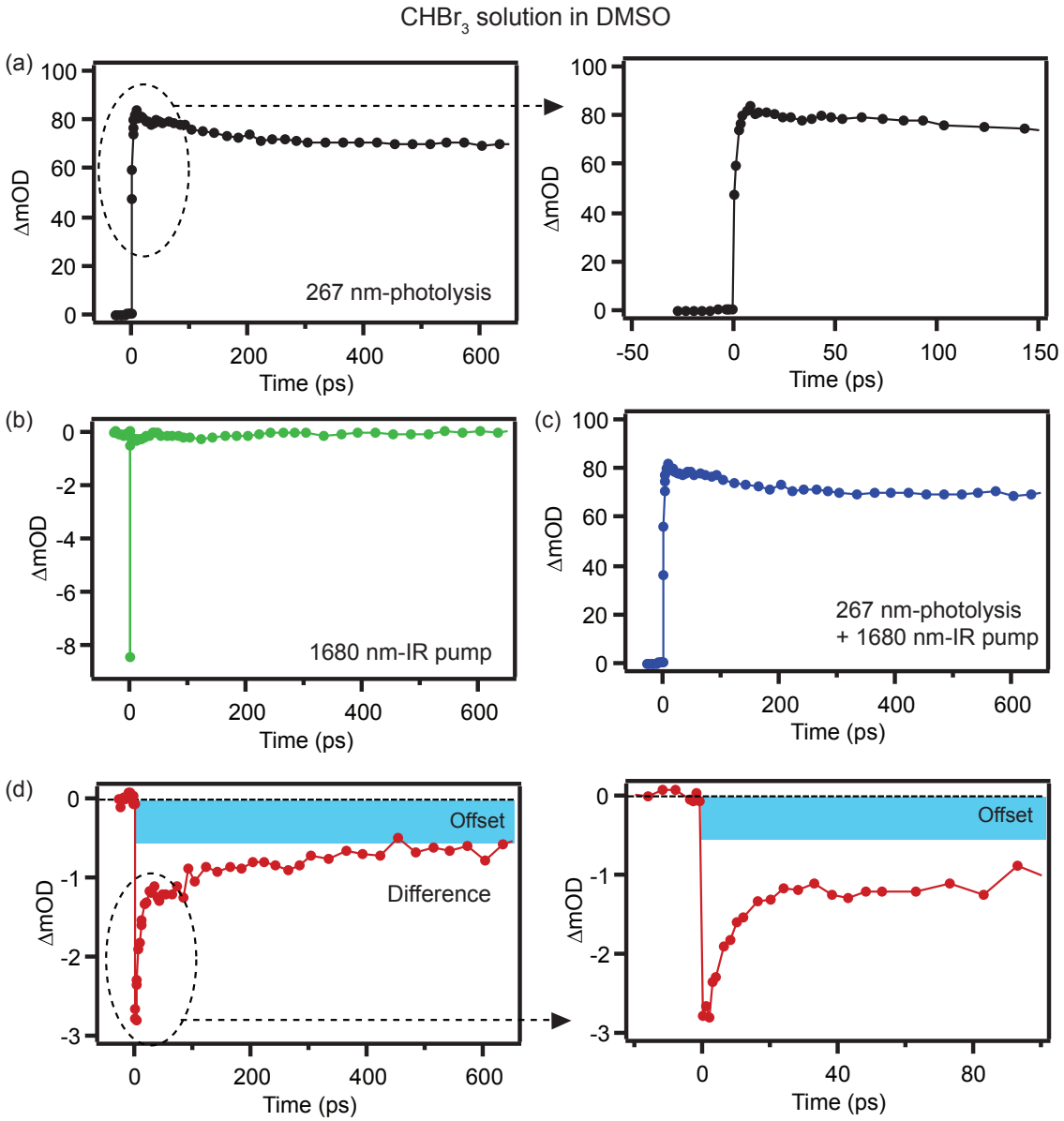
CHBr3 solution in DMSO
(a)
ΔmOD
Time (ps)
267 nm-photolysis
(b)
1680 nm-IR pump
(c)
267 nm-photolysis
+ 1680 nm-IR pump
(d)
Offset
Difference

difference signal of the $CHBr_3$ solution in CH_2Cl_2 solution (Figure 7) shows the familiar pattern discussed above. Meanwhile, the $CHBr_3$ solution in DMB (Figure 8) exhibits a large negative offset, but without the sharp negative dip at 0 ps, which is accompanied by a fast recovery.

4.3.3. Near-IR pump wavelength dependence of difference signal

In order to confirm that the difference signals that we observe in our three beam experiments originate from vibrationally driven reactions, we carry out near-IR pump wavelength dependent experiments. These experiments give direct evidence for the role of vibrational excitation by testing the prerequisite need of IR resonant energies to obtain the long time offset in the difference signals.

Figure 9(a) shows an absorption spectrum of CH_3OH in the near-IR region. The first overtone of the C–H stretch appears at 1700 nm, and the broad absorption band at 1573 nm is presumed to be the first overtone of the O–H stretch. Figure 9(b) shows that the magnitude of the difference signal drastically changes with the IR wavelength, depending particularly on whether the near-IR pump beam is on or off resonance with a CH_3OH absorption. When we tune the IR wavelength to 1500 and 1700 nm, resonant with the overtone absorption bands, we observe large difference signals accompanied by a large negative offset. On the other hand, if the near IR-pump is off-resonant, the difference signal becomes much smaller and, importantly, the negative offset decreases considerably, as can be seen with the IR wavelength at 1300 and 1900 nm. Thus, Figure 9 demonstrates the direct relationship between the vibrational excitation of CH_3OH and the appearance of difference signal (in particular the magnitude of the long time offset) in our three beam experiments. Since excitation of either the C–H or O–H stretching overtones of CH_3OH result in large difference signals, it may be that the Br atom can react with hydrogen

Figure 7. Three beam scans for a $CHBr_3$ solution in CH_2Cl_2: (a) 400 nm photolysis and 400 nm probe pulses, (b) 1700 nm IR pump and 400 nm probe pulses, (c) 400 nm photolysis, 1700 nm IR pump, and 400 nm probe pulses, and (d) the difference signal obtained by subtracting both (a) and (b) from (c). The 'offset' indicates depletion of the $CHBr_3$-Br complex by IR pump excitation.

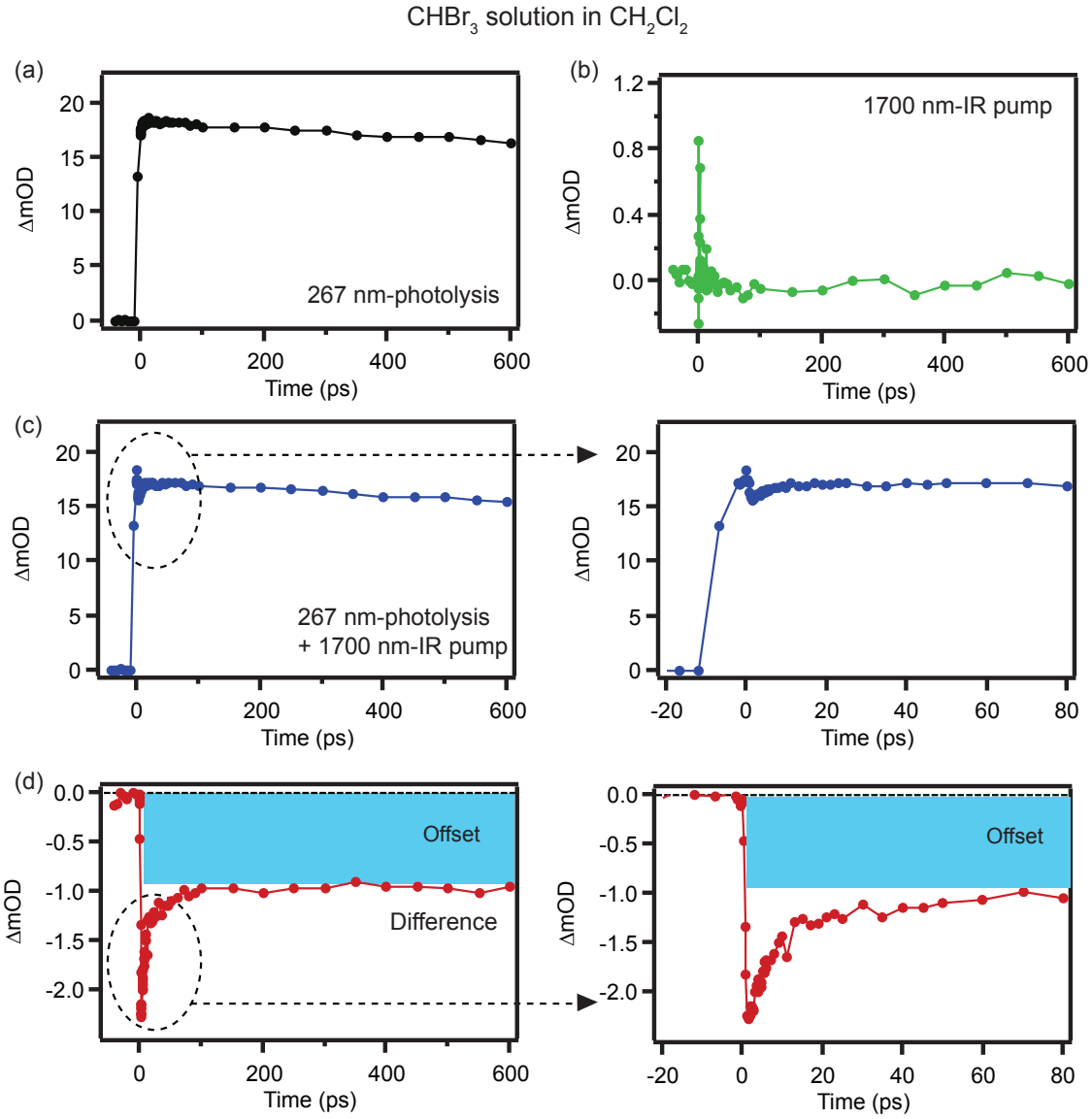
CHBr3 solution in CH2Cl2
(a)
ΔmOD
267 nm-photolysis
Time (ps)
(b)
1700 nm-IR pump
ΔmOD
Time (ps)
(c)
ΔmOD
267 nm-photolysis
+ 1700 nm-IR pump
Time (ps)
ΔmOD
Time (ps)
(d)
ΔmOD
Offset
Difference
Time (ps)
ΔmOD
Offset
Time (ps)

Figure 8. Three beam scans for a $CHBr_3$ solution in DMB: (a) 400 nm photolysis and 400 nm probe pulses, (b) 1692 nm IR pump and 400 nm probe pulses, (c) 400 nm photolysis, 1692 nm IR pump, and 400 nm probe pulses, and (d) the difference signal obtained by subtracting both (a) and (b) from (c). The 'offset' indicates depletion of the $CHBr_3$-Br complex by IR pump excitation.

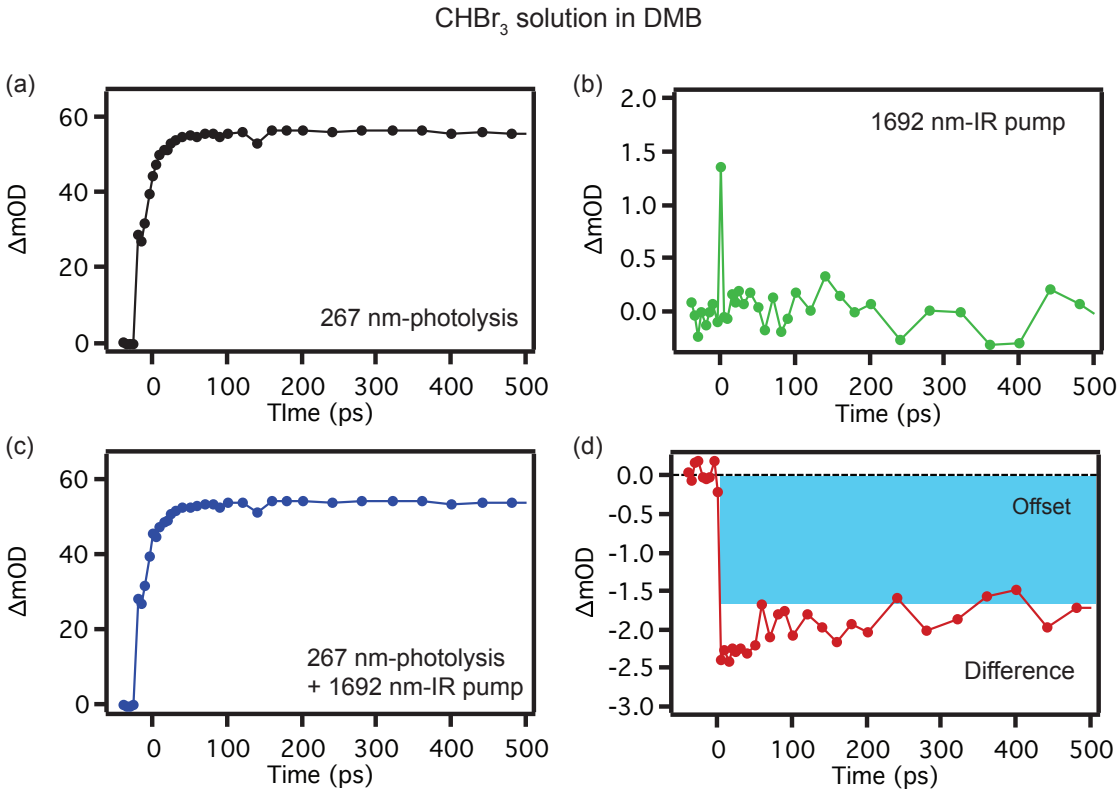
CHBr3 solution in DMB
(a)
ΔmOD
267 nm-photolysis
TIme (ps)
(b)
1692 nm-IR pump
ΔmOD
Time (ps)
(c)
ΔmOD
267 nm-photolysis
+ 1692 nm-IR pump
Time (ps)
(d)
ΔmOD
Offset
Difference
Time (ps)

Figure 9. (a) The absorption spectrum of CH_3OH and (b) the difference signals obtained for a Br_2 solution in CH_3OH at various near-IR pump wavelengths. The arrows in (a) indicate the wavelengths of the near-IR pump used in the three beam scans.

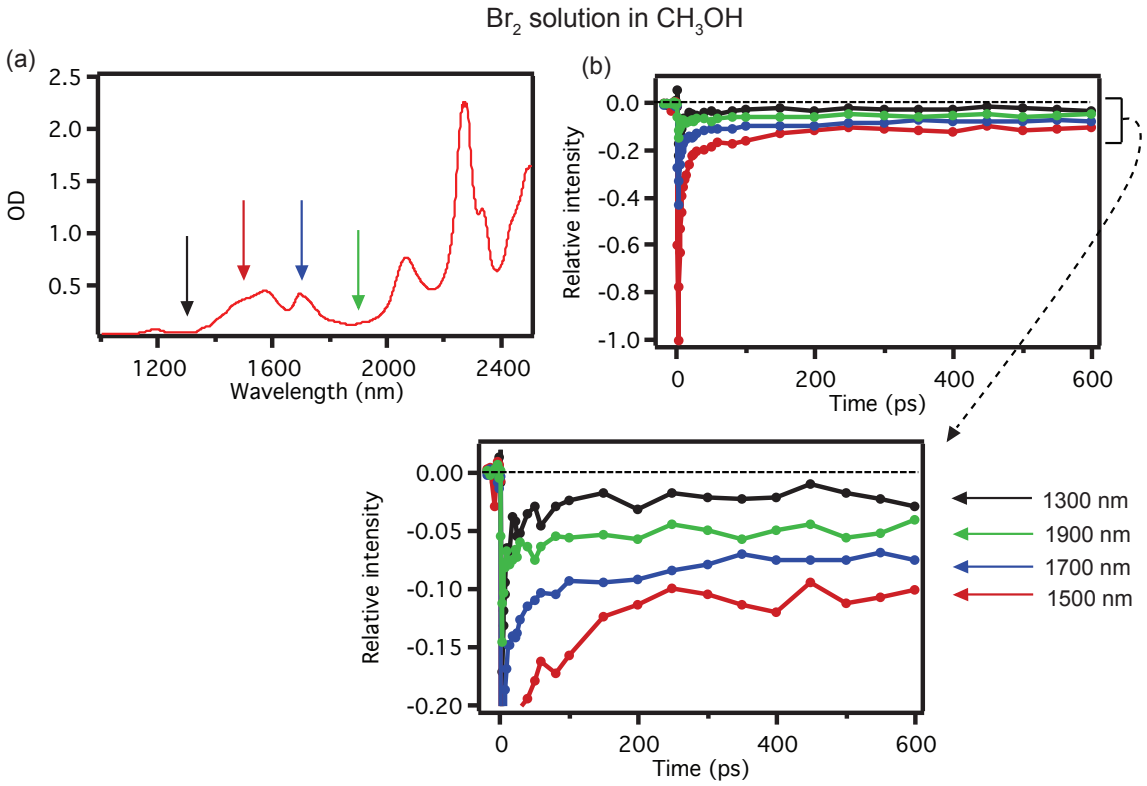
Br2 solution in CH3OH
(a)
OD
Wavelength (nm)
(b)
Relative intensity
Time (ps)
Relative intensity
Time (ps)
1300 nm
1900 nm
1700 nm
1500 nm

atoms from either the methyl or hydroxyl groups. While these results clearly illustrate the importance of the near-IR pump beam being resonant with a vibration of the solvent, direct evidence of HBr production is still required to address whether the solvent vibrations are causing a bimolecular (hydrogen abstraction) or unimolecular (vibrational predissociation) reaction.

We observe similar behavior for the near-IR wavelength dependence of the difference signal in the $CHBr_3$ solution in DMSO. Figure 10(a) shows the near-IR absorption spectrum of DMSO. There are two absorption peaks, one appearing at 1680 nm and the other at 1725 nm. The band at 1680 nm is the first overtone transition of the C–H stretch, but the origin of the band at 1725 nm is unknown.[18] Like in the Br_2 solution in CH_3OH, we observe large difference signals when the near-IR pump is resonant with an absorption band of DMSO (Figure 10(b)). Futher, the difference signal decreases if we detune the near-IR pump to 1850 nm and the negative offset disappears.

For solutions of $CHBr_3$ in DMB, we find that the solution changes on a relatively short time scale. It is noticeable over the duration of the experiments, to the extent that the magnitude of the difference signal decreases as we repeat the three beam scans. This prevents us from obtaining consistent results in the near-IR pump wavelength dependent experiments for this solution. With the $CHBr_3$ in CH_2Cl_2 solutions, the difference signal does not appear to depend on the near-IR pump wavelength. The magnitude of the negative offset in the difference signal is consistently ~1 mOD regardless of the resonance or nonresonance of the near-IR pump energy with an absorption band of CH_2Cl_2. The difference signal that we observe in the $CHBr_3$–CH_2Cl_2 solution is suspicious; it seems that this loss of the $CHBr_3$–Br complex is not due, at least solely, to the vibrational excitation of the solvent.

Figure 10. (a) The absorption spectrum of DMSO and (b) the difference signals obtained for a $CHBr_3$ solution in DMSO at various near-IR pump wavelengths. The arrows in (a) indicate the wavelengths of the near-IR pump used in the three beam scans.

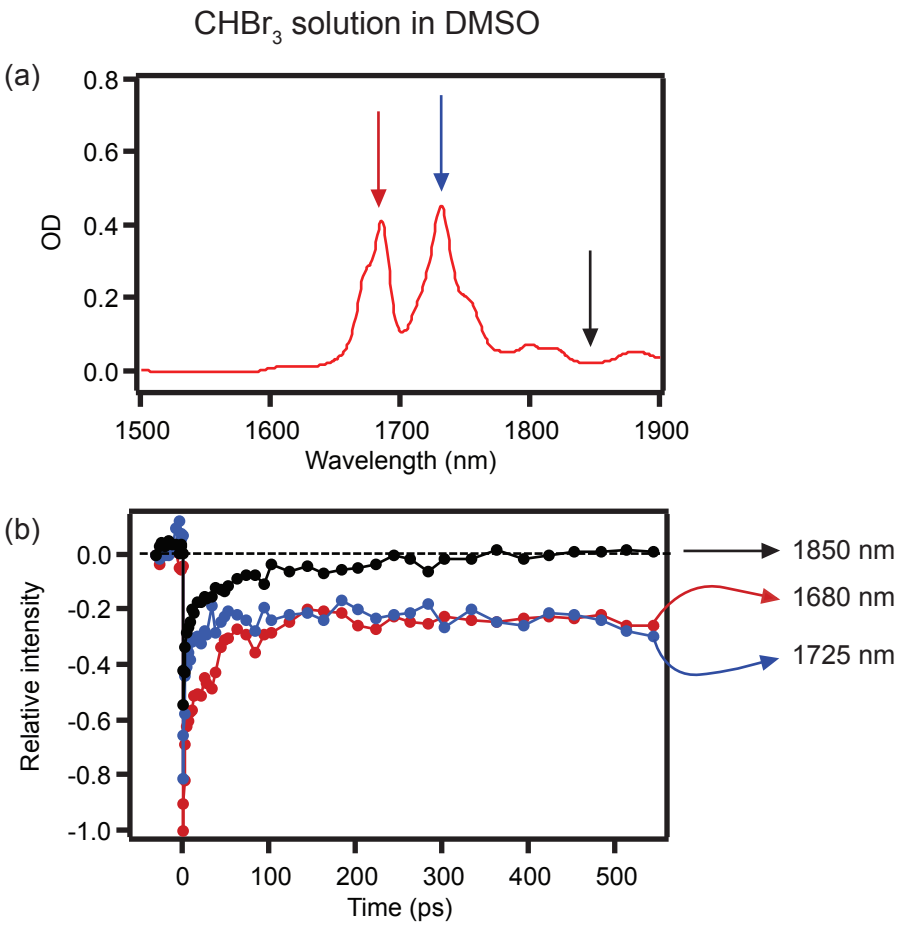
CHBr3 solution in DMSO
(a)
OD
0.8
0.6
0.4
0.2
0.0
1500
1600
1700
1800
1900
Wavelength (nm)
(b)
Relative intensity
0.0
-0.2
-0.4
-0.6
-0.8
-1.0
0
100
200
300
400
500
Time (ps)
1850 nm
1680 nm
1725 nm

The results of the Br_2 in CH_3OH and $CHBr_3$ in DMSO solutions demonstrate a strong IR wavelength dependence on the long time offset observed in the difference signal. We believe that this difference signal is reporting on the loss of some of the reactive Br. For these systems, the Br atoms are complexed with the solvent. The vibrational excitation of the solvent (and perhaps the Br–solvent complex) results in a long time offset in the difference signal. This offset is attributable to either geminate recombination following vibrational predissociation or the abstraction of a hydrogen atom by a Br atom. The 'bimolecular' reaction could occur as in intramolecular hydrogen transfer reaction of the complex or as a true bimolecular reaction following predissociation. Given the large excess of the solvent (versus the solute), it is conceivable to consider the magnitude of the offset too great to be accounted for merely from geminate recombination. But then, when one considers the lack of clear evidence for IR wavelength dependence in those systems for which we probe $CHBr_3$–Br ($CHBr_3$ in CH_2Cl_2 and DMB), it seems that it may be the vibrational excitation of the Br–solvent complex that is actually important. Due to the ambiguity in the measurement that detect the loss of reactive Br, we need a more direct probe of the bimolecular reaction.

4.3.4 The efforts toward detecting HBr products

Detecting the reaction product, HBr, will provide be direct evidence of a bimolecular reaction. Moreover, observing the formation of the product in real time can provide invaluable information about the reaction dynamics in detail, which should help account for contributions from vibrational predissociation. Recent studies of bimolecular reactions in the condensed phase reveal detailed reaction dynamics, such as energy disposal into products and relaxation of

vibrationally excited product, by monitoring the formation of products *via* time-resolved IR spectroscopy.[19-23]

For these reasons, we put much effort into finding the signal of the HBr product from vibrationally driven reactions in our transient IR absorption measurements. As with the transitent absorption data, there are limitations to consider, some of which are really hard to overcome. First, the IR absorption spectrum of the solvent (which we also use as a reaction partners for the Br atoms) should be spectrally clear near 4 μm; this is the region in which the HBr absorption is expected to appear. Again, if it is not clear, the solvent will act as an optically thick sample and absorb a large portion of our IR probe light, which will greatly increase the challenge of detecting the HBr signal. Even if there is a small absorption, the interference from the solvent absorption change will complicate the transient absorption signal. All the solvents that we have discussed so far have a clear absorption spectrum at this wavelength, except for CH_3OH. Secondly, we need to consider the stability of HBr in the solvent. Also, the position of the HBr absorption peak in the IR absorption spectrum is not known in most organic solvents. Thus, we bubble HBr gas into each of the solvents in an attempt to get a high enough concentration of HBr to observe the actual location of the transition in a static IR absorption spectrum. However, we only find the HBr absorption peak in CH_2Cl_2. This is unfortunate, as we were unable to get reliable IR wavelength dependent data while probing the Br loss for the $CHBr_3$ solution in CH_2Cl_2. With the DMSO and DMB solvents, there is no signs of HBr in the IR absorption spectrum (even after background subtraction of the IR absorption spectrum of the intact solvent). Further, we observe a color change and the formation of a precipitate using the DMB solvent. (This may be consistent with the fact that the $CHBr_3$ solution in DMB changes as we repeat the

three beam scans.) In CH_3OH, a very tiny absorption peak appears near 4 μm, but the interference from the CH_3OH absorption is rather severe.

Our last concern is that the HBr signal will be too small to be detectable in the transient IR absorption measurements. Based on the extinction coefficient of the Br–DMSO complex at the absorption maximum (430 nm) and the IR absorption cross section of HBr in the gas phase,[17] we estimate the magnitude of the expected HBr signal in the transient IR absorption measurement. If we assume that a 1 mOD offset in the difference signal is due in its entirety from the loss of the Br–DMSO complex through a hydrogen abstraction reaction (in short, 1 Br–DMSO = 1 HBr), then we calculate the magnitude of the HBr signal to be 17 μOD. This value is as large as the noise level in our transient IR absorption measurements, and we have worked rather hard to get the current noise level as low as they are. Perhaps not surprisingly, we have been unsuccessful at finding any HBr signal in any of transient IR absorption measurements. However, there are still open possibilities that we can find a product and clear an ambiguity; steady-state IR absorption or NMR studies after the long irradiation of photolysis and near-IR lights can be one of them.

4.4 Summary

We demonstrate that excitation of the first overtone of the C–H stretch (and the O–H stretch in the case of a CH_3OH solution) of various solvents can alter the dynamics of a Br–solvent complex in CH_3OH and DMSO. We observe difference signals in a three beam experiment (near-IR pump, photolysis, and probe) having a long time offset of 0.5 to 2 mOD. More importantly, these difference signals show a near-IR pump wavelength dependence. Only when the near-IR pump beam is resonant with an overtone absorptions of solvents will the

difference signal become large and exhibit a significant negative offset at long delay times. The negative offset, which represents of loss of the Br–solvent complex, may come from a hydrogen abstraction reaction between the Br atoms and the vibrationally excited solvent molecules. However, we cannot rule out the possibility of vibrational predissociation followed by geminate recombination. To our knowledge, this is the first experiment that shows the possibility of vibrationally driven bimolecular reactions in the condensed phase.

References

(1) Crim, F. F. *Acc. Chem. Res.* **1999**, *32*, 877.

(2) Sinha, A.; Hsiao, M. C.; Crim, F. F. *J. Chem. Phys.* **1991**, *94*, 4928.

(3) Sinha, A.; Thoemke, J. D.; Crim, F. F. *J. Chem. Phys.* **1992**, *96*, 372.

(4) Bronikowski, M. J.; Simpson, W. R.; Zare, R. N. *J. Phys. Chem.* **1993**, *97*, 2194.

(5) Yoon, S.; Henton, S.; Zivkovic, A. N.; Crim, F. F. *J. Chem. Phys.* **2002**, *116*, 10744.

(6) Yoon, S.; Holiday, R. J.; Crim, F. F. *J. Chem. Phys.* **2003**, *119*, 4755.

(7) Yoon, S.; Holiday, R. J.; Crim, F. F. *J. Phys. Chem. B* **2005**, *109*, 8388.

(8) Bechtel, H. A.; Camden, J. P.; Brown, D. J. A.; Martin, M. R.; Zare, R. N.; Vodopyanov, K. *Angew. Chem. Int. Ed.* **2005**, *44*, 2382.

(9) Martin, M. R.; Ankeny Brown, D. J.; Chiou, A. S.; Zare, R. N. *J. Chem. Phys.* **2007**, *126*, 044315.

(10) Sinha, A.; Hsiao, M. C.; Crim, F. F. *J. Chem. Phys.* **1990**, *92*, 6333.

(11) Metz, R. B.; Thoemke, J. D.; Pfeiffer, J. M.; Crim, F. F. *J. Chem. Phys.* **1993**, *99*, 1744.

(12) Bronikowski, M. J.; Simpson, W. R.; Girard, B.; Zare, R. N. *J. Chem. Phys.* **1991**, *95*, 8647.

(13) Prokhorenko, V. I.; Nagy, A. M.; Waschuk, S. A.; Brown, L. S.; Birge, R. R.; Miller, R. J. D. *Science* **2006**, *313*, 1257.

(14) Briney, K. A.; Herman, L.; Boucher, D. S.; Dunkelberger, A. D.; Crim, F. F. *J. Phys. Chem. A* **2010**, *114*, 9788.

(15) *CRC Handbook of Chemistry and Physics*; 87th ed.; CRC Press: Boca Raton, FL, 2012-2013.

(16) Preston, T. J.; Shaloski, M. A.; Crim, F. F. *J. Phys. Chem. A* **2013**, *117*, 2899.

(17) Sumiyoshi, T.; Fujiyoshi, R.; Katagiri, M.; Sawamura, S. *Radiat. Phys. Chem.* **2007**, *76*, 779.

(18) Jayaraj, A. F.; Singh, S. *Proc. Indian Acad. Sci. Chem. Sci.* **1993**, *105*, 71.

(19) Greaves, S. J.; Rose, R. A.; Oliver, T. A. A.; Glowacki, D. R.; Ashfold, M. N. R.; Harvey, J. N.; Clark, I. P.; Greetham, G. M.; Parker, A. W.; Towrie, M.; Orr-Ewing, A. J. *Science* **2011**, *331*, 1423.

(20) Abou-Chahine, F.; Greaves, S. J.; Dunning, G. T.; Orr-Ewing, A. J.; Greetham, G. M.; Clark, I. P.; Towrie, M. *Chem. Sci.* **2013**, *4*, 226.

(21) Dunning, G. T.; Glowacki, D. R.; Preston, T. J.; Greaves, S. J.; Greetham, G. M.; Clark, I. P.; Towrie, M.; Harvey, J. N.; Orr-Ewing, A. J. *Science* **2015**, *347*, 530.

(22) Orr-Ewing, A. J. *J. Chem. Phys* **2014**, *140*, 090901.

(23) Orr-Ewing, A. J. *Annu. Rev. Phys. Chem.* **2015**, *66*, 119.